

September 10th, 2018

MASTER THESIS

Investigation of the Scope and Limitations of Gradient Enhanced Crystal Plasticity in Explaining Macroscopic Phenomena

B. Nijhuis

**Faculty of Engineering Technology (ET)
Chair of Nonlinear Solid Mechanics**

Exam committee:

Prof. dr. ir. A.H. van den Boogaard

Dr. ir. E.S. Perdahcioğlu

Dr. ir. T.C. Bor

Ir. E.E. Aşık

Document number:

Department of Mechanics of Solids, Surfaces and Systems — 76558

UNIVERSITY OF TWENTE.

Abstract

In a wide range of applications, it is important to be able to model the constitutive response of materials. Most models however fail to predict macroscopically observed phenomena in plastic deformation: the Hall-Petch effect, Bauschinger effect and anelastic behaviour. A gradient enhanced crystal plasticity model, in which slip gradients are incorporated in the hardening model through geometrically necessary dislocations (GNDs), is believed to include the physical basis to represent these phenomena. A comprehensive review about its general applicability in this content is however not available. The aim of this work is therefore to assess the scope and limitations of a gradient enhanced crystal plasticity model in predicting macroscopic phenomena observed in plastic deformation of metals.

To establish a consistent simulation framework, a literature study is performed to determine the prerequisites of calculating GND-densities in finite-strain problems. Calculations based on either referential or spatial slip gradients are found suitable for this purpose. This outcome is validated using dedicated simulations, showing that the original gradient calculation algorithm can be retained. This code is extended for use with periodic boundary conditions.

Macroscopic phenomena are investigated by simulating the response of two-dimensional representative volume elements consisting out of hexagonally shaped grains under various loadings. The Hall-Petch effect in work hardening is very well represented by the length scale that is introduced by the slip gradients. Including GNDs clearly extends the width of the stress distribution within the material. The presence of such a stress distribution results in small scale plasticity effects when the material is unloaded after deformation. The Bauschinger effect is hereby enhanced. Small amounts of anelasticity are also observed as a result, but not as pronounced as experimentally observed.

The validity of the gradient enhanced crystal plasticity model is tested by a quantitative comparison of the evolution of GND-densities with experimental results. Using electron backscatter diffraction, local misorientations between material points can be characterised and related to the GND-density. The nature of both the density distribution as well as the evolution of the total GND-number with strain agree between experiments and simulations. The experimentally observed initial dislocation densities are not present within the numerical model though. Possibilities for including a realistic initial dislocation distribution should therefore be investigated.

As extension to the theoretical framework of the model, an alternative version for the included stress-update algorithm is proposed. The commonly applied check for elastic deformations is removed by modifying the flow criteria. It is shown it can be applied to problems involving small lattice rotations successfully but requires further research in maintaining a stable set of active slip systems in large-rotation problems.

A gradient-enhanced crystal plasticity model was found to be well capable of predicting macroscopic phenomena related to size effects and plasticity effects resulting from plastic anisotropy of a material's constituent grains. It is not yet fully applicable to effects that may originate from microstructural effects that do not involve dislocation-generation. To further validate the conclusions from this work, it is recommended to perform tests on three-dimensional models with realistic grain shapes to include the effects of the microstructure itself.

Preface

This thesis describes the findings of the research I undertook in partial fulfilment of the requirements for the degree of Master of Science in Mechanical Engineering at the University of Twente. It is performed on the subject of crystal plasticity models, which are increasingly used in modelling the constitutive behaviour of metals. The research started from my interest in modelling metal plasticity developed during my internship. During my graduation period from January to September 2018, I have been able to gain many new insights into the subject of crystal plasticity and a better understanding of the plastic behaviour of metals in general. With this new understanding and the final result of this research I am very satisfied.

My work was supervised by dr. ir. E.S. Perdahcioğlu, whom I would like to thank for formulating this challenging but rewarding assignment, his guidance and support throughout the research and providing me with the feedback that lead to this thesis. I would also like to express my gratitude to ir. E.E. Aşık for supporting me with the simulations on many occasions and agreeing to take place in my graduation committee. His contribution to this thesis by performing the EBSD-measurements is greatly appreciated. I wish to thank the remaining members of my graduation committee, prof. dr. ir. A.H van den Boogaard and dr. ir. T.C. Bor for offering their time and effort in the final phase of my studies.

I would like to thank my friends and roommates for the pleasant time, fruitful discussions and support they offered during my graduation. A special word of thanks goes out to my family and girlfriend for their everlasting support, guidance and motivation that greatly helped me in completing this thesis.

Last but not least, I would like to thank you as reader for showing your interest in my work.

Haaksbergen, September 2018,

Björn Nijhuis

Contents

1	Introduction	1
2	Constitutive framework of crystal plasticity	4
2.1	Kinematical model of crystal deformation	4
2.2	Stress response	5
2.3	Material behaviour in the plastic regime	5
2.3.1	Hardening behaviour	6
2.4	Algorithmic implementation	8
2.4.1	Discretizing constitutive equations	8
2.4.2	Stress update algorithm with elastic check and active set determination	9
2.4.3	Gradient and GND-density calculations	12
2.4.4	Finite Element implementation	12
3	Extensions to the crystal plasticity model	14
3.1	Stress update algorithm without elastic check and active set determination	14
3.1.1	Implementation of modified flow criteria in stress update algorithm	15
3.1.2	Comparison of the algorithms	16
3.2	Gradient calculations in periodic models	18
3.2.1	Comparison of the gradient codes	21
3.3	Determining GND-densities in a finite-strain formulation	22
3.4	Conclusions and recommendations	24
4	Verification of the crystal plasticity model	25
4.1	Verification of the lattice rotation update	25
4.2	Verification of the finite strain implementation	26
4.2.1	Conclusion	28
5	Predicting macroscopic phenomena using a gradient-enhanced crystal plasticity model	29
5.1	Modelling aspects	29
5.1.1	RVE with hexagonal grains	30
5.2	The Hall-Petch effect	31
5.2.1	The Hall-Petch effect in crystal plasticity models	31
5.2.2	Setting up the FEM-models	32
5.2.3	Results	34
5.2.4	Discussion of results	37
5.2.5	Conclusions	39
5.3	The Bauschinger effect	40
5.3.1	Setting up the FEM-models	41
5.3.2	Results	42
5.3.3	Discussion of results	45
5.3.4	Conclusions and recommendations	48
5.4	The anelasticity effect	48
5.4.1	Setting up the FEM-models	50
5.4.2	Results and discussion	50
5.4.3	Conclusions and recommendations	53
6	Experimental validation of the GND-evolution	54
6.1	Methods	54
6.2	Results	56
6.3	Discussion of results	59
6.4	Conclusions and recommendations	59
7	Conclusions	60
	Bibliography	61

Appendices	65
A Derivation of kinematical model assuming small elastic stretch	66
B Continuously differentiable approximation of the max() function	68
C Stress-update algorithm flowcharts	71
D Driver input files for future work	72
E Generating RVEs with random disorientation distributions	73
E.1 Generating random crystallographic orientations	73
E.2 Calculating disorientation distributions	74
E.3 RVEs with random disorientation distributions	75
F Numerical integration of dislocation densities	78

1 | Introduction

Modelling the constitutive response of materials is important in various stages in the lifetime of products. Whether it concerns the production and processing stage of raw materials, the transformation of raw materials into a final product or its usage phase, insight into the material's response to applied loads and deformation aids in the design process, quantifying product characteristics and assessing possible modes of failure throughout each of these phases [1]. Implementation of constitutive models into simulation software makes it possible to account for material induced limitations on product performance in early stages of the design process, limiting rework costs and time.

To describe the evolution of (plastic) deformation within metals, two main aspects need to be taken into consideration. The onset of plastic flow is described by the material's yield stress. After yielding and with increasing plastic flow, an increase in stress is observed: the material work-hardens. Thus, the apparent flow stress changes with ongoing deformation. The evolution of flow stress therefore needs to be taken into account by a suitable hardening model.

Different possibilities for implementing such behaviour in numerical models exist. The most elementary, but least general, method is a direct experimental characterisation of the response for the material and loading conditions that will be simulated. Generality, modifiability and implementability of this approach can be improved by using mathematical representations of stress-strain curves based upon a limited set of material parameters. However, the loading conditions that can be represented with conventional testing methods are limited. A wide variety of multi-axial yield criteria has therefore been developed to be able to extrapolate results from testing conditions to general stress states [2].

Even though plastic behaviour under arbitrary stress states can be captured using a suitable yield-criterion and hardening function, some macroscopic phenomena commonly observed in plastic deformation of metals are difficult to implement in continuum models [3]. These include the Bauschinger and anelasticity effects in processes where the loading direction is changed and grain-size dependency of material properties, the Hall-Petch effect. Numerous attempts have been made to account for this shortcoming by extending phenomenological continuum models. The main disadvantage of these models is the increasing number of fitting constants and empirical extensions underlying them [4].

The physical origin of the abovementioned macroscopic effects is often related to microstructural inhomogeneities inherent to polycrystalline materials. Within a polycrystalline aggregate, each grain has a distinct lattice direction and is mechanically anisotropic [5]. Together with the requirement of continuity of the deformation of adjacent grains along their common boundaries, this causes inhomogeneous deformation within grains. With decreasing grain size, the level of inhomogeneity at the grain boundaries increases [6] and it was hypothesized already in 1950 that this mechanism is responsible for a size-dependent macroscopic response [7]. Another effect that arises from lattice misorientations is the formation of residual stresses within the microstructure, which can be correlated to the macroscopically observed Bauschinger effect [8]. Anelasticity effects are another reflection of small scale plasticity effects during unloading [9].

From the aforementioned observations, it becomes apparent that microstructural effects need to be taken into account to fully capture the constitutive response of metals. At the microscale, plastic deformation can be modelled most suitably using crystal plasticity models [10]. Herein, plastic deformation is assumed to be caused solely by dislocation slip on the material's individual slip systems. Since the method was first introduced in 1982 by Pierce et. al. [11], a growing interest in crystal plasticity finite element modelling has developed and it was used in a wide range of applications [5]. The macroscopic response of a polycrystalline material can be simulated using a crystal plasticity framework by means of a representative volume element (RVE). In such two- or three-dimensional models, a number of differently oriented grains is present. Macroscopic quantities are obtained from the RVE's microscopic response under appropriate boundary conditions through averaging principles [12].

Results from crystal plasticity simulations performed using RVEs have shown that size-dependent material properties (e.g. [13–15]), the Bauschinger (e.g. [16, 17]) and anelasticity effects (e.g. [18]) can be captured. In these results however, the formulations for the description of crystallographic slip are often modified or extended explicitly to add the intended macroscopic behaviour to the model. This leads to the same disadvantages pointed out for the extended continuum models above.

It would therefore be desirable to obtain a model that is capable of correctly capturing the macroscopic behaviour without explicit modifications to the underlying constitutive framework. This model should be based upon an experimentally justifiable, physical basis. In this work, such a model is hypothesised to be represented by a gradient enhanced crystal plasticity model. The reasoning behind this choice will now be discussed.

Consider the class of phenomenologically based crystal plasticity models, in which the evolution of slip and slip resistance is governed by the total dislocation densities on the slip systems ([5, 12]). Here, a higher dislocation density implies a higher resistance against deformation. From a macroscopic point of view, it has long been agreed that it is possible to distinguish two types of dislocations [19]. Statistically stored dislocations (SSDs) form during uniform plastic deformation due to random trapping. Geometrically necessary dislocations (GNDs) on the other hand, form during inhomogeneous deformation to maintain compatibility of the lattice. The evolution of the SSD density can thus be expressed as function of slip [12]. As inhomogeneous plastic deformation is only possible if there exist gradients of plastic slip, the GND density can be expressed as function of slip gradients [20]. Through the incorporation of the GND density in the evolution equation of the slip resistance, a gradient-enhanced crystal plasticity model is obtained.

Due to differences in lattice orientations between adjacent grains in polycrystalline materials, GNDs primarily form near grain boundaries ([21, 22]). With decreasing grain size, the level of inhomogeneity at the grain boundaries and thus the number of GNDs increases. Together with the length scale that is introduced by the Burgers vector that relates the slip gradients to GND-densities [6], a gradient-enhanced model crystal plasticity model is rendered size dependent. A better representation of the Hall-Petch effect is thus expected. The non-uniform distribution of GNDs over the grains will additionally cause non-uniform hardening and thus a widening of the stress distribution over the material. The Bauschinger and anelasticity effects resulting from microstructural residual stresses are therefore anticipated to become more pronounced when including GNDs.

Literature results published on applications of gradient enhanced crystal plasticity methods so far, are generally limited to a single macroscopic phenomenon. Both rate-dependent and rate-independent implementations are used and great differences are found in the formulation of slip system hardening. Additionally, the results differ in terms of simulated material and RVE setup. Also, two- and three-dimensional models are used, with realistic as well as conceptual microstructures. Therefore, a good indication of the overall applicability of gradient enhanced crystal plasticity in predicting macroscopic phenomena in plastic deformation is not available, as results are not comparable.

Within this work, it is strived to overcome this shortcoming in the published literature. The full range of macroscopic phenomena mentioned above will be simulated using the same crystal plasticity model and RVEs that are similar in setup. No extensions or modifications to the constitutive formulation of crystal plasticity will be made apart from the inclusion of gradient effects through GNDs and the hardening model. The formulation is thus not adapted to fit one particular phenomenon. This provides insight into the extent to which the Hall-Petch, Bauschinger and anelasticity effects can be predicted by the presence of GNDs and thus inhomogeneous plastic deformation within the microstructure.

If successful in representing the constitutive response of metals, GECP-models provide a versatile tool in material development and characterisation, based on well motivated underlying physical mechanism. The final goal of this research is therefore to assess the general applicability of a gradient enhanced crystal plasticity model in capturing macroscopic phenomena observed in plastic deformation of metals.

The remainder of this report is structured in three parts. The first part concerns the theoretical aspect of the work. The description of the theory behind GECP-method and its implementation is described in Chapter 2. Extensions to the current model are covered in Chapter 3 and its validation is discussed in Chapter 4. The second part is formed by the application of GECP to simulations of macroscopic phenomena in plasticity in Chapter 5. The final part is dedicated to a qualitative experimental validation of the simulation results and is given in Chapter 6.

The notations that will be used throughout this work are defined as follows. Bold capital letters denote tensors, bold lowercase letters denote vectors and lightface lowercase letters denote scalars. Given three second-order tensors \mathbf{A} , \mathbf{B} and \mathbf{C} and using Einstein's summation convention, the single contraction tensor product is written as $\mathbf{A} = \mathbf{B}\mathbf{C}$ with $C_{ij} = A_{ik}B_{kj}$. The dot-operator is omitted for readability. The double contraction tensor product is denoted using the colon operator as $d = \mathbf{A} : \mathbf{B} = A_{ij}B_{ij}$. The tensor product of two vectors \mathbf{m} and \mathbf{n} is defined as $\mathbf{A} = \mathbf{m} \otimes \mathbf{n}$ with $A_{ij} = m_in_j$. \mathbf{A}^{-1} and \mathbf{A}^T represent the inverse and transpose of a tensor \mathbf{A} , respectively. The gradient operator is used as $\nabla(\{\bullet\}) = \partial(\{\bullet\})/\partial\mathbf{x}$. Superscripts (α) and (β) denote properties of a slip system α and β , respectively.

2 | Constitutive framework of crystal plasticity

Within this chapter, the constitutive relations underlying the gradient-enhanced crystal plasticity model used in this work will be introduced. In crystal plasticity models, plastic deformation is assumed to occur due to dislocation slip on slip systems in the crystal lattice. A kinematic model that relates this crystallographic slip to the deformation of the crystalline material is discussed in Section 2.1. Based on this description, the constitutive relation between deformation and load is derived in Section 2.2. The material behaviour in the plastic regime, including the flow criteria and hardening behaviour, is further elaborated on in Section 2.3. The algorithmic implementation of the crystal plasticity model is described in Section 2.4.

2.1 Kinematical model of crystal deformation

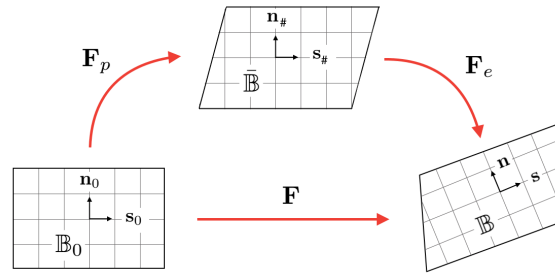


Figure 2.1: Schematic overview of the multiplicative decomposition $\mathbf{F} = \mathbf{F}_e \mathbf{F}_p$

The kinematical framework of finite-strain crystal plasticity models is commonly based on the multiplicative decomposition of the deformation gradient into an elastic and a plastic part, known as Kröner's decomposition:

$$\mathbf{F} = \mathbf{F}_e \mathbf{F}_p \quad (2.1)$$

In crystal plasticity, plastic deformation is caused by shearing of given slip systems in the materials. This shear deformation is a result of dislocation movement through the crystal lattice [23]. As plastic flow due to dislocation movement does not change the lattice structure, the intermediate configuration $\bar{\mathbb{B}}$ defined by \mathbf{F}_p is often assumed to leave the crystal lattice undistorted and unrotated. In this irrotational crystal plasticity formulation, the elastic part of the deformation accounts for all lattice distortions and rigid body rotations. A schematic overview of this decomposition is shown in Figure 2.1.

The deformation of a crystal with n possibly active slip systems $\alpha \in [1, 2, \dots, n]$ can be obtained by summing slip contributions on individual systems. For large deformations, *slips* are not well defined quantities, but *slip rates* are. The plastic deformation of crystalline materials is therefore formulated in terms of slip rates via the plastic velocity gradient [24]. As a result, the kinematical framework will be set up in terms of velocity gradients.

The plastic velocity gradient is defined as function of the slip rates $\dot{\gamma}^{(\alpha)}$ by

$$\mathbf{L}_p = \sum_{\alpha=1}^n \dot{\gamma}^{(\alpha)} \mathbf{n}_0^{(\alpha)} \otimes \mathbf{s}_0^{(\alpha)} \quad (2.2)$$

where the slip-plane normal $\mathbf{n}_0^{(\alpha)}$ and slip direction $\mathbf{s}_0^{(\alpha)}$ are constant vectors defined in the reference configuration. By noting that the resulting plastic deformation of a single slip step is small, the slip rates on individual slip systems α may be summed without taking into account the order of dislocation motion [5].

The total velocity gradient in the deformed configuration, $\mathbf{L} = \dot{\mathbf{F}}\mathbf{F}^{-1}$, can be additively decomposed into an elastic and a plastic part using $\mathbf{L} = \mathbf{L}_e + \mathbf{L}_p$. The plastic velocity gradient \mathbf{L}_p is mapped to the current configuration by the elastic rotation \mathbf{R}_e and the total velocity gradient is written as

$$\mathbf{L} = \mathbf{L}_e + \mathbf{R}_e \mathbf{L}_p \mathbf{R}_e^T \quad (2.3)$$

Substitution of (2.2) into (2.3) then gives

$$\begin{aligned} \mathbf{L} &= \mathbf{L}_e + \sum_{\alpha=1}^n \dot{\gamma}^{(\alpha)} \mathbf{R}_e \left(\mathbf{n}_0^{(\alpha)} \otimes \mathbf{s}_0^{(\alpha)} \right) \mathbf{R}_e^T = \mathbf{L}_e + \sum_{\alpha=1}^n \dot{\gamma}^{(\alpha)} \left(\mathbf{R}_e \mathbf{n}_0^{(\alpha)} \right) \otimes \left(\mathbf{R}_e \mathbf{s}_0^{(\alpha)} \right) \\ &= \mathbf{L}_e + \sum_{\alpha=1}^n \dot{\gamma}^{(\alpha)} \mathbf{n}^{(\alpha)} \otimes \mathbf{s}^{(\alpha)} \end{aligned} \quad (2.4)$$

by the orthogonality of \mathbf{R}_e . The deformation of the crystalline material is thus defined by the plastic slip on its various slip systems and elastic rotations of the crystal lattice. The formulation in (2.4) will be used to derive the constitutive relation for the crystal plasticity model in the subsequent section.

2.2 Stress response

Based on the result from (2.4), it can be seen that the deformation rate of a crystalline material can be decomposed into an elastic and a plastic part

$$\mathbf{D} = \mathbf{D}_e + \mathbf{D}_p \quad (2.5)$$

The plastic strain rate is given by the symmetric part of the plastic velocity gradient, $\mathbf{D}_p = \text{sym}(\mathbf{L}_p)$. From the definition in (2.2), it is found that

$$\mathbf{D}_p = \sum_{\alpha=1}^n \dot{\gamma}^{(\alpha)} \text{sym} \left(\mathbf{s}^{(\alpha)} \otimes \mathbf{n}^{(\alpha)} \right) = \sum_{\alpha=1}^n \dot{\gamma}^{(\alpha)} \mathbf{P}^{(\alpha)} \quad (2.6)$$

as expressed in the final configuration \mathbb{B} and by defining $\mathbf{P}^{(\alpha)}$ as the symmetric part of the Schmid tensor $\mathbf{s}^{(\alpha)} \otimes \mathbf{n}^{(\alpha)}$.

The objective rate for the Cauchy stress is now given by

$$\overset{\circ}{\boldsymbol{\sigma}} = \mathbb{C}_e : \mathbf{D}_e = \mathbb{C}_e : \left(\mathbf{D} - \sum_{\alpha=1}^n \dot{\gamma}^{(\alpha)} \mathbf{P}^{(\alpha)} \right) \quad (2.7)$$

by using $\mathbf{D}_e = \mathbf{D} - \mathbf{D}_p$. \mathbb{C}_e is the isotropic elastic stiffness tensor. With this expression, the constitutive relation for a crystal plasticity model capable of describing large rotations and large plastic deformations has been defined.

2.3 Material behaviour in the plastic regime

As discussed before, the plastic behaviour of the material takes place at the slip system level. Therefore, the evolution of the slip rates in (2.2) needs to be defined. Similar to conventional plastic material models, plastic slip is allowed when the shear stress on a slip system reaches an initial flow stress: the critical resolved shear stress. Upon further deformation, the resistance against deformation increases: slip systems harden by an increasing critical resolved shear stress. It has to be noted that no slip occurs on a slip system prior to exceeding the flow stress.

The evolution of the slip rates can both be described by phenomenologically as well as microstructurally-based models [12, 25]. For the first category of models, the critical resolved shear stress is updated as function of plastic slip. The latter category often uses a measure of the dislocation density within the material as internal variable to update the critical resolved shear stress. Within this work, a dislocation-density based crystal plasticity model will be used.

The flow behaviour of the slip systems is then governed by the flow criteria

$$\dot{\phi}^{(\alpha)} = \tau^{(\alpha)} - \tau_c^{(\alpha)}(\rho) \quad (2.8)$$

in which the critical resolved shear stress $\tau_c^{(\alpha)}$ is a function of the dislocation density ρ . The resolved shear stress $\tau^{(\alpha)}$ on a slip system α can be found using the symmetric part of the Schmid tensor according to

$$\tau^{(\alpha)} = \boldsymbol{\sigma} : \mathbf{P}^{(\alpha)} \quad (2.9)$$

2.3.1 Hardening behaviour

Hardening of a slip system due to the evolution of the dislocation density in the material can be described by the Taylor model

$$\tau_f = c\mu b\sqrt{\rho} \quad (2.10)$$

where τ_f is the flow stress, c is the Taylor factor, μ is the shear modulus and b is the Burgers vector length. A primary slip system can harden directly due to the formation of dislocations during a slip event of this system. A non-active, secondary slip system may experience hardening because of the generated dislocations by the primary slip too. This phenomenon is referred to as latent hardening and can be included in the Taylor model by the introduction of an interaction matrix $Q^{(\alpha\beta)}$ as function of six independent coefficients $Q_0^{(\alpha\beta)} \dots Q_5^{(\alpha\beta)}$ [10, 12]. In addition to the dislocation-induced hardening, a constant initial flow stress τ_0 representing the Peierls Nabarro stress is included. The critical resolved shear stress on a system α then follows from the dislocation densities on all systems β by

$$\tau_c^{(\alpha)} = \tau_0 + c\mu b \sqrt{\sum_{\beta=1}^n Q^{(\alpha\beta)} \rho^{(\beta)}} \quad (2.11)$$

Within a material, two types of dislocations can be distinguished. Statistically stored dislocations (SSDs) form during plastic deformation of the material by random trapping. When a crystal is subjected to inhomogeneous deformation, gradients of plastic slip arise. Geometrically necessary dislocations (GNDs) form as a result of such deformations in order to maintain compatibility in the crystal lattice. Following [10], the total dislocation density is calculated as

$$\rho^{(\alpha)} = \rho_{\text{SSD}}^{(\alpha)} + \rho_{\text{GND}}^{(\alpha)} \quad (2.12)$$

Due to their dependence on gradients of plastic slip, the presence of GNDs introduces a length scale in the crystal plasticity model, which renders the model size-dependent. This size-dependency would not have been present if only SSDs were included in the hardening model. Additionally, the presence of GNDs introduces a source of a remaining, inhomogeneous plastic deformation upon load removal. This is caused by the formation of equally-signed dislocation arrangements of which the net dislocation sign does not cancel out at the continuum level, where this is the case for the SSD-population. As introduced before, it is for these two reasons that a gradient-enhanced crystal plasticity model is believed to be able to capture macroscopic phenomena such as the Hall-Petch, Bauschinger and anelasticity effects.

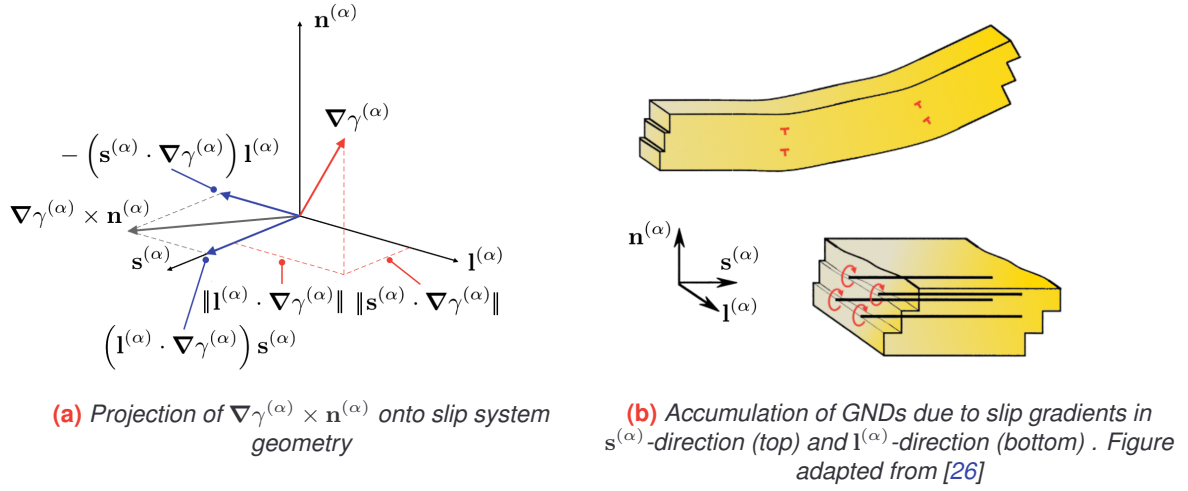


Figure 2.2: Relation between GNDs and curl of the plastic deformation gradient

Evolution of statistically stored dislocation densities

The evolution equation of the statistically stored dislocation density is given as function of the slip rates by

$$\dot{\rho}_{\text{SSD}}^{(\alpha)} = \frac{\dot{\gamma}^{(\alpha)}}{\gamma^{\infty}} \left(\rho_{\text{SSD}}^{\infty} - \rho_{\text{SSD}}^{(\alpha)} \right) \quad (2.13)$$

from which the value for ρ_{SSD} as function of the plastic slip can be obtained [12]:

$$\rho_{\text{SSD}}^{(\alpha)} = \rho_{\text{SSD}}^{\infty} \left[1 - \left(1 - \frac{\rho_{\text{SSD}}^0}{\rho_{\text{SSD}}^{\infty}} \right) \exp \left(-\frac{\gamma^{(\alpha)}}{\gamma^{\infty}} \right) \right] \quad (2.14)$$

Here, ρ_{SSD}^0 and $\rho_{\text{SSD}}^{\infty}$ are the initial and saturation densities of statistically stored dislocations, respectively. The parameter γ^{∞} determines the rate of saturation of the dislocation on the slip system.

Evolution of geometrically necessary dislocation densities

For the case of small deformation crystal plasticity, which is based on the additive decomposition of the deformation gradient

$$\mathbf{H} = \mathbf{H}_e + \mathbf{H}_p \quad (2.15)$$

the Burgers tensor is defined as [24]

$$\mathbf{G} = \text{Curl } \mathbf{H}_p \quad (2.16)$$

By assuming that the plastic distortion of a single crystal is solely caused by simple shear due to dislocation movement on given slip systems, the plastic deformation gradient can be written as

$$\mathbf{H}_p = \sum_{\alpha} \gamma^{(\alpha)} \mathbf{s}^{(\alpha)} \otimes \mathbf{n}^{(\alpha)} \quad (2.17)$$

where $\mathbf{s}^{(\alpha)}$ is the slip direction and $\mathbf{n}^{(\alpha)}$ is the slip system normal. Substitution of (2.17) into (2.16) yields

$$\mathbf{G} = \sum_{\alpha} \left(\nabla\gamma^{(\alpha)} \times \mathbf{n}^{(\alpha)} \right) \otimes \mathbf{s}^{(\alpha)} \quad (2.18)$$

which can be rewritten as [27]

$$\mathbf{G} = \sum_{\alpha} \left[\left(\mathbf{I}^{(\alpha)} \cdot \nabla \gamma^{(\alpha)} \right) \mathbf{s}^{(\alpha)} \otimes \mathbf{s}^{(\alpha)} - \left(\mathbf{s}^{(\alpha)} \cdot \nabla \gamma^{(\alpha)} \right) \mathbf{I}^{(\alpha)} \otimes \mathbf{s}^{(\alpha)} \right] \quad (2.19)$$

as apparent from Figure 2.2a. The terms $\mathbf{I}^{(\alpha)} \cdot \nabla \gamma^{(\alpha)}$ and $\mathbf{s}^{(\alpha)} \cdot \nabla \gamma^{(\alpha)}$ actually represent projections of the slip gradient $\nabla \gamma^{(\alpha)}$ on the slip system vectors $\mathbf{I}^{(\alpha)}$ and $\mathbf{s}^{(\alpha)}$, respectively. As seen in Figure 2.2b, a gradient of slip in the direction of $\mathbf{s}^{(\alpha)}$ gives rise to an accumulation of edge dislocations, whereas a slip gradient in $\mathbf{I}^{(\alpha)}$ requires an accumulation of screw dislocations. Using the definitions

$$\rho_{\text{GND},\odot}^{(\alpha)} = \mathbf{I}^{(\alpha)} \cdot \nabla \gamma^{(\alpha)} \quad \text{and} \quad \rho_{\text{GND},\ominus}^{(\alpha)} = -\mathbf{s}^{(\alpha)} \cdot \nabla \gamma^{(\alpha)} \quad (2.20)$$

the relation in (2.19) can thus be expressed in terms of the densities of geometrically necessary edge (\ominus) and screw (\odot) dislocations following [26]

$$\mathbf{G} = \sum_{\alpha} \left[\rho_{\text{GND},\odot}^{(\alpha)} \mathbf{s}^{(\alpha)} \otimes \mathbf{s}^{(\alpha)} + \rho_{\text{GND},\ominus}^{(\alpha)} \mathbf{I}^{(\alpha)} \otimes \mathbf{s}^{(\alpha)} \right] \quad (2.21)$$

Defining the Burgers tensor as in (2.16), a relation between the gradient of plastic slip and the densities of geometrically necessary dislocation can thus be derived. For the case of small deformations, gradients may be defined in the undeformed configuration and the directions of the vectors $\mathbf{s}^{(\alpha)}$ and $\mathbf{I}^{(\alpha)}$ can be assumed to remain unchanged. This makes that the dislocation densities can be calculated in a straightforward manner once the distribution of plastic slips throughout the material is known.

2.4 Algorithmic implementation

The numerical implementation of the stress-update component of the crystal plasticity code discussed in this work is based on the formulations of [10, 23, 28]. Herein, a fully implicit formulation is used to solve for the plastic slip increments. This algorithm includes an elastic check and the set of active slip systems is determined iteratively. Within this section, an overview of the underlying formulation of the stress-update algorithm is given. The discretization of the constitutive equations that forms the basis for the stress-update algorithm is discussed in Section 2.4.1. The algorithmic implementation of this discretization to determine the final stress state in a crystalline material is described in Section 2.4.2. The gradient computation procedure to determine the densities of GNDs in the material is outlined in Section 2.4.3. An overview of the FEM-implementation of the algorithm is provided in Section 2.4.4.

2.4.1 Discretizing constitutive equations

The basis for the formulation of a stress update algorithm is formed by discretizing the constitutive relations. The rate equation for the Cauchy stress in (2.7) is therefore rewritten in incremental form as

$$\Delta \boldsymbol{\sigma} = \mathbb{C}^e : \Delta \boldsymbol{\epsilon}^e = \mathbb{C}^e : (\Delta \boldsymbol{\epsilon} - \Delta \boldsymbol{\epsilon}^p) \quad (2.22)$$

using the rate of deformation tensor \mathbf{D} work-conjugate to the Cauchy stress to define the strain rate, $\dot{\boldsymbol{\epsilon}} = \mathbf{D}$. Integration of the plastic strain rate $\dot{\boldsymbol{\epsilon}}^p$ following the backward Euler method gives an expression for the plastic strain increment in terms of the plastic strain rate at the end of a step

$$\Delta \boldsymbol{\epsilon}^p \approx \dot{\boldsymbol{\epsilon}}_{n+1}^p \Delta t \quad (2.23)$$

in a fully implicit formulation. Insertion of the formulation of the flow rule $\dot{\boldsymbol{\epsilon}}^p = \sum_{\alpha=1}^n \dot{\gamma}^{(\alpha)} \mathbf{P}^{(\alpha)}$ into (2.23) yields the equation for the plastic strain increment

$$\Delta \boldsymbol{\epsilon}^p = \sum_{\alpha=1}^n \dot{\gamma}_{n+1}^{(\alpha)} \Delta t \mathbf{P}^{(\alpha)} \approx \sum_{\alpha=1}^n \Delta \gamma_{n+1}^{(\alpha)} \mathbf{P}^{(\alpha)} \quad (2.24)$$

Substitution of (2.24) in (2.22) gives the implicit stress update formulation

$$\boldsymbol{\sigma}_{k+1} = \boldsymbol{\sigma}_k + \Delta\boldsymbol{\sigma} = \boldsymbol{\sigma}^* - \mathbb{C}_e : \sum_{\alpha=1}^n \Delta\gamma_{k+1}^{(\alpha)} \mathbf{P}^{(\alpha)} \quad (2.25)$$

where the trial stress $\boldsymbol{\sigma}^*$ is defined as

$$\boldsymbol{\sigma}^* = \boldsymbol{\sigma}_n + \mathbb{C}_e : \Delta\boldsymbol{\epsilon}_n \quad (2.26)$$

in which the strain increment $\Delta\boldsymbol{\epsilon}_n$ is prescribed by the FEM-solver and $\boldsymbol{\sigma}_n$ is the previous equilibrium stress state of the material.

Based on the trial stress state and flow criteria values, either elastic or plastic deformation occurs. In the case of plasticity, accumulating plastic strain will affect the flow criteria due to hardening. This makes that in general, the expression for the stress update (2.25) has to be solved for using an iterative scheme. Two of such fully implicit schemes will be discussed in the remainder of this work.

2.4.2 Stress update algorithm with elastic check and active set determination

Miehe et. al. [28] have developed an implicit stress update algorithm in the constitutive framework of small strain single crystal plasticity. In the work of Soyarslan et. al. [10], it was extended to a finite-strain kinematical framework by including i.a. a lattice rotation update after a converged stress update step. The overall functioning of the stress update part of the code remains unchanged, however. Its implementation, together with the lattice rotation update will be described in this section. A flowchart of the algorithm is provided in Table C.2

Elastic check

Given the trial stress state $\boldsymbol{\sigma}^*$ obtained from (2.26), the resolved trial shear stress on a slip system α can be calculated using $\tau^{*(\alpha)} = \boldsymbol{\sigma}^* : \mathbf{P}^{(\alpha)}$. Based on the current value for the critical resolved shear stress $\tau_{c,k}^{(\alpha)}$, the flow criteria are evaluated in the elastic check

$$\phi^{*\alpha} = \boldsymbol{\sigma}^{(\alpha)} : \mathbf{P}^{(\alpha)} - \tau_{c,n}^{(\alpha)} < 0 \quad \forall \alpha \in (1, \dots, n) \quad (2.27)$$

If (2.27) is satisfied, the step is elastic. The returned tangent stiffness matrix is then set to \mathbb{C}^e and the final stress state equals the trial stress. Otherwise, plastic slip occurs and the Karush-Kuhn-Tucker conditions

$$\Delta\gamma^{(\alpha)} \geq 0, \quad \phi^{(\alpha)} \leq 0, \quad \Delta\gamma^{(\alpha)} \phi^{(\alpha)} = 0 \quad (2.28)$$

have to be satisfied. This is done using the following two steps.

Plastic slip update

The flow criteria are redefined in terms of the Cauchy stress as

$$r^{(\alpha)} \equiv \phi^{(\alpha)} = \boldsymbol{\sigma} : \mathbf{P}^{(\alpha)} - \tau_c^{(\alpha)}(\rho) \quad (2.29)$$

Given a fixed set \mathcal{A} of active slip systems, substitution of the expression of the stress at the end of the increment, (2.25), into (2.29) yields the expression for the approximated consistency conditions

$$\tilde{r}^{(\alpha)} = \boldsymbol{\sigma}^* : \mathbf{P}^{(\alpha)} - \sum_{\beta \in \mathcal{A}} \Delta\gamma_{k+1}^{(\beta)} \mathbf{P}^{(\beta)} : \mathbb{C}_e : \mathbf{P}^{(\alpha)} - \tau_{c,k}^{(\alpha)}(\rho) = 0 \quad (2.30)$$

For a fixed trial stress, (2.30) can be solved for the incremental plastic slips $\Delta\gamma^{(\alpha)}$ using the linearisation

$$r^{(\alpha)} - B^{(\alpha\beta)*} \Delta\gamma_{n+1}^{(\beta)} = 0 \quad (2.31)$$

with the Jacobian matrix

$$\overline{B^{(\alpha\beta)*}} \equiv -\frac{\partial r^{(\alpha)}}{\partial \gamma_{k+1}^{(\beta)}} = \mathbf{P}^{(\alpha)} : \mathbb{C}_e : \mathbf{P}^{(\beta)} + \frac{\partial \tau_c^{(\alpha)}}{\partial \gamma_{k+1}^{(\beta)}} \quad (2.32)$$

Using (2.31) and (2.32), a Newton-Raphson scheme is employed to iteratively update the values for the plastic slip. To be able to do so, the derivative of the critical resolved shear stress with respect to the plastic slip needs to be determined. The critical resolved shear stress is governed by the hardening behaviour of the slip systems and thus a function of ρ_{SSD} and ρ_{GND} . ρ_{SSD} is dependent on the plastic slip and the contribution

$$\frac{\partial \rho_{\text{SSD}}^{(\alpha)}}{\partial \gamma_{k+1}^{(\beta)}} = \frac{1}{\gamma_{\infty}} (\rho_{\text{SSD}}^{\infty} - \rho_{\text{SSD}}^0) \exp\left(-\frac{\gamma_{k+1}}{\gamma_{\infty}}\right) = \rho_{\text{SSD}}^{\infty} - \frac{\rho_{k+1}}{\gamma_{\infty}} \quad (2.33)$$

should thus be included in the last term in (2.32) as

$$\frac{\partial \tau_c^{(\alpha)}}{\partial \gamma_{k+1}^{(\beta)}} = \sum_{\beta \in \mathcal{A}} Q^{(\alpha\beta)} \left(\rho_{\text{SSD}}^{\infty} - \frac{\rho_{k+1}}{\gamma_{\infty}} \right) \frac{c\mu b}{2\sqrt{Q^{(\alpha\beta)} \rho_{k+1}^{(\beta)}}} \quad (2.34)$$

The incremental plastic slip values on each slip system can be calculated from $\Delta \gamma_{k+1}^{(\alpha)} = (B^{(\alpha\beta)*})^{-1} r^{(\beta)}$. For the case of isotropic hardening and equal resolved shear stresses on multiple systems, the Jacobian-matrix in (2.32) becomes singular and cannot be inverted. This problem is circumvented by applying a perturbation in the form of [28]

$$\left(B^{(\alpha\beta)} \right)^{-1} = \left(B^{(\alpha\beta)} + \epsilon \mathbf{I} \right)^{-1} \quad (2.35)$$

with

$$\epsilon = \min C \cdot \max_{1 \leq \alpha \leq n} \left\{ \sum_{\beta=1}^n |B^{(\alpha\beta)}| \right\} \quad (2.36)$$

in which $\min C$ is the machine accuracy with which the matrix inversion can be performed.

The first condition in (2.28) prescribes that all calculated plastic slip increments should be positive. In case of violation of this condition, the most violated system is stored. A modified update of the plastic slip values is performed using [23]

$$\gamma_{k+1}^{(\alpha)} = \gamma_k^{(\alpha)} + (1 - \theta) \Delta \gamma_{k+1}^{(\alpha)} \quad (2.37)$$

with

$$\theta = \min_{\alpha \in \mathcal{A}} \left(1 - \frac{\gamma_k^{(\alpha)}}{\Delta \gamma_{k+1}^{(\alpha)}} \right) \quad (2.38)$$

From the incremental plastic slip, the new total plastic slip is updated as $\gamma_{k+1}^{(\alpha)} = \gamma_k^{(\alpha)} + \Delta \gamma_{k+1}^{(\alpha)}$. The new plastic strain is found as $\epsilon_{p,k+1} = \sum_{\alpha \in \mathcal{A}} \gamma_{k+1}^{(\alpha)} \mathbf{P}^{(\alpha)}$. Following $\sigma_{k+1} = \sigma^* - \mathbb{C}_e : \epsilon_{p,k+1}$, the stress state at the end of the iteration is found.

This new stress state can be used again to calculate the resolved shear stresses on the slip systems, obtain the updated flow criteria and redo the calculations of the Jacobian matrix. This iterative scheme is employed until convergence has been reached, as defined by

$$\sum_{\alpha \in \mathcal{A}} \|r_{k+1}^{(\alpha)}\| / \sum_{\alpha \in \mathcal{A}} \|r_0^{(\alpha)}\| \leq \text{tol} \quad (2.39)$$

where $r_0^{(\alpha)}$ is the residual before the first iteration and tol is a predefined error tolerance.

Active set update

Before starting the Newton-Raphson iterations, the active set \mathcal{A} needs to be determined. As first estimate, this set is taken as the final set of active systems during the previous FEM-iteration. The plastic slip update procedure is performed. In case

$$\sum_{\alpha \in \mathcal{A}} r^{(\alpha)} \Delta \gamma^{(\alpha)} < 0 \quad (2.40)$$

the system that originally most violated the condition $\Delta \gamma^{(\alpha)} \geq 0$ is removed from the active set and the calculation procedure is repeated until (2.40) is no longer violated [10, 23]. If due to the updated solution from the Newton-Raphson scheme, any $\phi^{(\alpha)} > 0$ for systems not in the active set, the maximum loaded system is added to the active set and the calculation procedure is repeated [28]. For an empty initial set, all systems where $\phi^{(\alpha)} > 0$ are added to \mathcal{A} .

Elastoplastic moduli

After convergence of the Newton-Raphson loop, the final stress state that has to be passed back to the FEM-solver is known. Additionally, the tangent stiffness matrix needs to be computed. This is done using the Jacobian matrix calculated for the converged stress state according to

$$\mathbb{C}^{ep} = \mathbb{C}^e - \sum_{\alpha=1}^n \sum_{\beta=1}^n B^{(\alpha\beta)*-1} \left(\mathbb{C}^e : \mathbf{P}^{(\alpha)} \right) \otimes \left(\mathbf{P}^{(\beta)} : \mathbb{C}^e \right) \quad (2.41)$$

Lattice rotation update

To obtain the resolved shear stress on a slip system, the components of the stress tensor are projected onto this system using the Schmid tensor. Herein, the orientations of the lattice vectors that make up this tensor are important. It is thus required to keep track of the amount of rotation that the lattice vectors undergo while the material is being deformed.

The additive decomposition of the total velocity gradient as defined in (2.4) can be simplified if elastic strains are assumed to have a negligibly small influence on lattice rotations. Its elastic part is then solely defined by the elastic spin tensor \mathbf{W}_e , as described in detail in Appendix A. The additive decomposition of the total velocity gradient in accordance with the rigid-plastic assumption can then be written as

$$\mathbf{L} = \mathbf{W}_e + \mathbf{R}_e \mathbf{L}_p \mathbf{R}_e^T = \mathbf{W}_e + \sum_{\alpha} \dot{\gamma}^{(\alpha)} \mathbf{n}^{(\alpha)} \otimes \mathbf{s}^{(\alpha)} \quad (2.42)$$

The skew-symmetric part of (2.42) gives the total spin tensor. Using the approximation $\Delta \mathbf{R}_e = \exp(\mathbf{W}_e) = \exp(\mathbf{W} - \mathbf{W}_p)$, the relation

$$\mathbf{R}_e^{t+1} = \Delta \mathbf{R} \mathbf{R}_e^t \quad (2.43)$$

yields the total elastic rotation by subtracting the plastic spin \mathbf{W}_p , calculated in the stress-update algorithm, from the total spin at the end of the time step \mathbf{W} , as known from the FEM-solver, as [29]:

$$\mathbf{R}_e^{t+1} = \exp \left(\mathbf{W} - \sum_{\alpha} \dot{\gamma}^{(\alpha)} \text{skw} \left[\mathbf{n}^{(\alpha), t} \otimes \mathbf{s}^{(\alpha), t} \right] \right) \mathbf{R}_e^t \quad (2.44)$$

The updated Schmid tensor can now be found from

$$\mathbf{P}^{(\alpha), t+1} = \mathbf{R}_m \mathbf{R}_e^{t+1} \mathbf{P}^{(\alpha), t} \mathbf{R}_e^{t, T} \mathbf{R}_m^T \quad (2.45)$$

where \mathbf{R}_m is the material orientation matrix which defines the lattice orientation with respect to the global reference frame as in Section E.1.

2.4.3 Gradient and GND-density calculations

Gradients of plastic slip are computed from differences in slip between neighbouring integration points. As these points in general do not form a uniform grid, the calculation procedure from [30] is used. Herein, an application of the finite difference method to calculate gradients at irregular grids is proposed. Consider a central integration point \mathbf{r}_0 located at coordinates $\{x_0, y_0, z_0\}$. The first order Taylor series expansion of the plastic slip $\gamma^{(\alpha)}$ around this point with respect to a point $\mathbf{r} = \{x, y, z\}$ is written as

$$\gamma^{(\alpha)}(\mathbf{r}) = \gamma^{(\alpha)}(\mathbf{r}_0) + \boldsymbol{\Upsilon} \cdot (\mathbf{r} - \mathbf{r}_0) \quad (2.46)$$

with the unknown gradient vector $\boldsymbol{\Upsilon} = \left\{ \frac{\partial \gamma^{(\alpha)}(\mathbf{r}_0)}{\partial x}, \frac{\partial \gamma^{(\alpha)}(\mathbf{r}_0)}{\partial y}, \frac{\partial \gamma^{(\alpha)}(\mathbf{r}_0)}{\partial z} \right\}^T$. Now, this equation is set up for every integration point within a predefined search radius s [10]. To avoid an overdetermined set of equations, the norm

$$\mathbb{D} = \sum_{k=1}^n \left[\frac{\gamma^{(\alpha)}(\mathbf{r}_0) - \gamma^{(\alpha)}(\mathbf{r}_k) + \boldsymbol{\Upsilon} \cdot (\mathbf{r}_k - \mathbf{r}_0)}{\|\mathbf{r}_k - \mathbf{r}_0\|^3} \right]^2 \quad (2.47)$$

is minimised using $\partial \mathbb{D} / \partial \boldsymbol{\Upsilon} = 0$.

The gradient calculations are programmed in an Abaqus USDFLD subroutine. The script stores all integration point coordinates, upon which it determines per point which other integration points lie within the search radius. Only points belonging to the same grain will be considered. Per integration point, these neighbours are used to create the system of equations in (2.46) and solve for the gradients of slip per slip system. The GND-densities are then calculated using (2.20). This implementation of the gradient computations was originally proposed for irrotational crystal plasticity, as lattice rotations are not considered. Its applicability in the finite-strain framework will be more elaborately discussed in Section 3.3.

2.4.4 Finite Element implementation

The stress-update algorithm and gradient calculation scripts are not simultaneously active in the current implementation of the crystal plasticity finite element method. The USDFLD subroutine is called twice each increment of the Abaqus solver, performing different tasks at the start and the end of the increment. This is schematically outlined in Table 2.1.

Gradients of plastic slip are only computed at the end of the increment, after the stress-update algorithm has converged. GND densities are calculated accordingly. At the start of the next increment, the previously computed GND densities are assigned to the material's state variables. Using these values, the stress update algorithm programmed in the UMAT subroutine is able to calculate the GND-induced hardening terms. A small unbalance is thus introduced within each increment to be corrected in the subsequent one [10]. The assignment of the neighbouring points used for the gradient computations for each central Gauss point, is performed only at the start of the first increment for computational efficiency.

Table 2.1: Implementation of gradient computations and stress-update algorithm within global FEM-increments

Incremental calculation sequence	
Increment 1:	
USDFLD:	for all integration points, determine set of neighbouring points to be used in gradient calculations
UMAT:	perform global stress update iterations perform lattice rotation update
USDFLD:	compute slip gradients $\nabla\gamma^{(\alpha)}$ and GND-densities ρ_{GND}
...	
Increment n:	
USDFLD:	assign GND-densities ρ_{GND} to state variables
UMAT:	perform global stress update algorithms using updated state variables perform lattice rotation update
USDFLD:	compute slip gradients $\nabla\gamma^{(\alpha)}$ and GND-densities ρ_{GND}
Increment $n + 1$:	
USDFLD:	assign GND-densities ρ_{GND} to state variables
UMAT:	perform global stress update algorithms using updated state variables perform lattice rotation update
USDFLD:	compute slip gradients $\nabla\gamma^{(\alpha)}$ and GND-densities ρ_{GND}
...	

The implementation in Table 2.1 features the implicit, rate-independent finite-strain stress update algorithm from Section 2.4.2. In absence of the gradient computation script, it can thus be used to describe arbitrarily large deformations. It is important to note that up to this point, the gradient-enhanced crystal plasticity formulation is not applicable in finite-strain problems. The formulation of the Burgers tensor in (2.21) limits the validity of the GND-computations in Section 2.4.3 to applications involving small-deformations. The prerequisites for the finite-strain application of the gradient-enhanced crystal plasticity model will be discussed in Section 3.3.

3 | Extensions to the crystal plasticity model

This chapter provides an overview of extensions and adaptations that were made to the theoretical framework of the crystal plasticity model. Building upon the algorithmic framework introduced in Section 2.4.2, an alternative approach for multi-surface stress update algorithms is proposed in Section 3.1. Herein a method is developed which solves the stress update for all slip systems simultaneously without elastic check and iterative active set update. The calculation algorithm for the gradients of slip described in Section 2.4.3 is extended in two ways. At first, it is made suitable for use in combination with periodic RVEs in Section 3.2. The small strain gradient calculations that originate from Section 2.3.1 are examined for applicability within a finite-strain formulation in Section 3.3, to obtain a gradient-enhanced crystal plasticity model that can be used to describe arbitrary large deformations.

3.1 Stress update algorithm without elastic check and active set determination

As discussed in Section 2.4.2, the original stress update algorithm only enters the Newton-Raphson loop if the flow criterium for at least one system is larger than 0. For the elastic case, this loop is omitted, the plastic slip increments are set to 0 and the elastoplastic moduli are taken as the elastic ones. This requires an additional check in the algorithm and involves a manual adaptation of the plastic parameters.

Due to the method of updating the active set, the Newton-Raphson iterations may have to be performed multiple times in one load step. It is even possible that the same active set is solved for multiple times during the return mapping process. This results in a higher computational time and introduces the possibility for the algorithm to get stuck in an endless loop, iterating between the same active sets. It thus becomes clear that it is desirable to develop a solution method that is capable of solving the plastic slip parameters for all possible slip systems at once and return positive slip values only for systems exceeding their respective flow criteria. By not assigning plastic slip to inactive systems, the elastic check can be omitted. Solving the entire set of possible systems removes the necessity of defining an active set and its iterative update method.

In a conventional return mapping algorithm, the stress state is updated such that all flow criteria equal 0 in case of plastic flow. If one would omit the elastic check and employ the same algorithm for a stress state in the elastic domain, it will extrapolate an admissible elastic stress to the yield surface. This implies the condition $\phi = 0$ for both elastic as well as plastic deformation, instead of $\phi < 0$ for elastic and $\phi = 0$ for plastic deformation. A possibility to circumvent this problem is by introducing a modified expression for the flow criteria such that

$$\tilde{\phi}^{(\alpha)} = \max(0, \phi^{(\alpha)}) \quad (3.1)$$

(3.1) thus replaces the elastic check described in Section 2.4.2 and automatically defines the active set. However, the $\max()$ function is not continuously differentiable. This is an undesirable property in the definitions of the Jacobian in the Newton-Raphson scheme and the elastoplastic moduli, where derivatives of the modified flow criteria with respect to $\phi^{(\alpha)}$ are required. A suitable, continuously differentiable approximation for the $\max()$ function will thus have to be found for the development of the new algorithm. This aspect will be discussed in detail in Appendix B. Its implementation in the algorithm described in Section 2.4.2 and the required modifications will be considered in Section 3.1.1.

3.1.1 Implementation of modified flow criteria in stress update algorithm

With the continuously differentiable function that approximates (3.1) chosen to be $\bar{\phi} = \frac{\phi}{2} \left(1 + \tanh \left(\frac{\phi}{q} \right) \right)$, the Newton-Raphson scheme for updating the plastic parameters can be defined. The calculation steps that were outlined in Section 2.4.2 will be retained. Where needed, the algorithmic expressions are adapted. As a starting point, the approximated consistency conditions are redefined as

$$\tilde{r}^{(\alpha)} = \frac{1}{2} \tilde{r}_0^{(\alpha)} \left(1 + \tanh \left(\frac{\tilde{r}_0^{(\alpha)}}{q} \right) \right) \quad (3.2)$$

where $\tilde{r}_0^{(\alpha)}$ is similar to (2.30), but now obtained by taking the sum over all possible slip systems:

$$\tilde{r}_0^{(\alpha)} = \boldsymbol{\sigma}^* : \mathbf{P}^{(\alpha)} - \sum_{\beta=1}^n \Delta \gamma_{k+1}^{(\beta)} \mathbf{P}^{(\alpha)} : \mathbb{C}_e : \mathbf{P}^{(\beta)} - \tau_{c,k}^{(\alpha)}(\rho) = 0 \quad (3.3)$$

The linearised equation that is iteratively solved for is still of the form

$$r^{(\alpha)} - B^{(\alpha\beta)*} \Delta \gamma_{n+1}^{(\beta)} = 0 \quad (3.4)$$

but now the contribution of the approximation function (3.2) has to be taken into account in the Jacobian matrix:

$$\begin{aligned} B^{(\alpha\beta)*} &\equiv - \frac{\partial r^{(\alpha)}}{\partial \gamma_{k+1}^{(\beta)}} = - \frac{\partial r^{(\alpha)}}{\partial r_0^{(\alpha)}} \frac{\partial r_0^{(\alpha)}}{\partial \gamma_{k+1}^{(\beta)}} = \frac{\partial r^{(\alpha)}}{\partial r_0^{(\alpha)}} B_0^{(\alpha\beta)*} \\ &= \frac{1}{2} \left(1 + \tanh \left(\frac{\tilde{r}_0^{(\alpha)}}{q} \right) + q^{-1} \cosh^{-2} \left(\frac{\tilde{r}_0^{(\alpha)}}{q} \right) \right) B_0^{(\alpha\beta)*} = A^{(\alpha)} B_0^{(\alpha\beta)*} \end{aligned} \quad (3.5)$$

in terms of the original Jacobian $B_0^{(\alpha\beta)}$ as defined in (2.32) and the scalar factor $A^{(\alpha)}$. In case the inversion of the Jacobian-matrix is a problem, the perturbation of (2.35) is performed on $B^{(\alpha\beta)*}$.

The plastic slip parameters now follow again from $\Delta \gamma_{k+1}^{(\alpha)} = (B^{(\alpha\beta)*})^{-1} r^{(\beta)}$. It is however possible that the calculated plastic slip on some of the slip systems is not admissible in the sense $r^{(\alpha)} \Delta \gamma^{(\alpha)} < 0$. For these systems, the residual $r^{(\alpha)}$ and the corresponding rows and columns in $B^{(\alpha\beta)}$ are set to zero and $\Delta \gamma_{k+1}^{(\alpha)}$ is calculated using this updated set of equations. This update is based on the system dropping update discussed in Section 2.4.2, with the difference that it is performed within a Newton-Raphson iteration instead of after completing all iterations. The incremental plastic slip on the originally violated systems will be set to 0 by this correction.

The updated plastic slips $\gamma_{k+1}^{(\alpha)} = \gamma_k^{(\alpha)} + \Delta \gamma_{k+1}^{(\alpha)}$ are used to calculate the updated plastic strains, stress state and flow criterion values as described in Section 2.4.2. The updated flow criterion values are checked against (2.39) to determine the convergence of the Newton-Raphson loop.

In case the solution has converged, the consistent elastoplastic moduli are calculated. In its original formulation, the expression for the elastoplastic moduli is based on the inverted Jacobian $B_0^{(\alpha\beta)*^{-1}}$ that was obtained in the Newton-Raphson calculations. In the modified algorithm, this Jacobian is not directly available as it is replaced by the formulation $A^{(\alpha)} B_0^{(\alpha\beta)*}$ in (3.5). Therefore, the original Jacobian is obtained by applying the manipulation

$$B^{(\alpha\beta)*^{-1}} = \left(A^{(\alpha)} B_0^{(\alpha\beta)*} \right)^{-1} = A^{(\alpha)^{-1}} B_0^{(\alpha\beta)*^{-1}} \Rightarrow B_0^{(\alpha\beta)*^{-1}} = A^{(\alpha)} B^{(\alpha\beta)*^{-1}} \quad (3.6)$$

from which (2.41) can be rewritten as

$$\mathbb{C}^{ep} = \mathbb{C}^e - \sum_{\alpha=1}^n \sum_{\beta=1}^n A^{(\alpha)} B^{(\alpha\beta)*^{-1}} \left(\mathbb{C}^e : \mathbf{P}^{(\alpha)} \right) \otimes \left(\mathbf{P}^{(\beta)} : \mathbb{C}^e \right) \quad (3.7)$$

A note on computational efficiency

Using the modified algorithmic expressions described above, the plastic slip parameters are solved for all possible systems at once. This however does not mean that information of all systems is required at all times. When calculating the incremental plastic slips using (3.4), the entire system

$$\mathbf{B}^* \Delta \boldsymbol{\gamma}_{n+1} = \mathbf{r} \quad (3.8)$$

is solved. The residual vector \mathbf{r} may however contain many zero-entries due to the definition of (3.2). As a result, corresponding incremental slips will also remain zero. The solution procedure can be speeded up significantly by exploiting the sparsity of \mathbf{r} . Following the calculation of the current residuals $\tilde{r}^{(\alpha)}$, only the rows and columns of \mathbf{B}^* corresponding to non-zero entries in \mathbf{r} are calculated. $\Delta \boldsymbol{\gamma}$ is initialised as the $n \times 1$ -zero vector. The entries that should be assigned a plastic slip are updated by solving the reduced system

$$B^{(\alpha\beta)*} \Delta \gamma_{n+1}^{(\beta)} = r^{(\alpha)} \quad (3.9)$$

with $\{\alpha \in (1, \dots, n) \mid r^{(\alpha)} > 0\}$ and $\{\beta \in (1, \dots, n) \mid r^{(\beta)} > 0\}$. This reduces the number of calculation steps required in the definition of the Jacobian matrix and the computational time for solving the system of equations. As setting the residual of the violated systems to 0 represents a further reduction of the set of equations, the aforementioned method is still applicable with the system dropping update for inadmissible plastic slips. It should be noted that (3.9) does not fix the active set. The current active set is redefined after every update of r and thus during each iteration.

The reduced Jacobian matrix can also be used in calculating the elastoplastic moduli in (3.7) by only summing over system indices with positive flow criteria values. This further reduces the computational time as only contribution of currently active systems are taken into account.

The flow charts for both versions of the algorithm are shown in Tables C.1 and C.2 for comparison of the calculation steps in Appendix C.

3.1.2 Comparison of the algorithms

To compare the functioning of both versions of the algorithm, it will be tested on various levels. At first, simulations are performed on material point level, i.e. one single (integration) point at which stresses and strains are calculated following a prescribed loading. After these initial tests, the stress-update algorithms are implemented in the FEM-software Abaqus by means of a user material (UMAT) routine. Within this section, the outcomes of the various tests will be summarised in order to compare both codes in terms of efficiency and stability.

Simulations on material point level

Simulations at the material point level are performed using a dedicated driver script, which can take as input a prescribed stress or strain state or a predefined deformation gradient. It is also possible to set a combined loading option. Here, certain strain components are specified and the stresses in undeformed directions are kept zero. The script thus mimics the iterative solution procedure performed by a FEM-solver per integration point. The stability of the algorithms is best tested by using a prescribed stress state or the combined loading option. As the stress-update algorithms are strain driven, these load types generally require multiple iterations to find the deformation state that matches the prescribed loading.

The loading condition and material parameters used for testing are given in Table 3.1 (simulation 1). The evolution of the active set for the single load step simulation is graphically depicted in Figure 3.1. In both codes, the first increment is elastic and no systems are active. In the second load step, systems 17 and 20 become active. In the subsequent increments, the initially active set is larger, but reduces to $\mathcal{A} = [17, 20]$ after several system dropping updates. The original code performs these updates slower

Table 3.2: FEM-results for testing the implementation of the modified stress-update algorithm

Algorithm	Lattice rotation angles			Max. stress [MPa]	# increments	# iterations	CPU time [s]
	ϕ_1	Φ	ϕ_2				
Original	0	0	0	179.7	105	106	134.69
Modified	0	0	0	179.7	105	106	198.91
Original	0.3	0.2	0.5	336.0	105	116	140.74
Modified	0.3	0.2	0.5	335.3	107	123	212.16
Original	0	0.5	0.2	194.0	105	106	138.97
Modified	0	0.5	0.2	192.0	541	1804	22559.8

Simulations on FEM level

To test the functioning of the modified stress-update code in solving finite element models, it is implemented as user material model in Abaqus. A 100 x 100 mm square shell is meshed with 2.5 x 2.5 mm plane stress quadratic quadrilateral elements. The part is subjected to a 5 % uniaxial strain. Material parameters are identical to Table 3.1 except for the lattice rotations and the Young's modulus, which is set to 78 GPa. Three simulations are performed, each with lattice rotation angles as defined in Table 3.2.

For each simulation, the Von Mises stress distribution is compared between both versions of the algorithm. For the top left element, results are extracted for integration point 1 to be able to compare the evolution of the plastic slips. Results of the simulations are provided in Figures 3.2 to 3.4 and Table 3.2. It is clearly seen that for an increasing amount of lattice rotation, which is for observed most severely in Figure 3.4, the results of both algorithms start to differ. Also, the calculation time for the modified algorithm increases significantly.

To investigate the cause of this problem, the strain state of the first integration point of the top left element was input in the material point driver and the development of the active set was tracked. It was observed that the active set and the components of the elastoplastic stiffness tensor fluctuated severely. This behaviour was found to be caused by the update of the active set in case of negative plastic slips, as defined under item 4(b) of Table C.2. Previously active and admissible sets can be rendered inactive by this update at once, leading to severe changes in the active set and premature convergence of the Newton-Raphson iterations. It must be noted that the original algorithm suffers from the same convergence issues if the active set prediction is turned off. In general, the modified algorithm converges and yields the same results as the original code if this version can converge without active set prediction.

3.2 Gradient calculations in periodic models

Periodic boundary conditions are often applied to Representative Volume Elements (RVEs) used in crystal plasticity simulations. These are rectangular (2d) or box shaped (3d) FE representation of a polycrystalline material and consist out of a limited amount of grains. These grains may be cut by the boundaries of the RVE. Cut-off parts are continued at the opposed edge of the RVE. For a more elaborate discussion of these topics, the reader is referred to Section 5.1.

Recalling the gradient calculation procedure outlined in Section 2.4.3, gradients are calculated from neighbouring integration points within the same grain. A neighbouring point is taken into account in the calculations if its distance to the central integration point is less than a predefined search radius. However, if a cut grain is continued at the opposite side of the model, integration points from that region may never lie within the search radius and will thus not be included in the calculations. This causes gradients near the RVE-boundaries to be essentially based upon one-sided difference schemes instead of a more accurate two-sided scheme. Therefore, an extension to the gradient script for application to two-dimensional periodic RVEs has been developed.

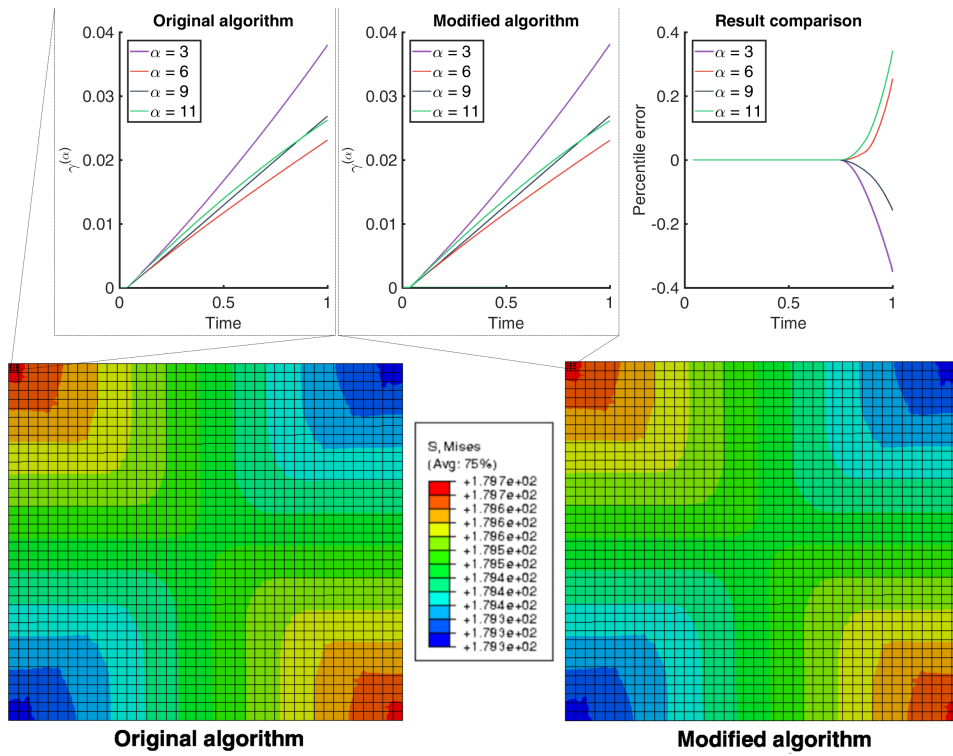


Figure 3.2: Comparison of the FEM-results obtained using both stress-update algorithms. Plastic slip evolution is displayed for integration point 1 of the top left element. Lattice rotation angles 0, 0, 0 radians

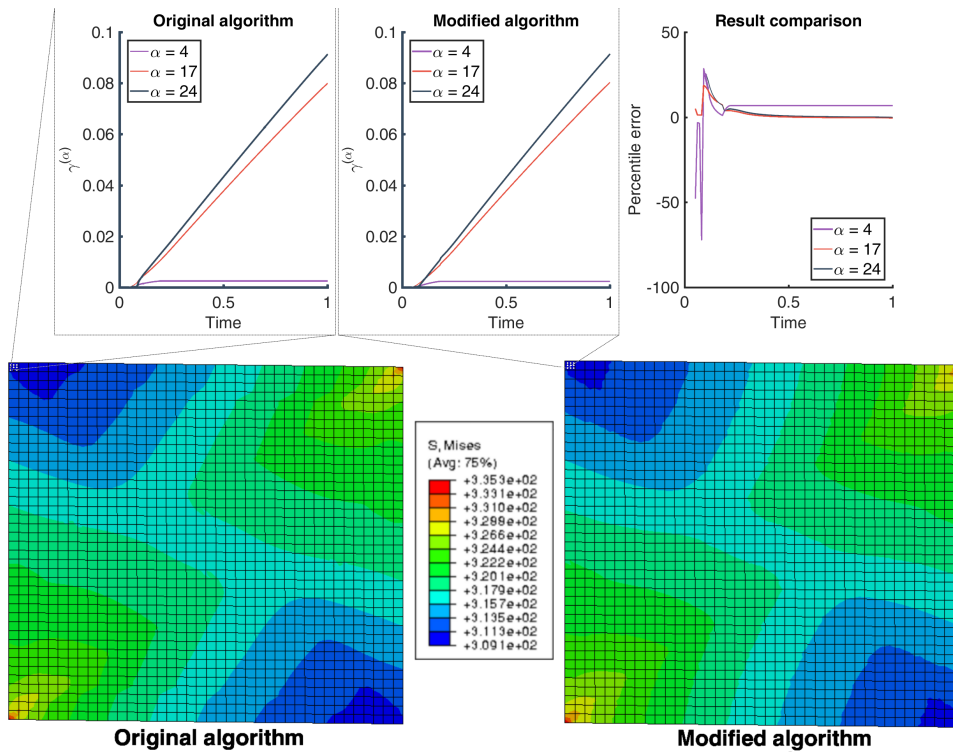


Figure 3.3: Comparison of the FEM-results obtained using both stress-update algorithms. Plastic slip evolution is displayed for integration point 1 of the top left element. Lattice rotation angles 0.2, 0.3, 0.5 radians

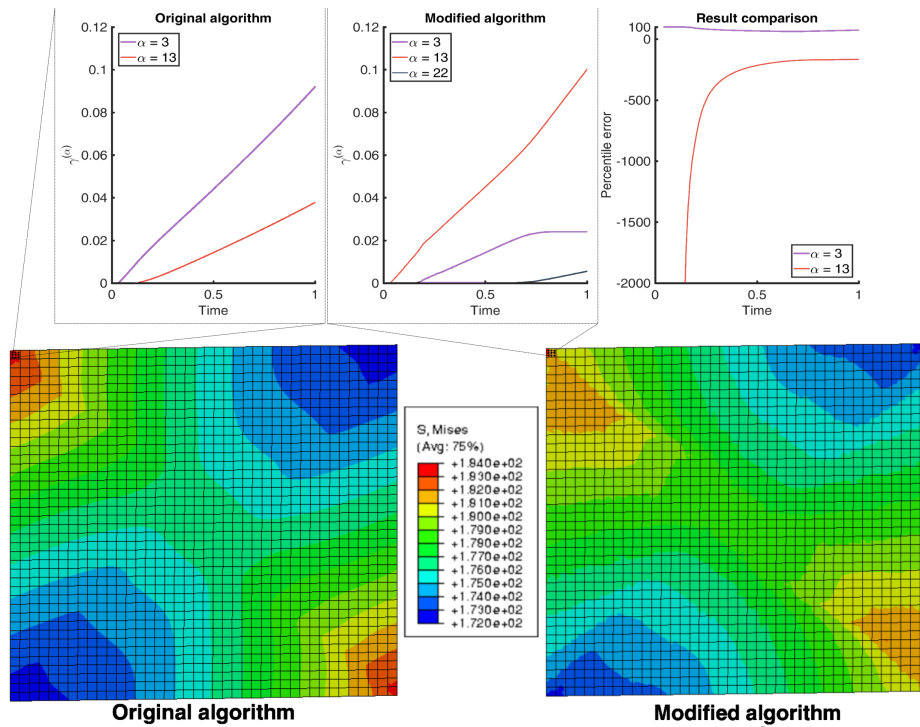
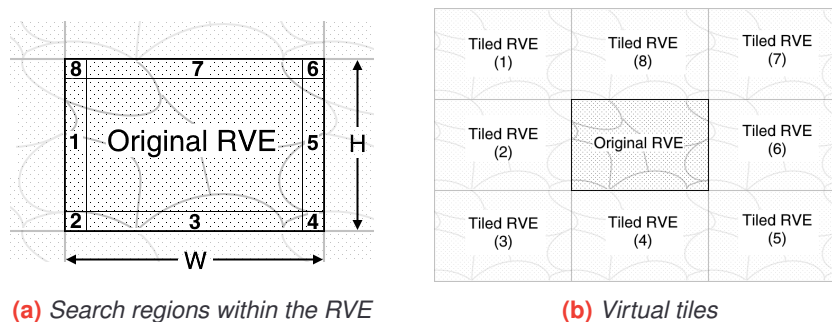


Figure 3.4: Comparison of the FEM-results obtained using both stress-update algorithms. Plastic slip evolution is displayed for integration point 1 of the top left element. Lattice rotation angles 0, 0.5, 0.2 radians

Within the original RVE, a fictitious inner rectangle is drawn at an offset to the outer shape with the size of the search radius s . The area between the two rectangles is divided into eight search regions, as shown in Figure 3.5a. Additionally, a number of eight tiles is identified as indicated in Figure 3.5b. Integration points that lie within the eight search regions will be mapped to the tiles by coordinate transformations. For instance, a point within region 1 is mapped to tile 6 by the shifting vector $\{W, 0\}^T$. A point in region 4 is mapped to tiles 8, 1 and 2 using the transformations $\{0, H\}^T$, $\{-W, H\}^T$ and $\{-W, 0\}^T$, respectively. This mapping is handled in the initialisation step of the gradient script in the first FE-increment as in Table 3.4.

The gradient calculation step is essentially left unaltered. The only difference with respect to the original formulation is that for shifted integration points, the distance to the central integration point is calculated from the shifted coordinates, whereas the slip data is extracted from the corresponding integration point in the original RVE. This is outlined in Table 3.3.



(a) Search regions within the RVE

(b) Virtual tiles

Figure 3.5: Search regions and tiles required for periodic gradient calculations

3.2.1 Comparison of the gradient codes

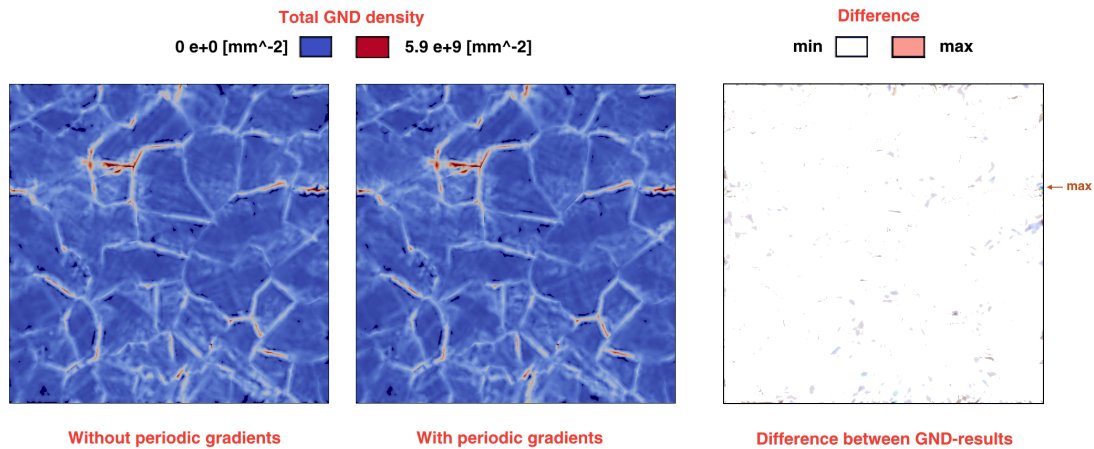


Figure 3.6: Comparison between GND density distribution calculated with and without periodic slip gradients

Figure 3.6 shows the total GND density as calculated by the gradient script using both the non-periodic as well as the periodic implementation. The intensity plot on the right indicates the difference between both colour plots. The higher the colour intensity of this plot, the greater the difference in GND density. The RVE depicted here consists of 29 grains with different orientations and a FCC-lattice. It is subjected to uniaxial tension in horizontal direction. As it serves the sole purpose of providing a qualitative comparison between the methods, further details about the model are omitted.

The majority of the distribution is the same in both colour plots, as expected from the fact that only points near the outside of the RVE are affected by the modified calculations. The greatest differences are indeed observed in this outer region, as indicated by the intensity plot. The small islands of negative GND densities, indicated in dark blue and visible near the RVE edges in the left plot, are removed by adding the periodic calculations. As a result, no colour differences between opposed edges are found anymore. The GND distribution is thus fully periodic now. The differences that are found in the interior grains are caused by slight changes of the response to the macroscopic loading caused by differences in hardening in the exterior grains.

Table 3.3: Modified calculation step for periodic gradient computations. *Modifications shown in blue*

Pseudo-code for calculation step
For each original integration point j Loop over integration points k that were identified to lie within search radius of point j : If k is a shifted integration point: 1. Get number of original integration point k_i corresponding to the shifted coordinate 2. Calculate gradient of slip based on distance between points j and k and slip values at points j and k_i Else: Calculate gradient of slip based on distance between points j and k and slip values at points j and k

Table 3.4: Modified initialisation step for periodic gradient computations. *Modifications shown in blue*

Pseudo-code for initialisation step
<p>Loop over all integration points:</p> <ol style="list-style-type: none"> 1. Store grain number 2. Store integration point coordinates (original array length equals number of integration points n_{IP}) 3. If integration point is within one of the search regions: <ol style="list-style-type: none"> (a) Perform coordinate shift using shifting vector(s) corresponding to the search region (b) Append shifted coordinate to the list of integration point coordinates (c) Store number of original integration point corresponding to the shifted coordinate <p>Loop over all original integration points $j \in [1 : n_{IP}]$:</p> <ol style="list-style-type: none"> 1. If grain number of j equals that of k and distance between j and k is less than the search radius s: <p style="margin-left: 40px;">Store k in vector containing all integration points within search radius of integration point j</p> 2. If integration point j is within one of the search regions: <p style="margin-left: 40px;">Loop over all remaining entries $k' > n_{IP}$ within coordinate list:</p> <ol style="list-style-type: none"> (a) Get number of original integration point k_i corresponding to the shifted coordinate (b) If grain number of j equals that of k_i and distance between j and k' is less than the search radius: <p style="margin-left: 40px;">Store k' in vector containing all integration points within search radius of integration point j</p>

3.3 Determining GND-densities in a finite-strain formulation

In a general finite strain framework, especially when large rotations are present, the simplifications mentioned in Section 2.3.1 are no longer valid. This may affect the calculation procedure of the GND-densities. Within this section, the theoretical framework of GND-density evolution in a finite-strain framework will be examined. Comparison of these results with the formulations in Section 2.3.1 will provide insight into the extent to which these formulations can be applied when simulations are to be performed that exceed the assumption of small deformations.

Within the finite strain setting, proper attention must be paid to the relations between plastic slips distributions and slip system orientations between the different configurations shown in Figure 2.1. As introduced before, the finite-deformation crystal plasticity framework is given by the multiplicative decomposition of the total deformation gradient as

$$\mathbf{F} = \mathbf{F}_e \mathbf{F}_p \quad (3.10)$$

to describe the mapping from the reference space B_0 to the observed space B via the intermediate configuration \bar{B} , representing the lattice space [31]. If a unit normal vector in the reference configuration is denoted as \mathbf{n}_0 and its counterpart \mathbf{n} is given in the final configuration, the unit lattice normal is defined in terms of the elastic and plastic deformation gradients as

$$\mathbf{n}_\# = \frac{\mathbf{F}_p^{-T} \mathbf{n}_0}{|\mathbf{F}_p^{-T} \mathbf{n}_0|} = \frac{\mathbf{F}_e^T \mathbf{n}}{|\mathbf{F}_e^T \mathbf{n}|} \quad (3.11)$$

The Burgers vector in reference configuration is defined as [32]

$$\mathbf{b}_p(S) = \int_{\partial S_0} \mathbf{F}_p dx_0 = \int_{S_0} (\text{Curl } \mathbf{F}_p)^T \mathbf{n}_0 dA_0 \quad (3.12)$$

Using the relations in (3.11), $\mathbf{n}_0 dA_0 = \mathbf{F}_p^T \mathbf{n}_\# dA_\#$, and (3.12) rewrites to

$$\mathbf{b}_p(S_\#) = \int_{S_\#} (\text{Curl } \mathbf{F}_p)^T \mathbf{F}_p^T \mathbf{n}_\# dA_\# \quad (3.13)$$

The term $\left[(\text{Curl } \mathbf{F}_p)^T \mathbf{F}_p^T \right]^T$ is referred to as the Burgers tensor \mathbf{G} and provides a measure for the Burgers vector in the intermediate configuration via \mathbf{G}^T . The plastically convected rate of \mathbf{G} is defined as

$$\overset{\square}{\mathbf{G}} = \dot{\mathbf{G}} - \mathbf{L}_p \mathbf{G} - \mathbf{G} \mathbf{L}_p^T \quad (3.14)$$

By substituting the plastic velocity gradient $\mathbf{L}_p = \sum_{\alpha=1}^n \dot{\gamma}^{(\alpha)} \mathbf{n}_\#^{(\alpha)} \otimes \mathbf{s}_\#^{(\alpha)}$, it follows that

$$\overset{\square}{\mathbf{G}} = \sum_{\alpha} \left[\left(\nabla_{\#} \dot{\gamma}^{(\alpha)} \times \mathbf{n}_\#^{(\alpha)} \right) \otimes \mathbf{s}_\#^{(\alpha)} \right] \quad (3.15)$$

in which $\nabla_{\#} \dot{\gamma}^{(\alpha)}$ represents the gradient of plastic slip in the lattice space. Gurtin [31] shows that by using the relations $\mathbf{l}_\#^{(\alpha)} = \mathbf{n}_\#^{(\alpha)} \times \mathbf{s}_\#^{(\alpha)}$ and the orthogonality of $\nabla_{\#} \dot{\gamma}^{(\alpha)} \times \mathbf{n}_\#^{(\alpha)}$ to $\mathbf{n}_\#^{(\alpha)}$, (3.15) can be decomposed as

$$\begin{aligned} \overset{\square}{\mathbf{G}} &= \sum_{\alpha} \left[\left(\mathbf{l}_\#^{(\alpha)} \cdot \nabla_{\#} \dot{\gamma}^{(\alpha)} \mathbf{s}_\#^{(\alpha)} - \mathbf{s}_\#^{(\alpha)} \cdot \nabla_{\#} \dot{\gamma}^{(\alpha)} \mathbf{l}_\#^{(\alpha)} \right) \otimes \mathbf{s}_\#^{(\alpha)} \right] \\ &= \sum_{\alpha} \left[\dot{\rho}_{\text{GND},\odot}^{(\alpha)} \mathbf{s}_\#^{(\alpha)} \otimes \mathbf{s}_\#^{(\alpha)} + \dot{\rho}_{\text{GND},\vdash}^{(\alpha)} \mathbf{l}_\#^{(\alpha)} \otimes \mathbf{s}_\#^{(\alpha)} \right] \end{aligned} \quad (3.16)$$

into rates of change of densities of geometrically necessary edge (\vdash) and screw (\odot) dislocations. He concludes therefore that temporal changes in the Burgers tensor may be characterised by the temporal changes in dislocation densities on the material's slip systems. These changes in dislocation densities are governed by the gradient of the plastic slip rates in the lattice as

$$\dot{\rho}_{\text{GND},\odot}^{(\alpha)} = \mathbf{l}_\#^{(\alpha)} \cdot \nabla_{\#} \dot{\gamma}^{(\alpha)} \quad \text{and} \quad \dot{\rho}_{\text{GND},\vdash}^{(\alpha)} = -\mathbf{s}_\#^{(\alpha)} \cdot \nabla_{\#} \dot{\gamma}^{(\alpha)} \quad (3.17)$$

Gradient calculations can however only be performed in the reference and spatial configuration using the current algorithm. It would be beneficial if these calculations could be retained, i.e. there is no need to include the lattice space. Using the identities

$$\nabla_{\#} = \mathbf{F}_p^{-T} \nabla_0 = \mathbf{F}_e^T \nabla \quad \text{and} \quad \mathbf{l}_\# = \mathbf{F}_p \mathbf{l}_0 = \mathbf{F}_e^{-1} \mathbf{l} \quad \text{and} \quad \mathbf{s}_\# = \mathbf{F}_p \mathbf{s}_0 = \mathbf{F}_e^{-1} \mathbf{s} \quad (3.18)$$

and (3.17), it is found that

$$\begin{aligned} \dot{\rho}_{\text{GND},\odot}^{(\alpha)} &= (\mathbf{F}_p \mathbf{l}_0) \cdot \left(\mathbf{F}_p^{-T} \nabla_0 \dot{\gamma}^{(\alpha)} \right) & \dot{\rho}_{\text{GND},\odot}^{(\alpha)} &= (\mathbf{F}_e^{-1} \mathbf{s}) \cdot \left(\mathbf{F}_e^T \nabla \dot{\gamma}^{(\alpha)} \right) \\ &= (\mathbf{l}_0 \mathbf{F}_p^T) \cdot \left(\mathbf{F}_p^{-T} \nabla_0 \dot{\gamma}^{(\alpha)} \right) & &= (\mathbf{s} \mathbf{F}_e^{-T}) \cdot \left(\mathbf{F}_e^T \nabla \dot{\gamma}^{(\alpha)} \right) \\ &= \mathbf{l}_0^{(\alpha)} \cdot \nabla_0 \dot{\gamma}^{(\alpha)} & &= \mathbf{l}^{(\alpha)} \cdot \nabla \dot{\gamma}^{(\alpha)} \end{aligned} \quad (3.19)$$

since $\mathbf{F}_p^T \mathbf{F}_p^{-T} = \mathbf{F}_e^{-T} \mathbf{F}_e^T = \mathbf{I}$. Similarly, $\dot{\rho}_{\text{GND},\vdash}^{(\alpha)} = -\mathbf{s}_0^{(\alpha)} \cdot \nabla_0 \dot{\gamma}^{(\alpha)} = -\mathbf{s}^{(\alpha)} \cdot \nabla \dot{\gamma}^{(\alpha)}$.

This is an important observation, as it implies that GND densities do not need to be calculated in the lattice space. They can be calculated in both the reference as well as the spatial configuration without loss of generality. The only prerequisite for this is that the lattice vector onto which the slip gradients are projected are expressed in the same frame as the gradients. The gradient calculation procedure outlined in Section 2.4.3 is thus not limited to small deformations. It can be applied in a finite strain formulation unmodified if referential gradients are used. The representation of lattice vectors, as specified by the grain orientations, in the reference space is namely already implemented. If spatial gradients are to be used, an additional rotation of these vectors is required to map them to the observed space. This can be done by pre-multiplying the lattice vectors by the elastic rotation matrix \mathbf{R}_e obtained from the lattice rotation update in Section 2.4.2:

$$\mathbf{l}^{(\alpha)} = \mathbf{R}_e \mathbf{l}_0^{(\alpha)} \quad \text{and} \quad \mathbf{s}^{(\alpha)} = \mathbf{R}_e \mathbf{s}_0^{(\alpha)} \quad (3.20)$$

3.4 Conclusions and recommendations

A modified version of the stress update algorithm developed by Miehe et. al. [28] has been proposed, solving for the entire set of slip systems at once without an initial elastic check. Several continuously differentiable approximations of the $\max()$ -function were tested for this purpose. The tanh-smoothing function proved to be the most suitable approximation function. It is concluded that for problems with small lattice rotations, the modified algorithm yields the same results as the original formulation. In system dropping updates, the final active set is found faster. For problems involving large rotations and requiring system adding updates, the active set cannot be maintained robust enough and modifications are needed.

A method to resume from previously converged active sets is thus to be developed. Additionally, the handling of the constraint $\gamma^{(\alpha)} \geq 0$ should be revised. This can be done by penalizing negative incremental slips, for instance by including a suitable penalty method in the dissipation maximisation problem that underlies the formulation of the stress-update algorithm. Input files for the material point driver that can be used for further improvement of the algorithm are attached in Appendix D.

The gradient computation script has been made applicable for use with periodic RVEs. A method based on two-dimensional shifting of the integration point coordinates to virtual tiled RVEs was used. To improve computational efficiency, only points that lie within the gradient search radius of the RVE's outer boundaries are shifted. The modified computation script was compared to the original formulation in a uniaxial tensile tests on a 29-grain RVE with FCC crystals and realistic texture. It was shown that the overall GND distribution remains virtually unaffected. Jumps in GND density that were originally observed between opposed edges of the RVE, were removed by the periodic gradient calculations, rendering the GND distribution to be fully periodic too. This increases the accuracy of the simulations.

A review of finite-strain formulations for the evolution of GND-densities from literature has pointed out that GNDs can be characterised also for large deformations without the necessity of retrieving the lattice configuration. Both spatial as well as referential gradients of slip rates can be used to calculate GND-densities, as long as these gradients are projected onto representations of lattice vectors within the same coordinate frame. It is therefore not necessary to add extra functionality to the USDFLD-subroutine for GND-calculations. Its ability to calculate referential gradients, together with the availability of lattice vectors expressed in reference configuration, makes it applicable for finite-strain applications.

4 | Verification of the crystal plasticity model

The purpose of this chapter is to assess the validity of the algorithmic implementation of the crystal plasticity model. Two aspects will be considered for this purpose. At first, the lattice rotation update as was described in Section 2.4.2 will be verified in Section 4.1. Furthermore, the functioning of different formulations of the crystal plasticity model in both small- as well as finite-strain applications will be addressed in Section 4.2.

4.1 Verification of the lattice rotation update

The lattice rotation update from Section 2.4.2 provides an approximation for the total elastic rotation of the slip systems following a converged stress update step. In Abaqus, it is possible to directly obtain the (incremental) rotation of the frame in which stress and strain components are expressed by using the *UMAT* input variable *drot*. This corresponds to the rigid rotation of the material frame based on the total deformation. For small plastic deformation, this rotation converges to the rotation measure calculated in the stress update algorithm.

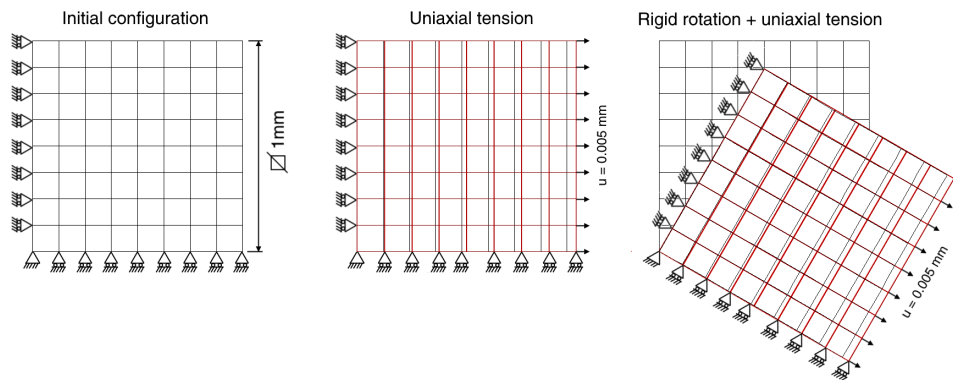


Figure 4.1: Models used for verification of the lattice rotation update

The two measures are compared to verify the ability of the lattice rotation update in the stress update algorithm to handle large rigid rotations. Three simulations are performed on a 1x1 mm square plane strain model meshed with 8 x 8 quadratic quadrilateral elements as shown in Figure 4.1:

1. Uniaxial tension up to 0.5% strain without lattice rotation update
2. Rigid body rotation of -30° , followed by 0.5% uniaxial tensile strain using the lattice update from Section 2.4.2 ($\mathbf{R}^{t+1} = \Delta \mathbf{R} \mathbf{R}_e^t$)
3. Rigid body rotation of -30° , followed by 0.5% uniaxial tensile strain using the *drot* lattice update ($\mathbf{R}^{t+1} = \text{drot} \mathbf{R}_e^t$)

By its implementation in the stress update algorithm, the rotation update from Section 2.4.2 is available immediately before the GND densities are calculated. The corresponding Abaqus measure becomes available at the start of the new increment, thus after the GND densities have been calculated. This implies a mismatch in lattice update at the moment that GNDs are calculated. GNDs have been turned off in order to rule such differences.

Both rotation update methods yield virtually identical results, as seen in Figure 4.2. As required, no influence of the rigid body rotation is observed in the final results. Difference between the results of simulation 1 and those of simulations 2 and 3 originate from lack of rotation update in the former. The results from simulations with lattice rotation update thus converge to the small-strain formulation in simulation 1 for small stretch. It can be concluded that the lattice rotation update used in the stress-update algorithm is implemented correctly to handle large rigid rotations and yields the desired results.

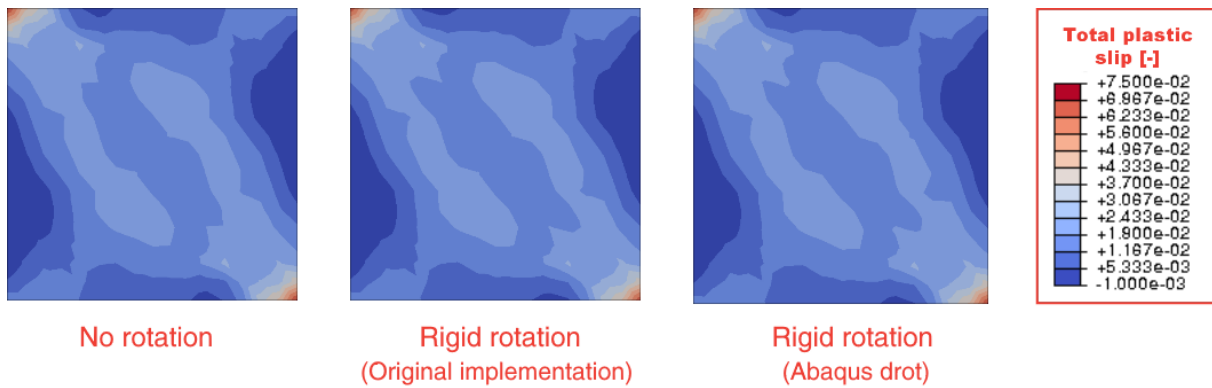


Figure 4.2: Total accumulated plastic slip from the lattice rotation update verification simulations

4.2 Verification of the finite strain implementation

The crystal plasticity method can be implemented in different ways as seen in Figure 4.3. For the case of irrotational crystal plasticity, in which the lattice frame $\mathcal{O}_\#$ is assumed to be attached to the material, implementations differ between small-strain and geometrical nonlinear frameworks. In the former, the orientations of the material frame and reference frame are assumed to be identical throughout the simulation. As a result, no lattice rotation update has to be performed. The orientation of the lattice vectors follows directly from the grain orientations as defined by the rotation matrix \mathbf{R}_m ($\mathcal{O}_m \rightarrow \mathcal{O}_\#$).

Implementation of irrotational crystal plasticity in a geometrically nonlinear framework, in which the material orientations are updated each increment, requires rotation of the lattice vectors too. For this purpose, the lattice rotation update in the stress-update algorithm is used. With the resulting elastic rotation matrix, the lattice vectors are rotated along with the material. Gradients of plastic slip and projection of the slip gradients onto the lattice to obtain the GNDs densities is now to be performed in the spatial configuration. Only then the calculation of the GNDs densities remains relative to the material frame in the same manner as in the small strain formulation.

Within the finite strain framework that was developed by Gurtin [31] and discussed in Section 3.3, it was shown that calculation of GNDs can be performed with respect to the reference lattice configuration. Slip gradients are thus calculated in and projected onto lattice vectors in the reference configuration, given by the grain orientation rotation matrix \mathbf{R}_m . A correct projection of the stresses onto lattice vectors in determining the resolved shear stress however does require a lattice rotation update. As stress tensor components are expressed in the spatial representation of the material frame \mathcal{O}_m , the lattice vectors are accordingly rotated along with this frame by the elastic rotation matrix in the stress update algorithm.

The differences between the possible implementations are investigated using a constrained simple shear test. A 1x1 mm square plane strain model, meshed with 30 x 30 quadratic quadrilateral reduced integration elements is sheared to 50% strain. Displacements on the bottom edge are constrained, while a pure horizontal displacement of 0.5 mm is prescribed on the top edge. The resulting stress-strain curves are provided in Figure 4.4.

The response of the small-strain simulation predicts the lowest increase in stress. When turning the geometrical nonlinearity option on, the stress increase with strain is larger. This can be explained by the re-orientation of the material frame during each step. For the small strain case, the deformation state is that of pure shear. For the geometrically nonlinear case, a tensile component is added as deformation proceeds. This results in higher stresses. In the vicinity of small deformations (up to $\approx 5\%$ strain), all formulations yield virtually identical results. This is an important observation for the verification of the large-deformation implementations.

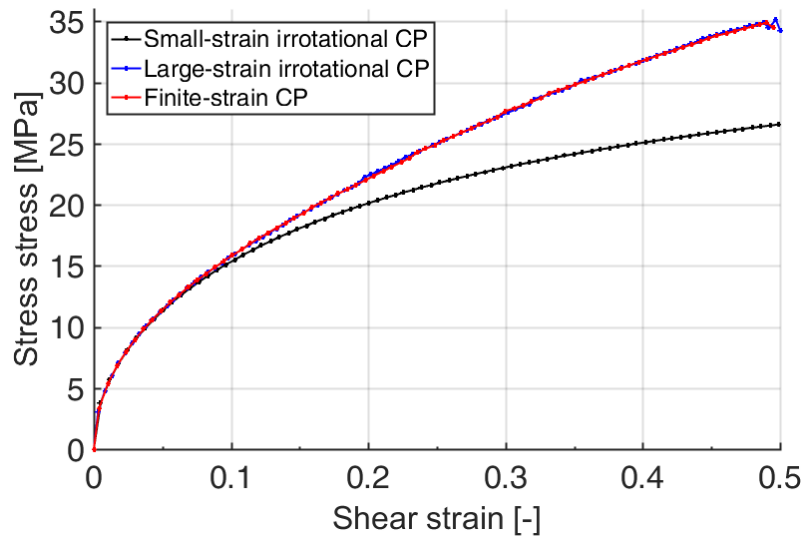


Figure 4.4: Stress-strain curves for the different implementations

4.2.1 Conclusion

The lattice rotation update as approximated by the exponent of the incremental elastic spin tensor was compared to the measure for rigid body rotations in Abaqus. As both measures give the same results in a tensile test following a rigid body rotation, the functioning of the lattice rotation update was verified. The behaviour of three possible implementations of the gradient enhanced crystal plasticity model was simulated in a simple shear test. All implementations provide results that meet expectations. Both large-strain formulations converge to the small-strain results in the vicinity of small strain, which is an important verification criterion. GND calculations resulting from referential as well as spatial gradients yield the same outcomes. This verifies their implementations. The finite-strain implementation based on referential slip gradients is argued to be most robust with respect to modelling assumptions and convergence errors.

5 | Predicting macroscopic phenomena using a gradient-enhanced crystal plasticity model

In the introduction, three macroscopic phenomena were identified as difficult to be represented by continuum models. These are the Hall-Petch effect, the Bauschinger effect and anelasticity. This section is dedicated to the simulation of these phenomena using a gradient enhanced crystal plasticity model. They will be separately treated in Sections 5.2 to 5.3 in the order in which they are listed above. Each section will contain a short introduction that describes the phenomenon and possibilities of modelling it, followed by an introduction of the simulations, numerical results and a discussion of the findings. Per phenomenon, a partial conclusion on the applicability of gradient-enhanced crystal plasticity in representing it will be formulated.

Details about the FEM-models used for simulations are presented separately per section, but general modelling aspects will be outlined in Section 5.1 first. Detailed information about the generation of the representative volume elements is limited to Section 5.2.2.

5.1 Modelling aspects

For simulating the macroscopic behaviour of a material using a crystal plasticity model, analysis are often performed on a Representative Volume Element (RVE). Such an RVE consists of only a limited amount of grains, as computational time does not yet allow for the simulation of full structures composed out of multiple grains. The size of the RVE is to be chosen small enough to ensure that extracted results are representative for a single material-point of a full-size structure. On the other hand, a sufficient number of grains should be included to capture the macroscopic behaviour of the material, i.e. its response does not change upon adding further grains to the model [33].

Closely related to the number of grains is the distribution of crystallographic orientations. Especially for a limited number of grains, care must be taken to ensure that the individual grain orientations result in a satisfactory uniform distribution of grain orientations in the polycrystal RVE [34]. The better such uniform distribution is captured, the better the generated model will be able to capture the macroscopic material behaviour.

Besides specifying the grain morphology in terms of size, grain number and orientations, appropriate boundary conditions have to be selected to ensure the RVE response is representative for its macroscopic counterpart. Kraska et. al. [35] distinguish three types of boundary conditions. For *homogeneous deformation*, all nodes are displaced such that the deformation field within the RVE is uniform. Using *homogeneous boundary conditions*, only the nodal boundaries are prescribed using the global strain field. For *periodic boundary conditions*, all interior nodes are free, but boundary nodes are related such that the model is periodic in all its dimensions. Deformations are prescribed within the constrain equations that relate opposing nodes.

All of the three aforementioned boundary conditions can be used to exactly prescribe an overall deformation. Periodic boundary conditions however pose the least restrictions to the anisotropic deformation of the different grains [35]. As most macroscopically observed phenomena in the plastic deformation of polycrystalline materials are believed to be caused by this crystal anisotropy, all simulations performed in this work are subjected to periodic boundary conditions.

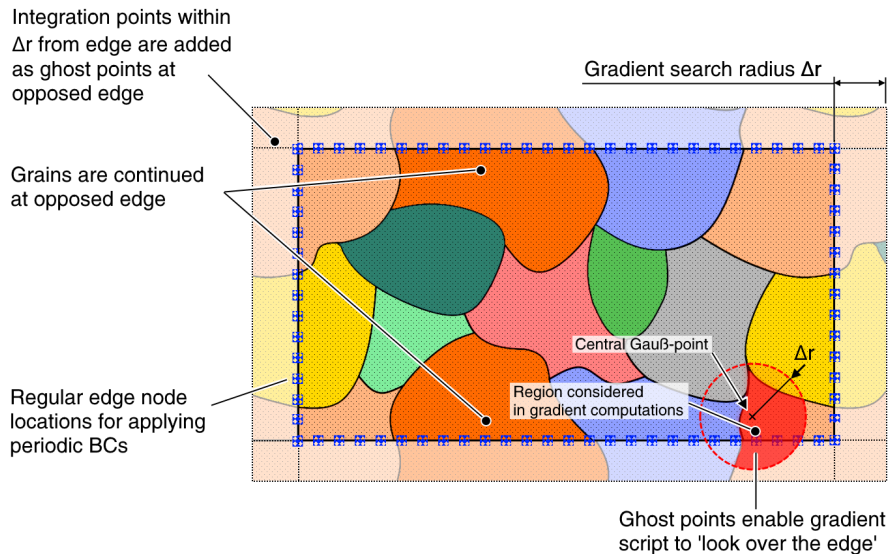


Figure 5.1: Schematic overview of the implications of periodicity on the generation of an RVE

A correct application of periodic boundary conditions poses additional constraints on the generation of RVEs and their finite element models, as seen in Figure 5.1. If a grain is cut by one of the RVE edges, the cut-off part must be continued from the opposed edge. Only then, a model is created that can be unlimitedly tiled. The Python code for generating the RVEs take this requirement into account during creation of the grains and material assignment. Furthermore, it is required that nodes on parallel edges of the RVE share the same coordinate along the length of the edge. This condition is enforced by seeding the exterior edges using a regular pattern during mesh generation. The periodic gradient computation script from Section 3.2 is used. All integration points no further away from the edge than the search radius of the gradient calculation script, are therefore added as ghost points near the opposed edge. The search radius is set to one-fourth of the incircle radius of the grains.

Within this work, RVEs consisting out of equally sized, hexagonal grains are used. This allows for exact control over the grain size. Furthermore, it is ensured no effects resulting from the presence of texture or grain size mismatches in realistic microstructures are affecting the results. Thus, any difference between simulations arises from the constitutive model and is not related to the statistics of the microstructure. The generation method and structure of the RVEs is discussed briefly in the subsequent sections. Where needed, further details are elaborated on in the discussion of the simulation procedures of the investigated phenomena.

5.1.1 RVE with hexagonal grains

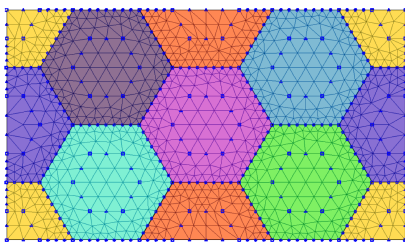


Figure 5.2: RVE with 8 hexagonal grains.
Corresponding colours indicate identical material assignment and crystal orientation.
Symbols show location of mesh seeds.

For the generation of RVEs with hexagonal grains, a rectangular face is partitioned by a set of tiled hexagons. To be able to create a periodic model, only full, half and quarter hexagonal sections may be present. Hexagon quarters are located at the corners of the model, full and half sections are alternated along the edges of the rectangle, as seen in Figure 5.2. Due to the geometrical constraints posed by this grain layout, the size of the RVE cannot be specified directly. The model dimensions are controlled by the number of grains along the horizontal and vertical direction of the model and the edge length of the hexagons instead.

Each full hexagon is assigned a material and grain orientation. Grains cut by the model edges are thus continued at the opposite side of the RVE, as visualised by the colours in Figure 5.2. As due to the mismatch in lattice orientations between adjacent grains, most incompatibility based effects take place near the grain boundaries, a finer mesh is required near those boundaries. The grain boundaries are meshed by specifying the number of equidistantly spaced nodes along the edges of the hexagons. Additionally, a smaller hexagon is constructed within each grain. Its size and number of nodes along its edges can be used to control the mesh in the grain interior. A Python script ran through Abaqus CAE is used to automatically generate and mesh the hexagonal grains, assign material parameters and crystal orientations and generate the required constraint equations for the periodic boundary conditions.

5.2 The Hall-Petch effect

The macroscopic behaviour of polycrystalline materials is determined, among other things, by the size of its grains. In general, a material with finer grains is harder and exhibits a higher initial yield stress than a material with coarse grains. In the 1950s, Hall and Petch independently found an identical relation between yield strength and grain size:

$$\sigma_y = \sigma_0 + k/\sqrt{d} \quad (5.1)$$

It was found a Hall-Petch-like relation can also be used for indentation hardness, cleavage fracture stress and ductile-brittle transition temperature [36]. Several models have been proposed for justifying the Hall-Petch relation and as an attempt to find an expression for the Hall-Petch constant. The majority of this models explicitly makes use of the abovementioned dependency on the inverse of the square root of the grain size. However, recent comparisons of large sets of available data have shown that the Hall-Petch relation in its original form may be questioned, as the experimental data could also be related to the grain size using other relations (e.g. by a simple reciprocal or logarithmic function) and the proposed theoretical predictions of the Hall-Petch constant are insufficient [37].

The grain size-dependency of the yield stress and work hardening behaviour, where smaller grains imply a stronger and harder material, is nevertheless still acknowledged. The Hall-Petch effect can thus at least be regarded as a general size effect. A Hall-Petch relation, extended to the full work-hardening regime, that is in line with these findings can be written as [12]:

$$\sigma_y(\epsilon) = \sigma_0(\epsilon) + k(\epsilon)d^{-n} \quad (5.2)$$

in which the Hall-Petch exponent n may take a wider range of values than the original -0.5.

5.2.1 The Hall-Petch effect in crystal plasticity models

Several attempts to model the Hall-Petch behaviour using the crystal plasticity method have been published in literature. Most authors add a size dependency by means of including GNDs in the hardening model. Often, the GND density is determined using the gradient of plastic slip ([6, 12, 34, 38]). Haouala et. al. however calculate the GND density as function of the distance to the grain boundary [15]. Evers et. al. [13] have proposed a composite model, in which grains are split in core and boundary volumes. By enforcing the average deformation gradient in corresponding boundary elements from two adjacent grains to equal the globally prescribed average deformation gradient, a mismatch in lattice orientation between the core and boundary volume is created. The GND-density is calculated as function of this disorientation. This however implies that no presence of GNDs in the core region is possible and the ratio between core and boundary volumes must be determined from experimental data.

By including GNDs in the crystal plasticity model, a size-dependent hardening behaviour is obtained. For fine grained materials, the work hardening rate becomes higher. The effect on work hardening rate was found similar to that observed in experiments in the work of Becker [12]. The initial yield stress however remains unchanged, as the dislocation densities do not develop prior to plastic deformation.

Several authors try to capture the Hall-Petch behaviour at yield by initialising dislocation densities. Cheong et. al. [38] fit the simulation results to experimental data by including and scaling an initial SSD-distribution. In their scaling approach, they however directly introduce the square root dependency on the grain size. Counts. et. al. [34] introduce preliminary kinematics, in which an undistorted single crystal is transformed to a grain in a polycrystalline material. Based on the deformation gradients in the preliminary kinematics, an initial GND density is calculated. In the paper of Evers et. al. [6], the mismatch in orientation of adjacent grains in the undeformed configuration is used to initialise the GND density. The latter two approaches obtain a qualitative representation of the Hall-Petch effect at yield, but the resulting Hall-Petch exponents still differ from the experimentally observed values. It must however be noted that the size-dependent yield stress is found without explicitly including a length scale.

From the conclusions drawn in literature, it is found no modelling of the precise interaction mechanisms at the grain boundaries is required to capture a size-dependent stress-strain response. Including a size-dependency in the work hardening relations by means of GNDs is sufficient to render the work hardening behaviour size-dependent. To model a size-dependent transition between elastic and plastic deformation with this approach, a realistic initial dislocation density is required. As the gradient-enhanced crystal plasticity formulation discussed in this work includes a length scale in the evolution of GNDs, it should be possible to observe a different hardening behaviour for different grains sizes. As no initialisation method for the dislocation densities is included, the elastic-plastic transition is expected to remain unchanged though.

The following research question is formulated to investigate the applicability of the crystal plasticity method in predicting the Hall-Petch effect in metals:

Research Question 1.1

To what extent can size-dependent stress-strain behaviour of a material be predicted solely by including GNDs as function of slip gradients in the crystal plasticity framework?

5.2.2 Setting up the FEM-models

The simulations within this section are partly inspired by the approach described by Becker to investigate the Hall-Petch effect in polycrystalline materials [12, p. 135]. In his work, a 12 grain, rectangular RVE with realistic microstructure is subjected to a uniaxial tensile deformation under plane strain conditions. This deformation is obtained by vertically constraining one edge of the RVE and prescribing a horizontal displacement at the opposed edge. The average grain size is varied by scaling the dimensions of the RVE, while keeping the morphology of the grains constant. Simulation results are compared to experimental stress-strain curves for pure aluminium with average grain sizes of 34, 88, 240 and 500 μm . The material parameters are obtained by fitting the numerical stress-strain response to the experimental data for the largest grain size. This set of parameters is then used for simulating the smaller grain sizes. Becker obtains an almost perfect agreement with the experimental data.

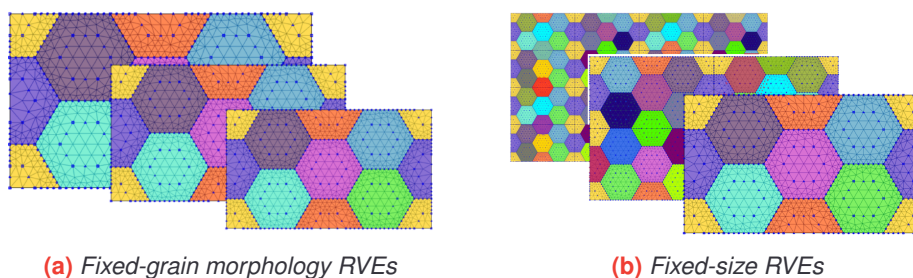


Figure 5.3: Different methods for scaling RVEs

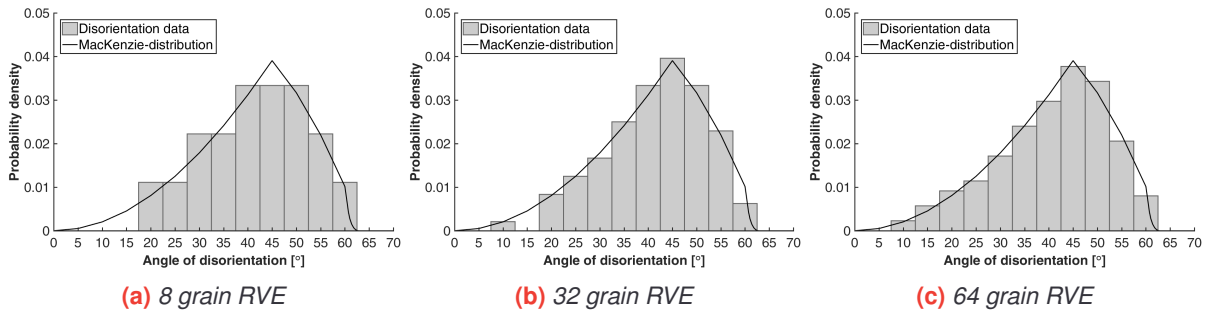


Figure 5.4: Best-obtained disorientation distributions for various numbers of hexagonal grains

In this work, RVEs with equally sized, hexagonal grains will be used to have direct control over the size of the grains. The incircle diameter of the hexagons is set equal to the desired grain size. In contrast to the work of Becker, fully periodic RVEs will be used. This avoids additional strengthening effects resulting from displacement constraints, which restrict the anisotropic deformation of crystals near the constrained edges. Two scaling methods are proposed as shown in Figure 5.3. For method 1, the grain number is kept fixed while changing the outer dimensions of the sample. For method 2, the outer dimensions of the sample are kept fixed while changing the grain number. The difference between the scaling method lies in the ratio between grain boundary area and RVE volume. For method 1, this ratio remains constant, whereas for method 2, it is varied. As several authors attribute the Hall-Petch effect to grain boundary effects [6, 13, 14], the second method is used to investigate the influence of the grain boundary area ratio.

Fixed-grain morphology RVEs

Simulations for this scaling method will be performed for 8.5, 17, 34, 88, 240 and 500 μm grains. For each sample, the grain number and morphology is kept constant. The grain size is altered by changing the size of the RVE. To make sure the numerical results will most closely resemble the response of a real polycrystalline material, it is important to obtain a good distribution of grain orientations over the model. For a computationally efficient model, the number of grains should be as low as possible. Due to geometrical restrictions posed by the periodicity of the RVE, the smallest possible RVEs consist out of 8, 16, 32 or 64 grains.

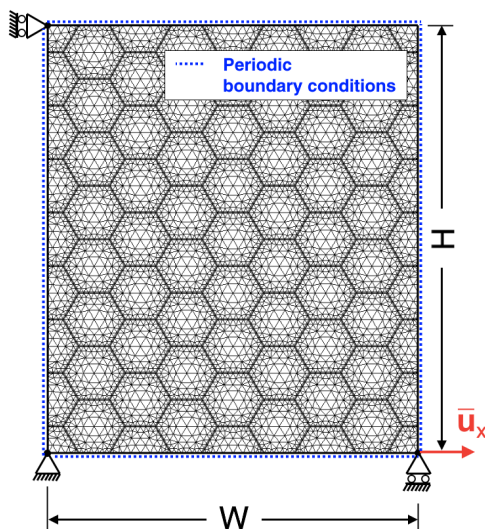


Figure 5.5: 64-grain FEM-model used for simulating the Hall-Petch effect

Following the approach in Appendix E, a number of trial RVEs with random assignment of grain orientations was generated for each grain number. The resulting distribution of disorientations between adjacent grains was compared to that of a random polycrystals, as specified by the MacKenzie-distribution [39]. It was found that for all considered grain numbers, an RVE with a reasonably random disorientation distribution can be obtained. The best-obtained distributions are shown in Figure 5.4. Presence of the low range of disorientation angles is however only observed in the 32 and 64-grain RVEs. For those angles, incompatibility between grains is low and less GNDs are expected to be generated at the corresponding grain boundaries. This results in less additional hardening. To avoid an overprediction of the hardening effect by not including low disorientation angles, the 64-grain RVE with the disorientation distribution in Figure 5.4c will be used for the simulations. Details about the assignment of grain orientations can be found in Appendix E.

E [MPa]	ν [-]	b [nm]	c [-]	$\rho_{SSD}^{0,(\alpha)}$ [mm ⁻²]	$\rho_{SSD}^{\infty,(\alpha)}$ [mm ⁻²]	γ^{∞} [-]	τ_0 [MPa]	$Q_0^{\alpha\beta} - Q_5^{\alpha\beta}$ [-]
68758.93	0.348214	0.286	0.3	$2 \cdot 10^4$	$2.2 \cdot 10^8$	0.23	0	0.1, 0.3, 0.16, 0.22, 0.38, 0.45

Table 5.1: Material parameters used in the Hall-Petch simulations

An overview of the model with applied boundary conditions is shown in Figure 5.5. Each individual grain is meshed with 132 plane strain quadratic triangular elements. The mesh is refined near the grain boundaries. Each simulation will be performed up to 4% equivalent strain in horizontal direction, for which $\bar{u}_x = 0.04 \cdot W$. The material parameters for pure aluminium are adapted from [12] and are shown in Table 5.1. The hardening parameters $\rho_{SSD}^{0,(\alpha)}$, $\rho_{SSD}^{\infty,(\alpha)}$ and γ^{∞} will be fitted to the results from Honeycombe for 500 μm grains [40, p. 238] and used in the simulations for the other grain sizes.

Fixed-size RVEs

For the second sizing method, the outer dimensions of the rectangular RVE are kept constant. The grain size is now specified by varying the number of grains. A 32-grain model with 34 μm grains is used as reference model. One 8-grain model with 68 μm grain size can be created with still a reasonably uniform disorientation distribution (Figure 5.4a) within the same rectangular area. Increasing the grain numbers to 128 and 512 creates periodically tiled models with grain sizes of 17 and 8.5 μm . In this way, a similar range of grains sizes compared to that in the fixed-morphology RVEs is covered. For the two smallest grain sizes, each grain is randomly assigned an orientation as generated using the method in Section E.1. The boundary conditions applied to the models for the second sizing method are identical to those in Figure 5.5.

5.2.3 Results

Results for fixed grain morphology

The stress-strain responses of the fixed-morphology RVEs are given in Figure 5.6a. The experimental data that was used to fit the material model is also included in this plot. It is found that the experimental results are represented very well by the 500 μm -grain model. As the grain size decreases, an increase in the stress level is observed. Also, the work hardening rate of the material at fixed strain levels is found to increase with decreasing grain size. With developing strain, this rate decreases and eventually saturates to a constant level.

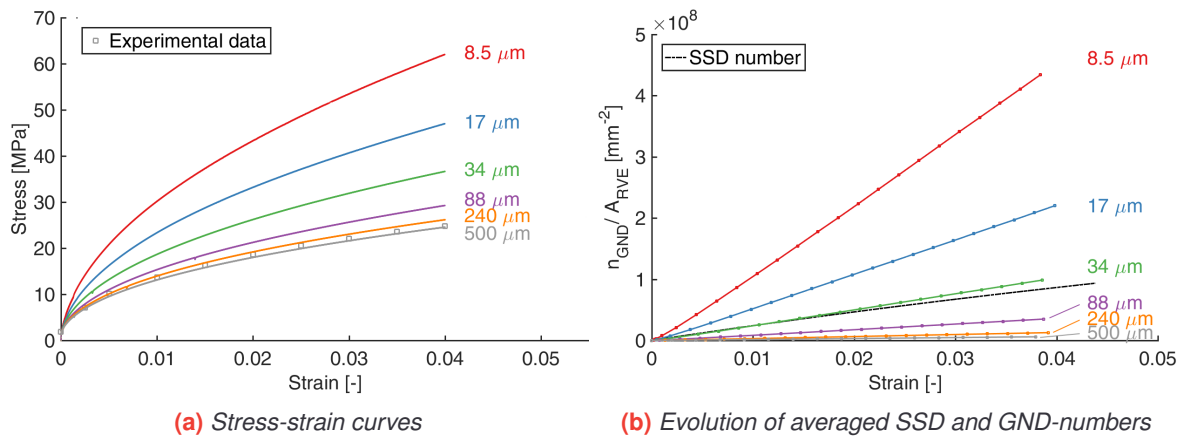


Figure 5.6: Results for tensile deformation of hexagonal-grained RVEs with fixed grain morphology

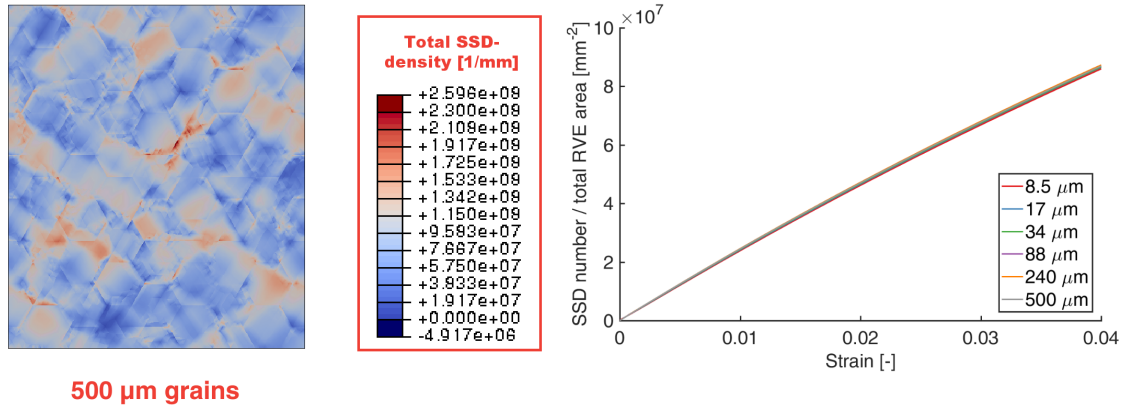


Figure 5.7: Comparison of the SSD evolution as function of strain for the different models (left) and SSD distribution in the 500 μm fixed-morphology model (left)

The total SSD-number normalised by the RVE area as function of strain is plotted in Figure 5.7 together with the SSD-density distribution at 4% strain in the 500 μm -grain model. Dislocation numbers are calculated using the approach in Appendix F. The effect of the different grain orientations can clearly be recognised from the difference in ρ_{SSD} between the different grains. The normalised number of GNDs generated is plotted as function of strain in Figure 5.6b.

When comparing the evolution of dislocation densities for the various grain sizes, it is found that no difference in the SSD-distribution is found between the different grain sizes. This is a direct result of scaling the RVE while keeping the grain morphology the same, as each model is subjected to the same deformation and thus obtains the same distribution of plastic slip. By the direct dependence of the SSD-number on the plastic slip, the SSD-distribution will remain unchanged.

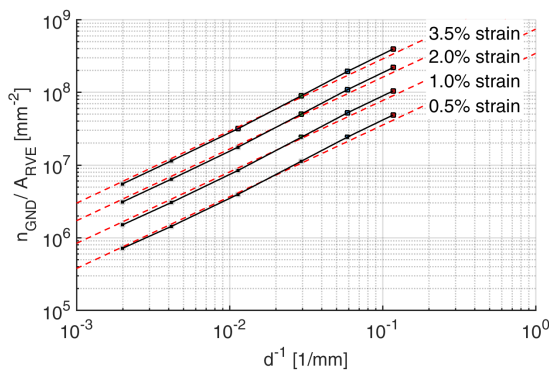


Figure 5.8: Total GND number at fixed strain level versus inverse grain size for the fixed-morphology models. Red lines indicate linear fit

With a decreasing grain size, a larger number of GNDs is present. For grains smaller than 34 μm , the total number of GNDs starts to significantly outweigh the SSD numbers and thus the hardening becomes dominated by the GND evolution. The GND generation rate also increased with grain size and is linear with respect to the average strain in the RVE, whereas the generation rate for SSDs drops with increasing strain due to the characteristics of (2.14). When plotting the normalised GND number against the inverse of the grain size in Figure 5.8, the GND number at fixed strain is found to be inversely proportional to the grain size. This result can be related to the length scale introduced by the gradient calculations and is a direct consequence of the used scaling method.

A comparison of the GND-density distribution between the models with 8.5 and 500 μm grains is shown in Figure 5.9. It is again clearly noticed that for the large grains, virtually no GNDs are present. It can also be seen that the formation of GNDs is concentrated around the grain boundaries. A similar result is found when comparing the Von Mises stresses between the two aforementioned models. A larger distribution of stresses is present for the smaller grain size and regions with high stress are concentrated around grain boundaries due to the enhanced hardening caused by the GND presence.

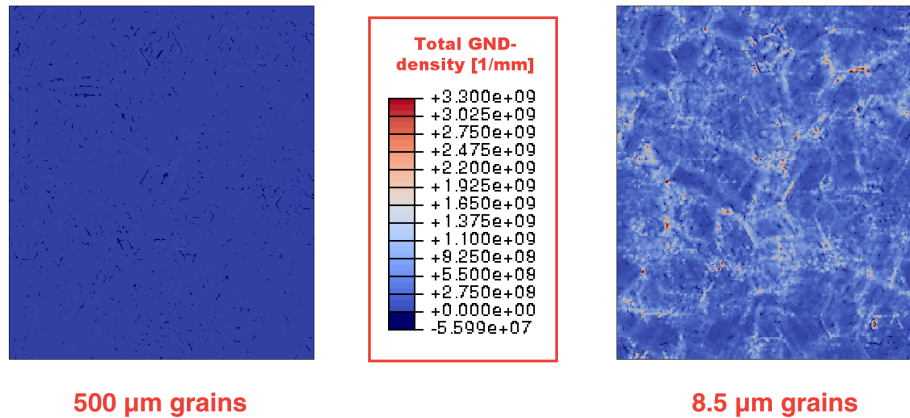


Figure 5.9: Comparison of GND-densities for the 8.5 and 500 μm fixed-morphology models.

Results for fixed RVE dimensions

The simulations with RVEs of identical outer dimensions show comparable results to those discussed above. An important observation is made from the evolution of SSDs with strain in Figure 5.11a. Despite the varying number of grains and thus changing orientation distributions, the curves are virtually identical to each other and comparable in magnitude and trend to those obtained from the fixed-morphology RVEs. This indicates that comparison between the different results of the second scaling method is possible, as well as a comparison between the results from both scaling methods. It validates that a sufficient number of grains and a sufficiently random orientation distribution is present in all models and the periodic boundary conditions are applied appropriately. This is the case if the response does not change upon adding a further amount of grains to the RVE [33], which is what is observed in the results and essentially what is done in the second scaling method.

The trends in the stress-strain curves (Figure 5.11b) and GND-evolution versus strain (Figure 5.11c) are similar to those found from the fixed-morphology simulations. A decreasing grain size gives rise to a larger number of GNDs and thus higher stress levels. The increase of the GND number is again found to be linear with strain and at fixed strain level is inversely proportional to the grain size (Figure 5.11d). A difference between the two scaling types is primarily found in the results for the 8.5 μm grains. For the fixed-size RVE, the total GND number and stress levels are lower than observed for the fixed-morphology RVE. The distribution of the GND-densities in the 8.5 and 68 μm models is compared in Figure 5.10. Also here it can be seen that GNDs concentrate near the grain boundaries and higher numbers are observed for smaller grains.

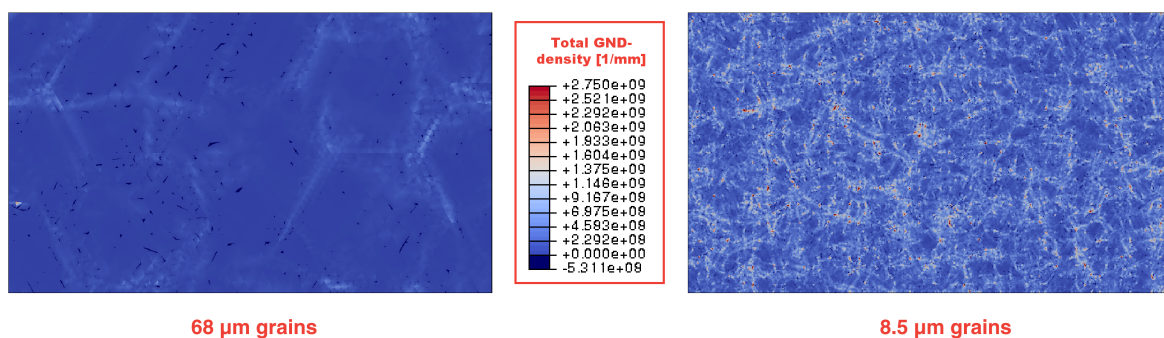


Figure 5.10: Comparison of GND-densities for the 8.5 and 68 μm fixed-dimension models.

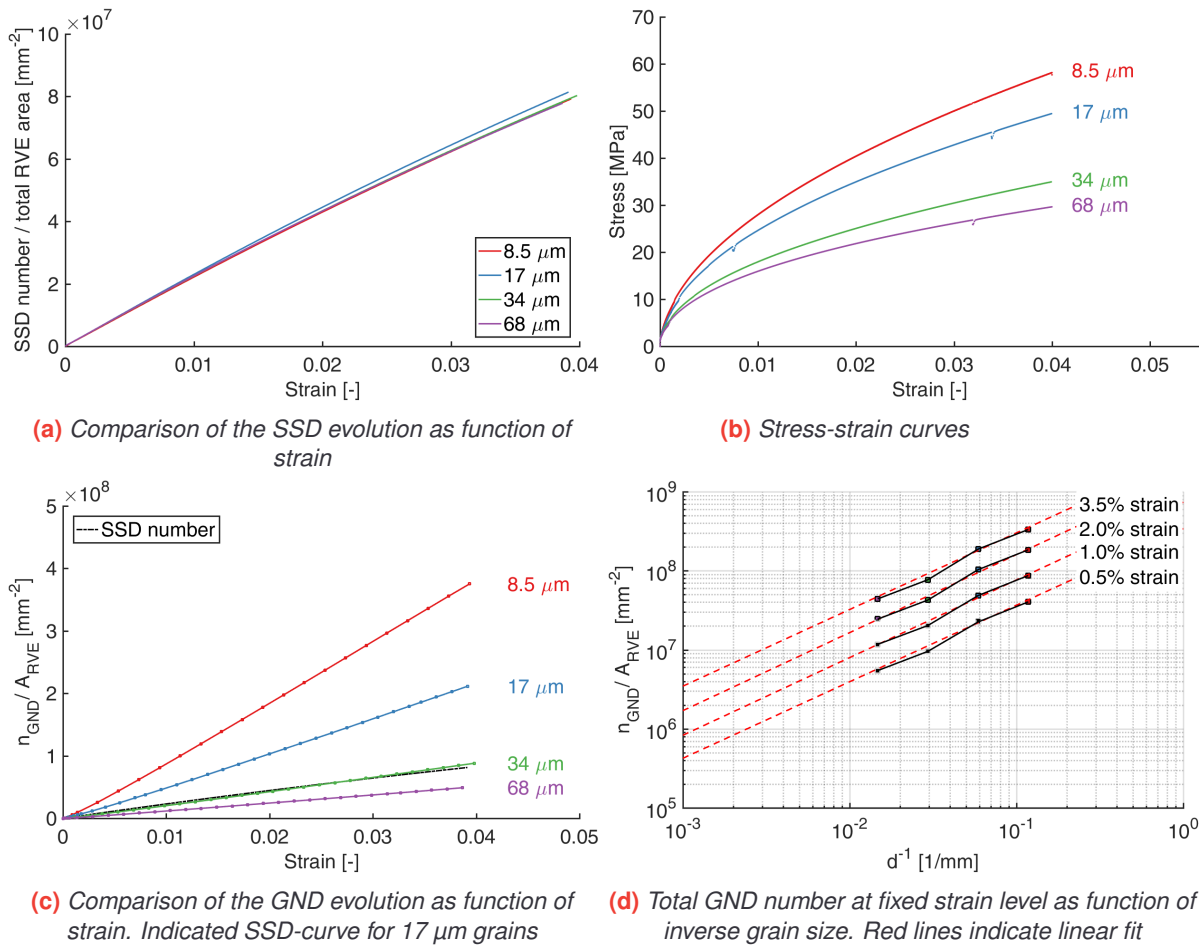


Figure 5.11: Results for tensile deformation of hexagonal-grained RVEs with fixed outer dimensions

5.2.4 Discussion of results

The Hall-Petch plots at 0.2% strain are shown for both scaling methods in Figure 5.12. Both are in well agreement with the classically obtained exponent of 0.5. For the fixed-morphology simulations, a somewhat larger exponent of 0.72 produces a better fit. This indicates a slight overprediction of the grain size effect on the flow stress. Literature findings obtain exponent values close to or exceeding 1 ([6, 12, 34]) and thus a significant overprediction of the size effect. Overall, the experimentally observed size-effect can thus be regarded to be captured very well using the approach in this work.

Differences between the current findings and ([6, 12]) can be attributed to effects of non-periodic models and thus restricted anisotropic behaviour. Also, the low grain number (12 grains were used) with non-random misorientation distribution used in these two publications is believed to have significant influence on the results. In the paper of Counts et. al. [34] an initial GND density is used, but no details are provided on the GND-evolution and thus the effect of this initial density on the final results cannot be traced. A fair comparison with these results is thus not possible. In its formulation, the implementation of GNDs in the model of Becker [12] is equal to that used in this work. It is therefore posed that including periodicity and a sufficiently random misorientation distribution is of great importance when using gradient-enhanced crystal plasticity models, due to the increasing effect of inhomogeneities on the macroscopic response of the RVE.

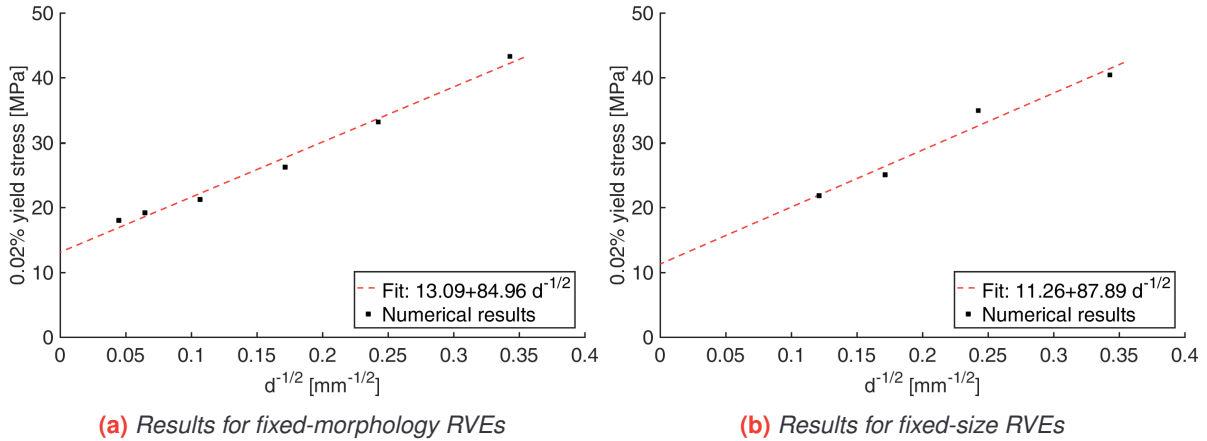


Figure 5.12: Hall-Petch plots at 0.2% strain

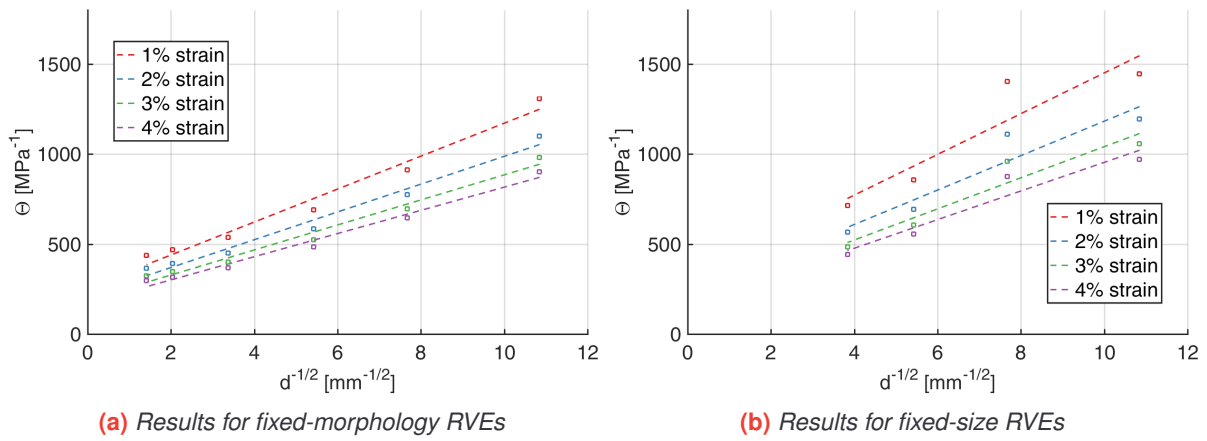


Figure 5.13: Hall-Petch plots for the work hardening rate at various strain levels

The concentration of GNDs primarily near grain boundaries as claimed by ([21, 22]) is in accordance with literature findings. The precise relation of this fact to the increase of GND numbers with decreasing grain size can be explained as follows. It was stated by Evers et. al. [6] that with decreasing grain size, inhomogeneities due to incompatibility at the grain boundaries increase. They claim that this effect too, but primarily the Burgers vector length that relates the slip gradients to GND densities, cause an increasing hardening effect near the grain boundaries. For the fixed-morphology simulations, the absolute incompatibility in terms of misorientation between two crystals remains unchanged. An increasing GND-number with decreasing grain size is still observed though. It is thus indeed the spatial distance in which a difference in plastic slip levels is to be accounted for, that is the driving mechanism for grain size hardening.

Experimental results for 99.99% pure aluminium showed that initially, the work hardening rate $\Theta = \frac{d\bar{\sigma}}{d\bar{\epsilon}}$ obeys a Hall-Petch-like dependency too. With prolonged strain, the influence of grain size becomes less visible, i.e. the Hall-Petch slope decreases. Already at strain levels of 5%, no grains size dependency in the work hardening slope can be observed anymore [41]. Figure 5.13 shows the work-hardening rates versus inverse square root of the grain size for both scaling methods. Contradictory to the experimental observations, the work hardening rates do not saturate to the same constant level.

In (2.11), the critically resolved shear stress of a slip system is described as function of the square root of its total dislocation density. A similar dependency is observed macroscopically for the stress $\bar{\sigma}$, as shown in Figure 5.14a. Due to the evolution behaviour of the GNDs, the total dislocation number increases

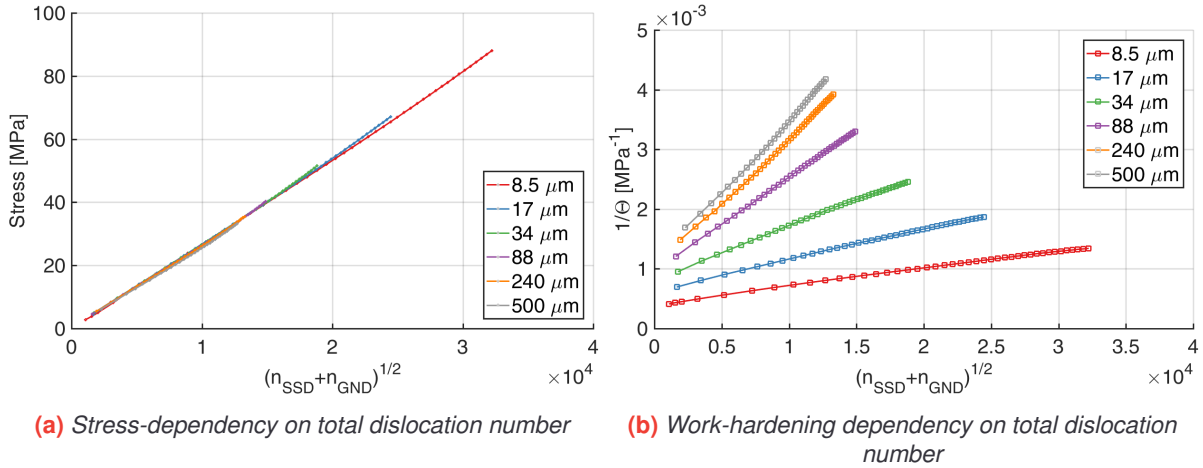


Figure 5.14: Results found to scale linearly with the square root of the total dislocation number

almost linear with macroscopic strain $\bar{\epsilon}$, especially for the smaller grain sizes. As a consequence, the inverse of the work hardening rate Θ is found to be directly proportional to the square root of the total dislocation density ρ_{tot} :

$$\left. \begin{array}{l} \rho_{tot} = a\bar{\epsilon} + b \\ \bar{\sigma} \propto \sqrt{n_{tot}} \end{array} \right\} \rightarrow \bar{\sigma} \propto \sqrt{a\bar{\epsilon} + b} \rightarrow \Theta = \frac{d\bar{\sigma}}{d\bar{\epsilon}} \propto \frac{1}{\sqrt{a\bar{\epsilon} + b}} \rightarrow \frac{1}{\Theta} \propto \sqrt{n_{tot}} \quad (5.3)$$

as is visualised in Figure 5.14b. This implies that a saturation of the work hardening rates to an identical, constant, level together with a constant GND-generation rate is not possible.

5.2.5 Conclusions

The grain-size dependency of the flow stress was studied using a gradient-enhanced crystal plasticity model. It was shown that the incorporation of slip gradients in the slip system hardening function through the GND-density renders a size-dependent work-hardening behaviour. The initial yield stress remains unchanged though. The results for both the fixed-morphology as well as the fixed-size RVEs agrees well with the classical Hall-Petch exponent of 0.5. However, the larger Hall-Petch exponent of 0.72 in the fixed-morphology results indicates that here the effect of grain size may be overpredicted to some extent. Compared to literature results, the Hall-Petch fit obtained with the current models is significantly better. Application of periodic boundary conditions and using RVEs with a sufficient number of grains and random disorientation distribution was found to be crucial in the application of the crystal plasticity model.

The driving mechanism for the size-dependency of a gradient enhanced crystal plasticity model was identified as the spatial distance in which differences in plastic slip levels have to be accounted for. For prolonged deformation, no size-independent saturated work hardening was observed. This is derived to be caused by the ever-increasing GND-number. For higher strain levels, it therefore seems that the work-hardening behaviour is overpredicted.

Research Question 1.1 - Answer

Size-dependent work-hardening behaviour is obtained by including GNDs as function of slip gradients. The inclusion of GNDs does not affect the initial yield stress. The fit to the Hall-Petch relation is good for small strains, but deviations with experimental results increase with increasing strain.

5.3 The Bauschinger effect

Upon loading a pre-strained crystalline material in reverse direction, the yield stress in this direction is lower than the original yield stress in the pre-strain direction. This effect is called the Bauschinger effect. The extent to which this effect is observed, depends on the load history of the material, the strain rate and texture of the microstructure [42]. Numerous attempts have been made to model the Bauschinger effect in both single and polycrystals, but the generally accepted underlying mechanism can in essence be derived to be based upon formation of back stresses [43]. These back stresses result from dislocation pile-ups around obstacles. Piled-up dislocations develop a stress opposing the loading direction, hindering the motion of dislocations with the same sign. This causes the material to work-harden. Upon reversing the load direction, piled-up dislocations are repelled by this stress in the direction of the reversed load. The back stress thus helps moving dislocation in the new loading direction and therefore lowers the yield stress in that direction [42].

The concept of back stress has been applied to various rate-dependent crystal plasticity models to determine the cyclic loading behaviour of (poly-)crystalline materials (a.o. [17, 44, 45]). Herein, the resolved shear stress acting on a slip system is modified to include the back stress $\tau_b^{(\alpha)}$ as $\tau'^{(\alpha)} = \tau^{(\alpha)} - \tau_b^{(\alpha)}$. With the exception of [44], GNDs as function of strain gradients are not included. In this work, Bayley et. al. use a gradient-enhanced crystal plasticity formulation with a back stress formulation in terms of GND gradients [44]. From their application of the model to constrained simple-shear of a semi-infinite block, they observe the back stress evolution to be the sole cause for the observed Bauschinger effect. The GND-induced slip system hardening did not affect the Bauschinger effect. One could raise the assumption that the Bauschinger effect could only be modelled by including a back stress term in the constitutive relations.

It was however shown by various authors that this is not required for polycrystalline materials. For instance, Tóth et. al. use a conventional rate-dependent crystal plasticity formulation to predict cyclic plasticity phenomena in copper [45]. The Bauschinger effect was observed, caused by plastic anisotropy of the grains. A similar observation was made by Li et. al. [17]. They compared cyclic results for AL7075 from a three-dimensional texture based RVE with and without the contribution of back stress. Both the back stress as well as residual stresses were shown to contribute to the macroscopic Bauschinger effect. The presence of such residual stresses as probable cause of the Bauschinger effect has been more elaborately studied during the last years. As a fact, experimental studies on mainly austenitic stainless steel have identified residual lattice stresses as primary source of the Bauschinger effect in these materials [4, 8, 46].

The observations from literature show that including a back stress measure is not required to capture the Bauschinger effect. The comparison of numerical results with experimental data in the works cited above, however shows that a conventional crystal plasticity model could not fully predict it. If the hypothesis is posed that the Bauschinger effect in polycrystalline materials is caused by residual stresses, increasing the extent to which these are predicted by a crystal plasticity model may resolve this shortcoming.

Unlike what is found in the work of Bayley et. al. [44] for single crystals, the influence of GNDs on slip system hardening may affect the Bauschinger effect in polycrystalline materials. As GNDs form primarily near grain boundaries [21, 22], they will enhance the non-uniformity of the stress distribution within the material. This was observed from the results in Section 5.2.3 too. It will therefore be investigated whether the inclusion of GND-induced hardening in the constitutive framework can solve the shortcoming of the conventional model to predict the residual stress-state within the material. Therefore, the following research questions are formulated:

Research Question 1.2

1. Can the Bauschinger effect observed from crystal plasticity simulations be explained by the presence of residual stresses?
2. Can the representation of the Bauschinger effect as a result of residual stresses be improved by inclusion of GNDs in the hardening model?

5.3.1 Setting up the FEM-models

Two materials will be used for simulating the Bauschinger effect using (gradient enhanced) crystal plasticity in the remainder of this section, being a 6000-series aluminium alloy (FCC-lattice) and a dual-phase steel (BCC-lattice). For both materials, the 32-hexagonal-grain RVE with random orientation distribution from Figure E.4b is used with boundary conditions as in Figure 5.5. Consistent with the Hall-Petch models, grains are meshed with 132 plane strain quadratic triangular elements each.

The aluminium model will be subjected to cyclic tests and compared to cyclic stress-strain data retrieved from literature [47], to allow for the assessment of the extent to which the model can represent the experimentally observed Bauschinger effect. The material is strained uniaxially up to levels of ± 0.5 , 1.0, 1.5 and 2.0% engineering strain in horizontal direction. To determine the effect of the presence of GNDs, simulations are performed using both the gradient enhanced crystal plasticity formulation as well as using the stress-update algorithm in which the GND-induced hardening terms are omitted.

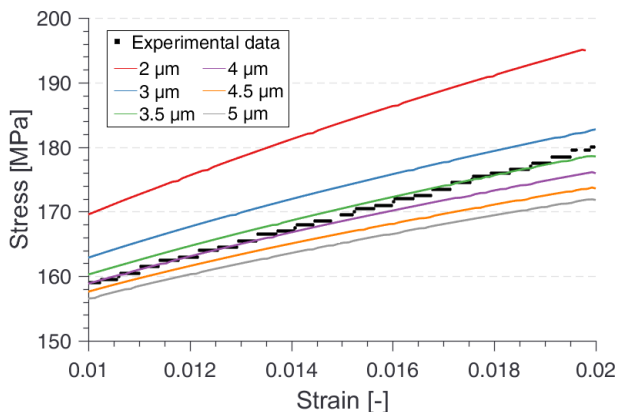


Figure 5.15: Fit to experimental data for different grain sizes

Material parameters are fitted to the experimental loading curve of 2.0% engineering strain. The grain size was determined first using assumptions that were derived from the Hall-Petch results. For small grain sizes, GNDs outnumber SSDs already at small strain levels. The (saturated) work hardening rate is therefore mainly controlled by the GND generation rate and thus the grain size. Following this observation, a uniaxial tensile strain of 2% was applied to a range of RVEs with grain sizes of 2, 3, 3.5, 4, 4.5 and 5 μm . The SSDs evolution parameters were taken equal to those in the Hall-Petch simulations. The saturated slopes of the stress-strain curves were compared to that of the experimental stress-strain curve in Figure 5.15. The grain size was found to be 3 μm .

With this given, the evolution parameters of the SSD-density could be fitted for both the gradient-enhanced as well as the SSD-only simulations. The entries of the interaction matrix for latent hardening are chosen identical to those in Section 5.2.2. The final parameter values are given in Table 5.2.

A load-reversal test is applied to the dual-phase (DP) steel model to investigate the effect of the harder second phase present in this type of material on the Bauschinger effect. Prestrain levels of 3% and 4% engineering strain in horizontal direction are applied before unloading the material to zero strain. Martensite material data is assigned to grains 3, 5, 17 and 32 to mimic a martensite content of 12%. The components of the interaction matrix are taken from [16]. The SSD-evolution parameters for both the ferrite and martensite grains are fitted simultaneously to match experimental tensile data of DP600. The average grain size is set to 20 μm in accordance with the experimental results. The final material parameters are shown in Table 5.2.

	E [MPa]	ν [-]	b [nm]	c [-]	$\rho_{SSD}^{0,(\alpha)}$ [mm ⁻²]	$\rho_{SSD}^{\infty,(\alpha)}$ [mm ⁻²]	γ^{∞} [-]	τ_0 [MPa]	$Q_0^{\alpha\beta} - Q_5^{\alpha\beta}$ [-]
Alu (SSD+GND)	61500	0.3	0.286	0.3	$2 \cdot 10^4$	$1 \cdot 10^8$	0.1	51	0.1, 0.3, 0.16, 0.22, 0.38, 0.45
Alu (SSD-only)	61500	0.3	0.286	0.3	$2 \cdot 10^4$	$3 \cdot 10^9$	0.5	51	0.1, 0.3, 0.16, 0.22, 0.38, 0.45
DP (ferrite)	210000	0.3	0.286	0.4	$2.3 \cdot 10^7$	$8 \cdot 10^8$	0.4	7	1, 1.4, 1.4, 1.4, 1.4, 1.4
DP (martensite)	210000	0.3	0.286	0.3	$1 \cdot 10^8$	$3 \cdot 10^9$	1	7	1, 1.4, 1.4, 1.4, 1.4, 1.4

Table 5.2: Material parameters used in the Bauschinger effect simulations

The influence of production-induced dislocations is tested in additional simulations by mimicking a cold-rolling step. Prior to the abovementioned simulations, the RVE is compressed in vertical direction and elongated in horizontal direction. This deformed state is then used as initial configuration for the cyclic and reload tests and is subjected to identical strain levels as discussed above. For the dual-phase steel RVE, a 1%-compression - 1%-tension pre-deformation is applied. For the aluminium model, a 10% - 10% deformation is used to exaggerate its resulting effects.

5.3.2 Results

The stress-strain curves for unrolled aluminium with and without GNDs are shown together with the experimental data in Figure 5.16a. In initial tension, both curves agree well with the experimental data and the size of the elastoplastic-transition is captured. Upon compressive reloading, the reyield stress is underpredicted compared to the experiments, where the elastoplastic transition starts earlier. The size of the transition region is also larger than obtained from simulations. During compressive loading, the increase in work hardening rate that is observed in the experimental data is overestimated by the crystal plasticity model. This causes the simulated material response to be flatter than its experimental counterpart. This effect is most pronounced for the SSD-only simulations. After tensile reloading, again the size of the elastoplastic transition region is smaller than experimentally observed and macroscopic yield occurs later. In the second tensile load step, the slope of the stress-strain curve resembles that of the experiments very well for the simulations with GND-presence. For the SSD-only results, the response appears still too flat. An increase in transition region size upon load reversal is observed for both simulation types. Its size also increases with plastic deformation.

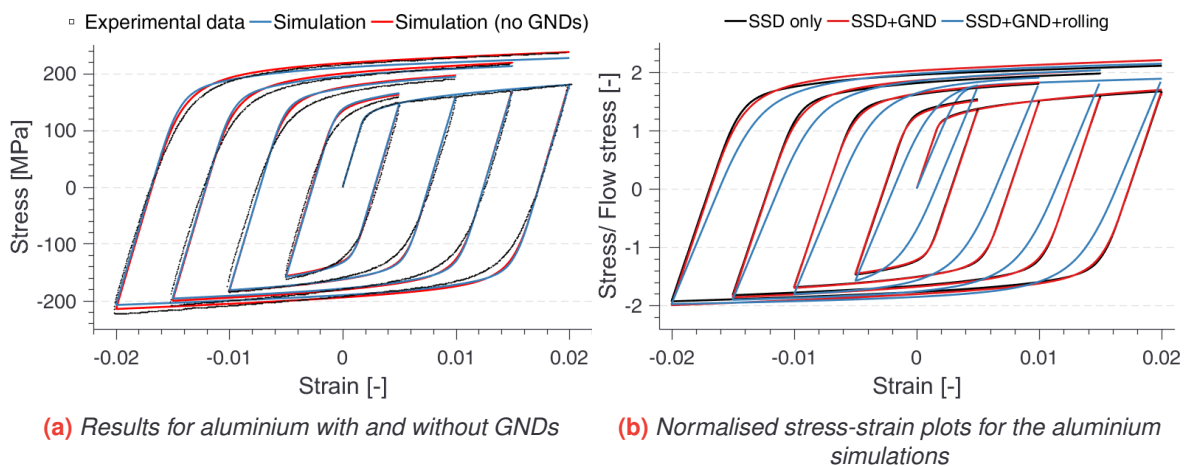


Figure 5.16: Stress-strain curves from the aluminium cycle tests

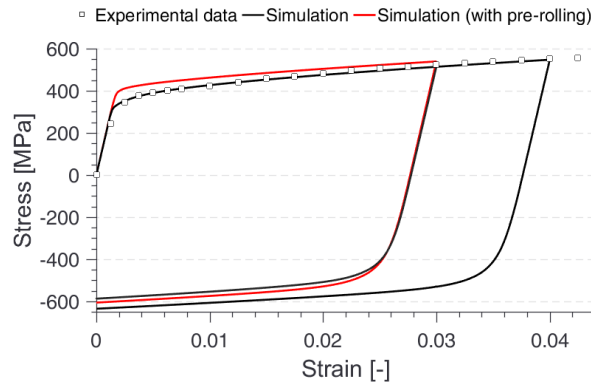


Figure 5.17: Stress-strain curves for dual-phase steel

Figure 5.16b shows the cyclic stress-strain curves for the simulations without GND-presence, with GND-presence and with the applied 10%-10% rolling deformation, normalised with respect to the initial flow stress. It is observed that initially, the stress for the rolled specimen is higher than that of the non-rolled RVEs. This is a direct consequence of the additional hardening resulting from the plastic deformation in the rolling step. The macroscopic elastic modulus is found to be increased. This clearly shows the influence of the plastic anisotropy of the individual grains, which respond differently to the uniaxial tension after the plastic deformation applied in the rolling step. Overall, the sizes of the elastoplastic transition regions increase. Yielding upon load reversal occurs earlier, indicating that the Bauschinger effect is enhanced by the pre-rolling.

The load reversal curves for both the dual-phase steel RVEs with and without pre-rolling are shown in Figure 5.17. The experimental tensile data is also shown to indicate the fit of the material model. In these results too, the applied pre-rolling raises the flow stress levels due to additional hardening. The size of the elastoplastic transition region is again found to be increased with increasing prestrain and rolling deformation.

The distribution of integration point stresses in the loading direction (σ_{11}) at 2% tensile strain is shown in Figure 5.18 for the different simulations. The stress levels are normalised with respect to the macroscopic prestress level at this point. All plots show a distribution that is centred around the macroscopic stress level. Comparing the results for aluminium, it is shown that including GNDs in the crystal plasticity model results in a wider stress distribution. The same holds for applying an initial deformation step. When comparing the distribution from the aluminium simulation with GND-presence to that of the dual-phase steel, it is seen that the stress distribution is wider for the latter material. The presence of a hard second phase thus also results in a widening of the distribution. The significant difference found between the aluminium results with GNDs and with and without pre-rolling is not observed in the DP steel. It must however be noted that the pre-rolling deformation applied to the DP steel is significantly lower than that applied to the aluminium RVE.

Figure 5.19 shows the dependency of the stress distribution on the prestrain level for the aluminium RVE simulated with the gradient enhanced crystal plasticity model. It is observed that with increasing plastic deformation, the width of the distribution increases. This is in line with the findings from the comparison between the unrolled and rolled RVEs, where also an increasing distribution with was found upon applying an initial plastic deformation. This is a direct result of an increased amount of work hardening.

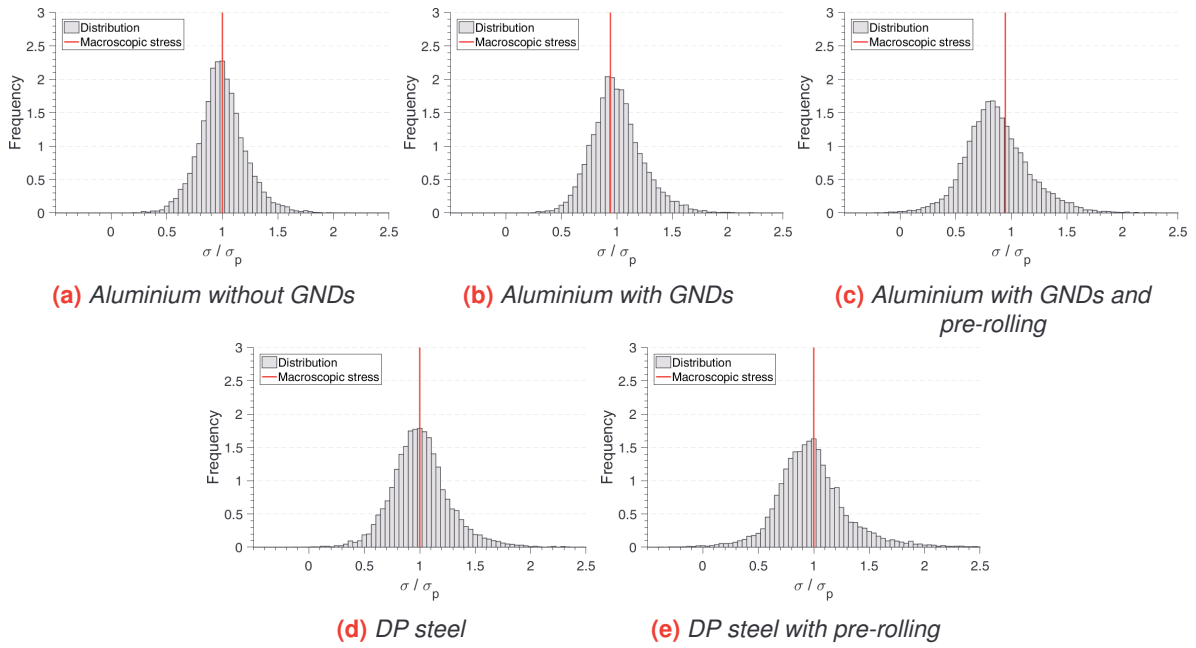


Figure 5.18: Stress distributions after tensile loading up to 2% strain for different RVEs.

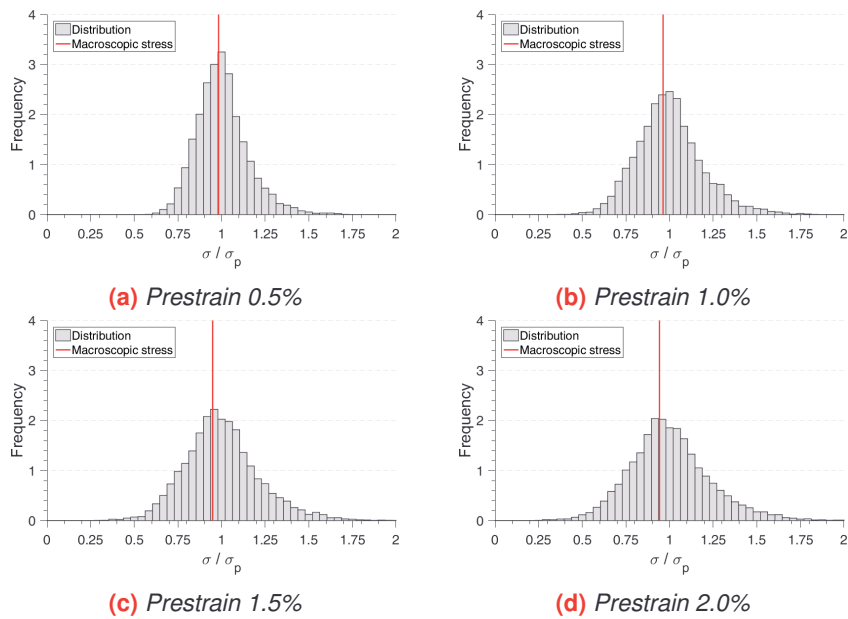


Figure 5.19: Stress distributions as function of prestrain level for aluminium with GND presence

Aluminium w/o. GNDs			Aluminium w. GNDs			Aluminium w. GNDs + rolling		
Prestrain	Cycle 1	Cycle 2	Prestrain	Cycle 1	Cycle 2	Prestrain	Cycle 1	Cycle 2
0.5%	0.20	0.24	0.5%	0.20	0.25	0.5%	0.51	0.41
1.0%	0.28	0.34	1.0%	0.29	0.37	1.0%	0.53	0.51
1.5%	0.32	0.39	1.5%	0.34	0.43	1.5%	0.54	0.54
2.0%	0.35	0.43	2.0%	0.38	0.47	2.0%	0.55	0.56

Dual-phase steel		Dual-phase steel w. rolling	
Prestrain	Cycle 1	Prestrain	Cycle 1
3.0%	0.31	3.0%	0.33
4.0%	0.34		

Table 5.3: Bauschinger stress parameters for the different simulations

5.3.3 Discussion of results

The simulations for aluminium qualitatively show the same results as experimentally observed in terms of elastoplastic transitions. Considering the availability of the material data underlying the experimental stress-strain curves, the fit to the experiments can be regarded reasonable. It is however not good enough for a direct comparison. No further comparison with experiments will be therefore be made, as validity of such conclusions may be questionable. Based on the observed effect of a pre-rolling step on the final response, the fit may be improved if more detailed information on the deformation history of the material used for the experiments is given and included in the simulations. This is in line with the findings in [48], where the pre-straining history was found to influence the difference in tension and compression response. A change towards a model with non-uniform grain size distribution will affect the elastoplastic transition region, as a wider grain size distribution leads to a larger transition region size [49]. This can also improve the fit with the experimental results.

Table 5.3 provides the Bauschinger stress-parameters for the different simulations and prestrain levels. The Bauschinger stress-parameter is a non-dimensional constant to indicate the magnitude of the Bauschinger effect and is defined as

$$\beta_{\sigma} = \frac{|\sigma_p| - |\sigma_{r,0.2\%}|}{|\sigma_p|} \quad (5.4)$$

where σ_p is the stress level just before load reversal and $\sigma_{r,0.2\%}$ is the 0.2% reyield stress after load reversal. In all simulations, even those without GND presence, the Bauschinger effect is observed.

Based on the stress distributions in Figure 5.18 and the Bauschinger parameters in Table 5.3, there exists a correlation between the distribution width and the magnitude of the Bauschinger effect. The wider the distribution becomes, the more pronounced the Bauschinger effect is encountered. This can be explained by considering Figure 5.20, which shows the evolution of the distribution throughout the deformation cycle for DP-steel. The macroscopic stress level and negated initial yield stress are indicated as well. This figure is representative for the other simulation results too.

Upon compressive reloading, the total distribution is shifted in negative direction. Parts of the RVE become loaded in compression while the remaining material points are still in tension. Once the compressed points exceed their local flow stress, microscopic yielding occurs. Their flow is however restricted by surrounding elastic regions. It is also known that after yielding, the stress decrease with increasing compression lowers due to a reduction of the instantaneous modulus. Plastically deforming points within an elastic matrix would thus be characterised by a changing shape of the distribution: bins at the left side (characterising the plastified points, hindered in flow by the elastic points) will not move in negative direction whereas those to the right side (characterising the elastic points) will. Subsequently, the height of the distribution increases.

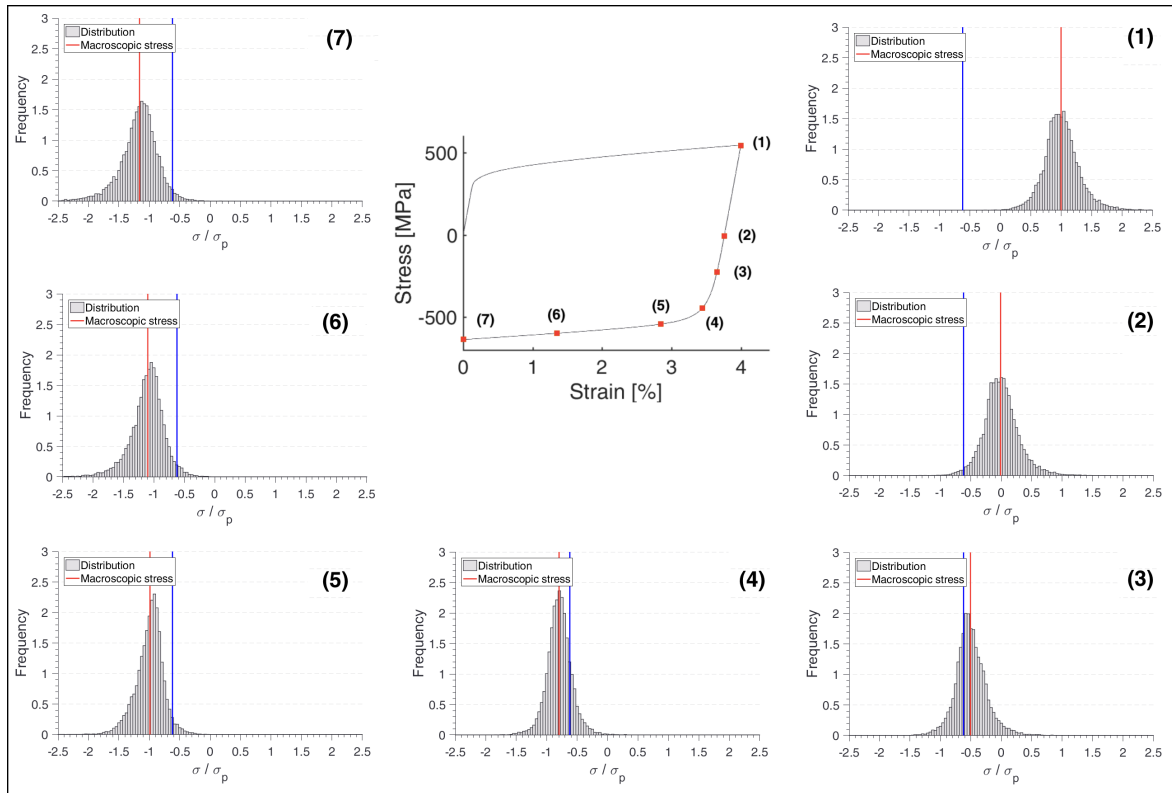


Figure 5.20: Evolution of stress distributions with strain in DP steel. *Blue line indicates negated initial yield stress*

Once a sufficient number of points has been plastified, macroscopic plastic flow can occur. The left bins of the stress distribution can then move in negative direction. Parts of the material with the highest stresses may not have yielded in compression yet. If surrounding plastic points allow flow of material around these elastic regions, the stress distribution shape will change opposite to the behaviour discussed above. Now, the rightmost bins of the distribution will be unable to move further left, whereas the left bins will move and the distribution height decreases.

Both abovementioned phenomena are observed in the elastoplastic transition and plastic region of Figure 5.20, respectively. A transition between plastic points within an elastic matrix towards elastic points within a plastic matrix thus takes place, initialised by the points initially loaded in compression most. The increase in distribution height, indicating plastic deformation has occurred, is observed before the macroscopic stress reaches the negated initial yield stress. The observed Bauschinger effect is accordingly found to be caused by the presence of a distribution of stresses in loading direction.

It will now be investigated what microstructural behaviour can explain the evolution of the stress distributions. As the grains within the RVE are plastically anisotropic, the difference in grain orientations within the material is most likely to underlie this evolution. Considering the initial tensile load step, two types of grains can be distinguished. Plastically soft grains yield earlier in tension, showing higher levels of plastic slip. Plastically hard grains yield later and show low levels of plastic slip. This can be shown in Figure 5.21, where the total plastic slip distribution after tensile preloading to 4% strain is plotted for the ferrite grains. Similar to Figure 5.20, stress distribution at various points of the unloading curve are shown for two adjacent grains. Results for the grain with a low amount of slip are shown at the left side of the figure, those for a grain with a high amount of slip on the right side. The grain with the lowest amount of plastic slip is indicated in magenta. The point on the stress-strain curve where this grain is first fully in compression is marked with an asterisk (*).

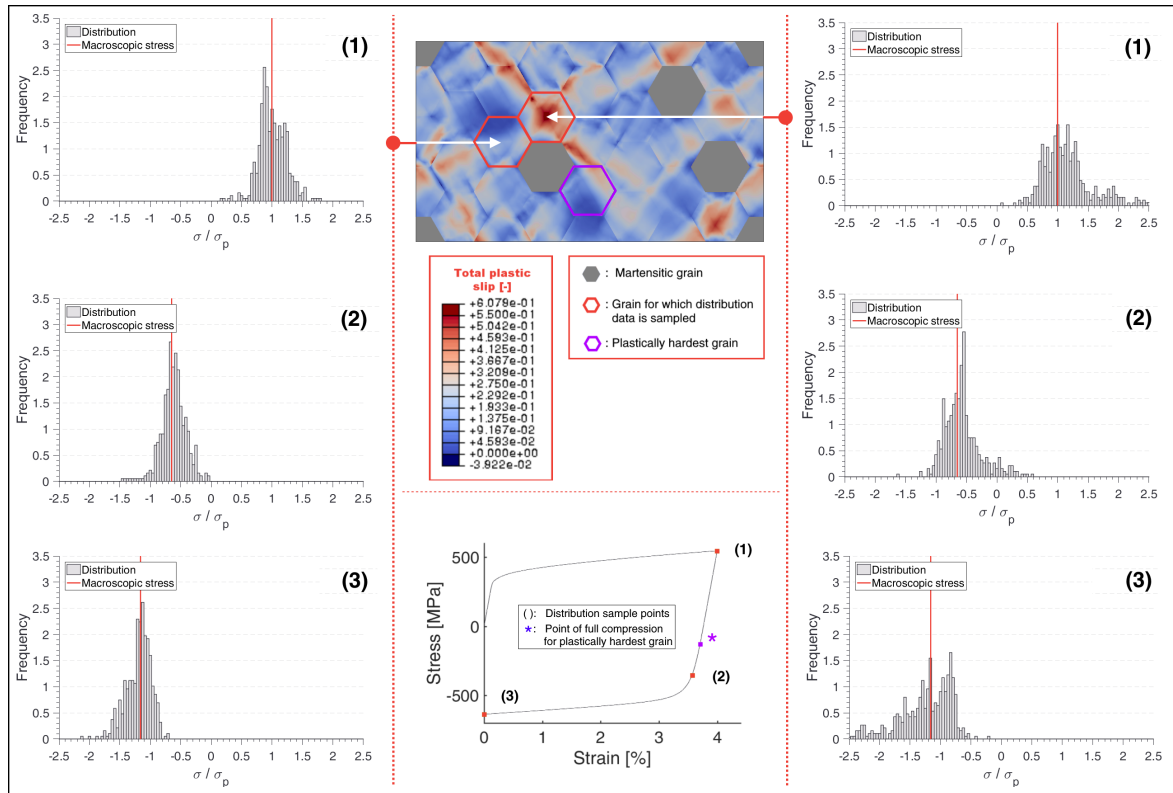


Figure 5.21: Evolution of stress distributions in plastically hard and soft grains with strain

At the prestrain level (point 1), stresses in the plastically soft grain are higher due to increased hardening. As a result of the differences in slip between grain boundary and core, its stress distribution is also wider. At the compressive 0.2% re-yield stress (point 2), the plastically harder grain is fully in compression, whereas the plastically softest one is still partly in tension. Similar findings were also reported in [17, 42]. The hardest grain has reached this state of full-compression considerably earlier. The shapes of the distributions at grain level evolve with strain similarly to those of the total RVE as discussed above. It is seen in Figure 5.21 that a significant difference in plastic slip between grains can exist. Therefore, macroscopic plastic deformation may be a result of plasticity within single grains only. Together with the observation that plastically hard grains reach a compressive state before soft ones upon reloading, it is found that the onset of macroscopic yield in compression is determined by yield in the plastically hardest grains. The observed Bauschinger effect is thus a direct result of differences in grain yield stresses. This is in agreement with the observations made in [4, 8].

Differences in grain yield stresses can be caused by plastic anisotropy and thus orientation mismatches between grains, but also directly by differences in material parameters in multi-phase materials. These differences in yield stress will increase by plastic pre-deformation due to work-hardening. This explains why the Bauschinger effect becomes larger with increasing prestrain or by applying the pre-rolling deformation. Analogously, the presence of GNDs enhances the Bauschinger effect. It was found in Section 5.2.3 already that GNDs were found to form primarily around grain boundaries. This results in wider stress distributions within grains. Thus, besides increasing differences in grain yield stresses as a direct result of GND-induced hardening, GNDs also magnify the intergranular Bauschinger effect.

5.3.4 Conclusions and recommendations

The Bauschinger effect observed from the simulations is found to be caused by the presence of a distribution of stresses in the loading direction, which causes parts of the material to yield earlier upon load reversal than would have been expected from the macroscopic stress level. These distributions are a direct result of differences in the response of individual grains to the macroscopic deformation. Plastic anisotropy and presence of a second-phase within the material are the underlying cause for these differences. They are widened by plastic deformation due to work hardening and GND-presence due to work hardening and magnification of the intergranular Bauschinger effect. This leads to a more pronounced macroscopic Bauschinger effect. Additional tests are required to further validate this conclusions with experimental results. Detailed information on the pre-deformation during the material manufacturing and grain-size distribution is to be included in the simulations in order to do so.

Research Question 1.2 - Answer

1. The presence of a Bauschinger effect in the crystal plasticity results can be explained by residual stresses in the material.
2. Considering contributions of GNDs in the slip system hardening equations increases differences in grain yield stresses and thus enhances the Bauschinger effect at the RVE level. It also widens the stress distributions within grains, enhances the Bauschinger effect within grains.

5.4 The anelasticity effect

In his work, Brown [50] described the typical behaviour of a polycrystalline material in a microstrain experiment. If a material is loaded up to a point below its elastic limit and then unloaded, the stress-strain curve is linear and cycles over the same straight line. If the elastic limit is exceeded by a small extent, the unloading curve forms a closed loop. This indicates that, in contradiction to what is commonly believed, the unloading curve of the material is not linear. A small amount of hysteresis is observed. The higher the preload stress, the bigger the width of the area contained within the loop becomes. This nonlinear unloading behaviour is referred to as anelasticity. After exceeding a certain preload stress, the loop fails to close. This stress level is termed the anelastic limit and defines the onset of a remaining (micro-) plastic deformation. If cycled below the anelastic limit, the hysteresis behaviour is completely reversible.

Anelastic effects are also observed after plastic deformation in various metals [51]. Upon unloading, a clear and nonlinear deviation from the initial elastic modulus is observed. Hysteresis loops are formed if the material is reloaded again. Similar to the microstrain behaviour discussed above, the nonlinear effects increase with the amount of plastic deformation. Over the past decades, various physically based explanations have been proposed to model the anelastic behaviour as summarised in [50].

Hill [52] described a possible cause for nonlinear unloading and hysteresis behaviour already in 1950. According to his reasoning, nonlinear unloading is caused by different orientations of grains within a material. This causes residual stresses which may cause a small amount of plasticity already before completely removing the external load on the material, producing an additional strain component. In his discussion, the initial parts of the unloading and reloading curves are however considered fully elastic. It may however be reasoned that this does not have to be the case in general, as for particular residual stress distributions some grains may already yield in compression at the very moment the load is reversed. An observation that is in line with the presence of residual stresses was made by Hama et al. [51]. They found from a crystal plasticity simulation that nonlinear unloading behaviour could be caused by differences in critical resolved shear stresses on various slip systems. As these stresses are governed by hardening and thus the amount of plastic deformation, different grain orientations give rise to dissimilarities here.

Anelastic effects were also attributed to the bowing-out of dislocation segments [53–55]. This mechanism causes limited and reversible dislocation motion. It appears in conjunction with the atomic bond stretching responsible for the elastic Hookean response. Under an applied shear stress τ , an initially straight dislocation segment is bent into a circular arch. The final curvature is reached when the line tension in the dislocation segment due to stretching equilibrates the shear stress. The resulting slip, proportional to the area A spanned by the arch, is the cause for the anelastic strain. Its magnitude can be derived to be a function of the total dislocation density ρ and average dislocation segment length l [53]:

$$\epsilon_{an} = \frac{\rho}{c} b A \quad (5.5)$$

in which c is the Taylor factor. The anelastic strain is thus a function of the dislocation structure, determined by ρ and l . With increasing plastic deformation, and thus increasing ρ and decreasing l , anelasticity effects become more visible. Below the critical shear stress, which equals the stress to produce the minimum arch radius $l/2$, the bow out mechanism should be fully reversible.

In cyclic loading below the flow stress, hysteresis behaviour and microplasticity are however observed [50, 54]. This contradicts the reversibility assumption. The authors in [54] explain small irreversibilities by the presence of obstacles to dislocation motion. These obstacles exert back stresses on the dislocation segment. As a result, the stress levels for dislocations to pass the obstacles in forward and reverse loading differ. As long as no obstacles are passed in forward loading, the mechanism remains reversible. The same is true if some obstacles will be passed in both forward and reverse loading. If not all obstacles are passed in reversed loading, some permanent deformation remains and microplasticity occurs.

Another explanation for nonlinear unloading that is related to back stresses and obstacles are dislocation pile-up and release mechanisms [9, 56]. Such mechanisms are in line with what was discussed in Section 5.3 in conjunction with the Bauschinger effect. Upon loading, repellent forces hinder the forward movement of dislocations, whereas the backward movement is aided by these forces. This would lead to the additional strain component observed as anelasticity.

In the current crystal plasticity model, no back stress formulation is present at the slip system level. A direct incorporation of dislocation pile-up and release mechanism is thus not available. The mechanism of dislocation bow-out can also not be represented at the continuum level, as the motion of individual dislocation segments is not taken into account. In Section 5.3.2, small-scale plasticity effects during unloading were however observed, caused by residual stresses, leading to an additional strain component on top of the elastic unloading strain. If anelasticity effects could be explained by the residual stresses originating from differences in grain orientations in a polycrystalline material, as found by Hill [8], this would be observable from the simulation results. To investigate upon the prediction of anelasticity by a gradient-enhanced crystal plasticity model, the following research question is posed:

Research Question 1.3

To what extent can anelasticity effects be explained by microplasticity effects due to residual stresses originating from plastic anisotropy using a gradient-enhanced crystal plasticity model?

5.4.1 Setting up the FEM-models

Within this section, simulations will be performed using models identical to those in Section 5.3.1. 32-hexagonal-grain periodic RVEs representing a 6000-series aluminium alloy and a DP600-grade dual phase steel are used. GNDs are included in the hardening model for all simulations.

The models will be subjected to a loading-unloading-reloading deformation. In the initial load step, the RVEs are uniaxially strained up to 0.5, 1.0, 1.5 and 2.0% engineering strain (aluminium) and 3 and 4% engineering strain (DP-steel). After that, the strain level is reduced such that the macroscopic stress in loading direction goes to 0. The amount of strain corresponding to the point of zero stress is obtained from the unloading curves in Figures 5.16a and 5.17. Finally, the material is strained up to the respective prestrain level again and deformation is continued up to 1.1 times that level.

5.4.2 Results and discussion

The stress-strain plots for the various simulations are shown in Figure 5.22. Once the stress level is lowered, the slope of the unloading curve is virtually identical to that of the initial elastic part. The same applies for the reloading curves. A small amount of hysteresis in the unloading-loading curves is however observed in all simulations. This effect becomes more notable if the prestrain level is increased and is shown clearly in the magnified sections of the plots. As soon as the reloading stress approaches the prestress level, the curves sharply bend over and continue as if the tensile loading had not been interrupted. This sharp elastoplastic transition after tensile reloading is in line with experimentally observed behaviour [52].

The Kocks-Mecking plots, which show the instantaneous modulus $\Theta = d\sigma/d\epsilon$ versus stress, are shown for both materials in Figure 5.23. They are normalised with respect to the elastic moduli. A reduction of the effective unloading modulus with decreasing load is observed. Initially, the unloading modulus equals the elastic one. At the end of reloading, the effective modulus is 0.26% less than the elastic modulus at 2% prestrain for aluminium and 0.78% at 4% prestrain for DP-steel. Small amounts of anelastic strain are thus present in unloading. The effective modulus during reloading is equal to the elastic modulus up to the point where macroscopic flow is observed, characterised by the sharp drop in the Kocks-Mecking plot. This indicates that no additional anelastic strain component is present during reloading.

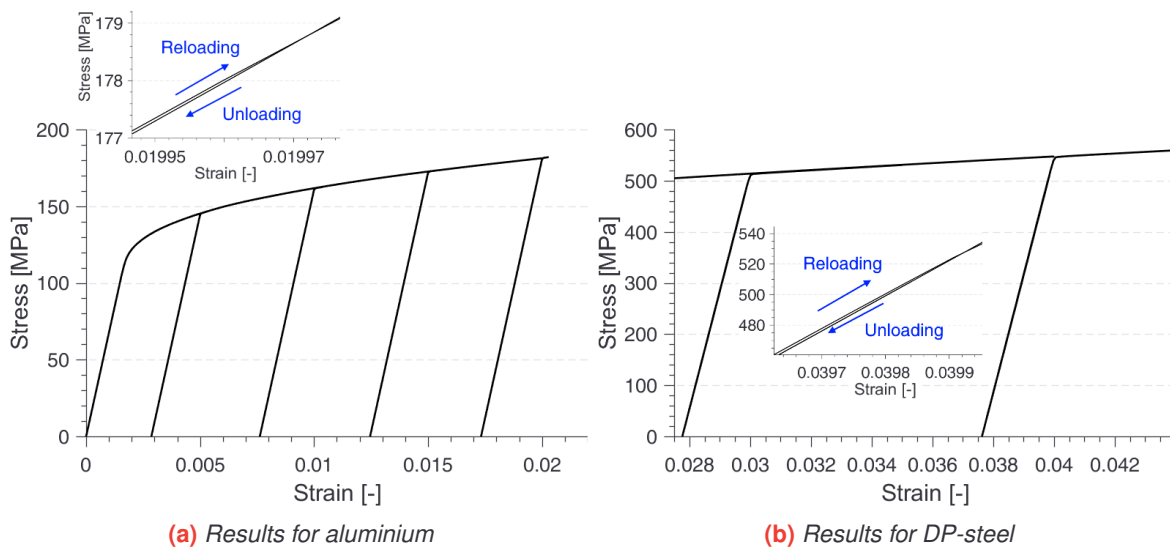


Figure 5.22: Stress-strain curves for the anelasticity simulations

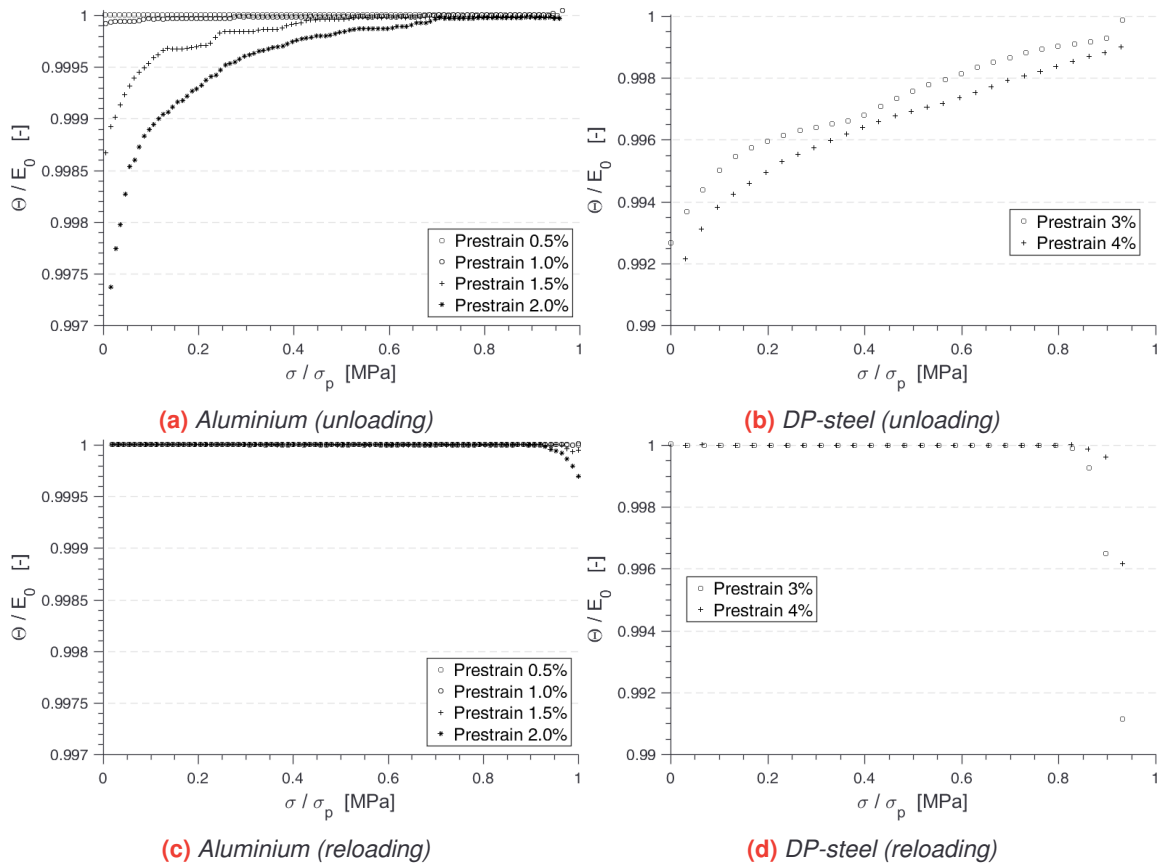


Figure 5.23: Kocks-Mecking plots for the anelasticity simulations

In their paper, Cleveland and Gosh [9] describe the evolution of experimentally obtained Kocks-Mecking plots for the unloading of aluminium 6022 and a high strength steel. They observe reductions of the instantaneous moduli up to 12% and 22%, respectively. This is significantly more than found from the simulations. Furthermore, the initial unloading modulus does not equal the elastic modulus but is reduced rapidly by 6-10% immediately after load reversal. This reduction is also observed in the experimental results in [53, 55]. The simulated behaviour in the reloading step contradicts with the findings in [55], where the instantaneous modulus decreases gradually upon reloading too. Anelasticity effects are thus not represented completely by the crystal plasticity model, even though some departures from linear unloading behaviour are seen.

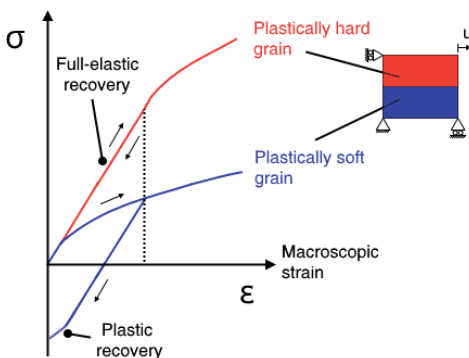


Figure 5.24: Mechanism for plastic slip during unloading

To determine the cause of this underprediction, the underlying mechanism for the observed behaviour will be identified. When comparing the slip levels at the start and end of the unloading phase, it is seen that small differences arise around locations at which most slip has accumulated as indicated in Figure 5.25. Plastic slip in unloading thus only occurs in the plastically weakest grains and can be explained by plastic anisotropy as in Figure 5.24. If strain recovery in the plastically hardest grains is fully elastic, an amount of plasticity is required for strain recovery in the plastically weakest grain if the difference in the onset of plastic deformation is large enough. When the evolution of plastic slip in the plastically weakest grains is investigated, the following is recognised:

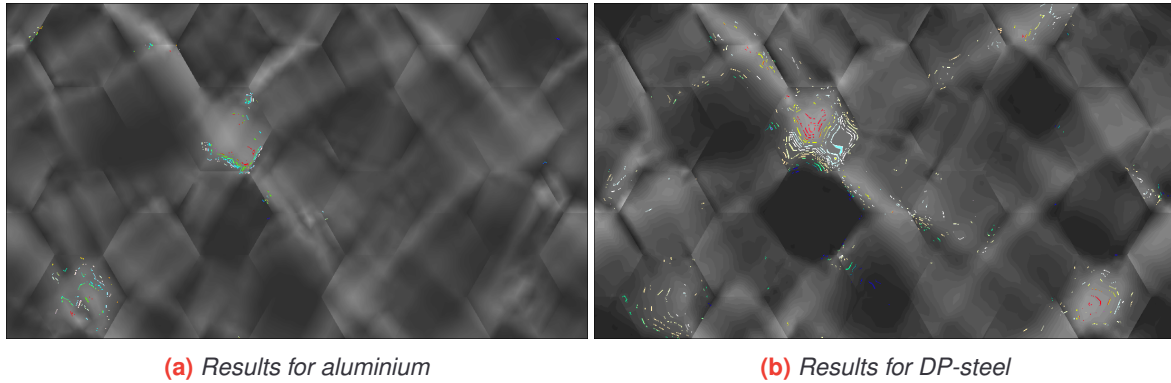


Figure 5.25: Locations with additional plastic slip during unloading

- Anelastic effects are caused by increasing amounts of plastic slip on slip systems that were not or significantly less active than the systems accountable for the majority of the deformation during preloading.
- In the reloading step, plastic strain after elastic deformation initiates from those slip systems that were most active during preloading.

It is thus shown that load reversal gives rise to slip on systems that were less favourably oriented during forward loading. As these systems have hardened less, small amount of plastic slip can accumulate during unloading relatively easy, leading to the observed macroscopic anelasticity effect. As the additional plastic slip during unloading is small compared to that accumulated during preloading, no noteworthy changes are made to the slip and dislocation density distributions. Hence, tensile reloading activates the same slip systems that were active in preloading. As they have already hardened, the material first behaves elastically. Only as the stress level starts to reach the preload stress, the critically resolved shear stresses resulting from this hardening are overcome and macroscopic yielding starts. This explains why no nonlinearities are observed during reloading.

The observed effects are thus solely manifestations of small scale plasticity resulting plastic anisotropy and differences in slip system hardening. This is in accordance with the findings in [51]. From the present results it can neither be deduced with certainty whether or not such small-scale plasticity effects are the underlying mechanism for anelasticity, nor is fully determined whether these effects are predicted to the right extent by the current FEM-models.

The nature of the RVEs will namely influence the macroscopic response. They are currently limited to the two-dimensional space, whereas only in three dimensions the anisotropic nature of the grains is fully captured. A more realistic three-dimensional stress state in combination with plastic anisotropy may enhance differences in slip system hardening and thus result in a wider distribution of stresses in the material. The same is true if a non-uniform grain size distribution is chosen [49]. As wider stress distributions were shown to earlier initiate plastic deformation after load removal in Section 5.3.2, it is expected that anelasticity effects caused by small-scale plasticity become more pronounced. Results from two-dimensional RVEs with realistic grain morphology [57] have indeed shown larger nonlinearities in unloading than were observed in Figure 5.22.

If better fitting results cannot be obtained using realistic, three-dimensional models, one could raise the assumption that the current crystal plasticity formulation is unable to capture the underlying physics of anelasticity effects. Given the excellent resemblance of unloading-reloading curves for a HCT780 grade steel obtained by a constitutive model based upon the dislocation bow-out mechanism in [53], it can be argued that additional detail about the dislocation structure is to be added to the model formulation. This would enable to capture deformations that are not a result of atomic bond stretching (as elastic deformation), nor result from an increase in the number of dislocations (as plastic deformation), but results from reversible dislocation motions within the developed dislocation structure.

5.4.3 Conclusions and recommendations

A small amount of anelasticity was observed in the unloading curves of aluminium and dual-phase steel. With increasing prestrain, its magnitude increases. The observed effects are caused by small scale plasticity resulting from the different orientations of the material's slip systems and plastic anisotropy. Compared to experimental results, the reduction of the unloading moduli is underpredicted to a great extent. Further simulations should be performed on three-dimensional RVEs with realistic grain morphology to see if this underprediction can be explained by the FEM-models. Including dislocation structure details in the crystal plasticity formulation could help to be able to describe reversible dislocation motion without the necessity of increasing the dislocation density.

Research Question 1.3 - Answer

Microplasticity effects originating from plastic anisotropy and differences in slip system hardening add an additional strain component to the elastic unloading strain, leading to anelasticity. Its magnitude was however significantly underpredicted by the current simulations.

6 | Experimental validation of the GND-evolution

From the various simulation results, a linear increase in the total number of GNDs as function of macroscopic strain was observed. Additionally, GNDs primarily formed near grain boundaries. To be able to assess the validity of the crystal plasticity model used in this work, it has to be determined whether or not this behaviour is in accordance with the real-life material response.

In order to do so, a method that can be used to determine the GND densities within a material is required. Using electronic backscatter diffraction (EBSD), it is possible to study crystallographic orientations. Local changes in crystallographic orientation (of points within one grain) are a manifestation of lattice curvature. As introduced before, GNDs are required to account for such gradients. It is therefore possible to relate local orientation changes to the densities of geometrically necessary dislocation. Results from EBSD measurements can thus be used to characterise GND densities.

In their paper, Calcagnotto et. al. [58] compare two methods for this purpose. The first method is based on the work of Kubin and Mortensen [59] and uses the kernel average misorientation (KAM), that is directly found from the EBSD data, as measure for the local misorientation angle φ . The second method is adopted from the work of Demir et. al. [60] and uses the full dislocation tensor to determine the GND density. It was concluded that both methods are appropriate for the calculation of GND densities from EBSD data. The first method will be used within this work for its simplicity. The GND density can then be found from

$$\rho_{\text{GND}} = \frac{2\varphi}{ub} \quad (6.1)$$

where u is the unit length in which the curvature is to be accommodated for and b is the length of the Burgers vector.

The aim of this section is to provide a quantitative comparison between simulation outcomes and experimental results in terms of the evolution behaviour of GNDs. This will be done by comparing experimentally characterised GND-density distributions and total GND numbers at various strain levels with results from a simulated RVE with material parameters fitted to the response of the experimentally tested material.

6.1 Methods

Determining macroscopic response

Experimental characterisation of the material is performed using the Kammrath & Weiss tension-compression module. It can be placed directly under a microscope to be able to photograph the sample during deformation. Tensile specimens fitting the module are laser cut from a sheet of interstitial free (IF) steel. The samples are aligned in the rolling direction of the sheet. To be able to graphically evaluate deformations, a square pattern consisting of four dots is painted onto one side of each specimen using black silicone kit.

One specimen is placed in the tensile stage, after which the module is positioned under a stereo microscope. An image of the dots in the reduced section is captured to serve as reference for the strain calculations. The specimen is now elongated while recording the tensile load. Elongation is increased in regular intervals. At the end of each interval, a further image of the dots is taken. This process is repeated until the material reaches its ultimate tensile strength, marked by the moment where the applied load first decreases with increasing elongation.

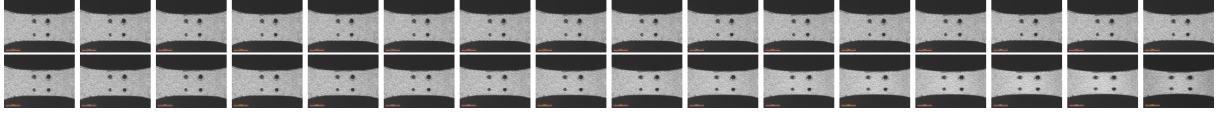


Figure 6.1: Microscope images used for quantifying the stress-strain response of IF-steel. *Top left: no deformation, bottom right: deformation after reaching UTS*

Strains are calculated from the images in Figure 6.1 by measuring the spacing between two dots aligned horizontally in tensile direction using

$$\epsilon_{xx,i} = \frac{\Delta x_i - \Delta x_0}{\Delta x_0} \quad (6.2)$$

where Δx_i is the interdot spacing in image i and Δx_0 is the interdot spacing in the original image. Stresses are found by dividing the maximum load prior to interruption by the nominal area of the tensile specimen, 3.00 x 0.70 mm.

Experimental characterisation of GND-densities

GND-densities will be characterised for three samples, elongated with 100, 200 and 300 μm , respectively. For each sample, a microscope image is captured prior and after completion of the deformation process to determine the strain level. The reduced regions are cut out of the deformed specimens. A further sample is cut out of an undeformed specimen to serve as reference for the initial GND-density distribution. The cut parts are placed together in a cylindrical mount.

The mounted sample is grinded in multiple steps using silicon carbide grinding paper, the coarsest grit being 500 and the finest grit being 4000. Polishing is done in multiple steps using diamond suspensions ranging from 9 to 0.25 μm grain size and finished by a silica suspension with a grain size of 0.04 μm .

An EBSD analysis is then performed on each sample, capturing a rectangular area of 160x120 μm with a resolution of 0.1289 μm . KAM data is obtained for each sample by postprocessing the EBSD-results. A kernel size of 5x5 pixels is used, corresponding to second neighbour rank. Misorientations can be calculated between the central pixel and each pixel within its surrounding kernel using

$$\varphi = \cos^{-1} \left(\frac{1}{2} \left[\max_{i,j} \text{Tr} (\mathbf{S}_i \mathbf{G}_c \mathbf{G}_k^{-1} \mathbf{S}_j) - 1 \right] \right) \quad (6.3)$$

where \mathbf{G}_c and \mathbf{G}_k are the orientation matrices for the central and kernel pixel, respectively and \mathbf{S}_i are the proper symmetry matrices listed in Table E.2. The orientation matrices can be calculated from the EBSD-obtained Euler angles according to (E.3) in Appendix E. The KAM-calculations are performed using the Matlab toolbox MTEX [61]. Kernel pixels with misorientations larger than 2° are excluded from the calculations.

Numerical comparison

A simulation is performed on the same 64-grained FE-model as shown in Figure 5.5. A BCC crystal structure is assigned to the grains to represent the ferrite phase in the IF-steel. The grain size is set to the average grain size of the experimentally characterised samples, being 12 μm as found after running a grain detection algorithm on the EBSD-data. The sample is strained up to 8% engineering strain. The material parameters are fitted to the experimentally determined response and are shown in Table 6.1.

E [MPa]	ν [-]	b [nm]	c [-]	$\rho_{\text{SSD}}^{0,(\alpha)}$ [mm ⁻²]	$\rho_{\text{SSD}}^{\infty,(\alpha)}$ [mm ⁻²]	γ^∞ [-]	τ_0 [MPa]	$Q_0^{\alpha\beta} - Q_5^{\alpha\beta}$ [-]
208199	0.3	0.286	0.1	$1 \cdot 10^7$	$2 \cdot 10^9$	1.0	25	1.0, 1.4, 1.4, 1.4, 1.4, 1.4

Table 6.1: Material parameters used in the validation simulations

6.2 Results

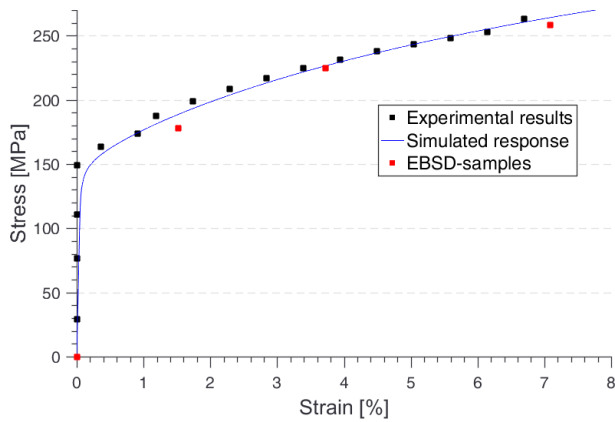


Figure 6.2: Experimentally and numerically obtained stress-strain results for IF-steel

The stress-strain data retrieved from the microscope images is shown in Figure 6.2, together with the best fit to this data obtained from the crystal plasticity simulation. The experimentally determined stress-strain points for the samples analysed using EBSD are included in this figure too. The numerical fit to the simulation data is good, but it must be noted that the value of the Taylor factor ($c = 0.1$) is relatively low, indicating the magnitude of the dislocation-induced work-hardening is high.

The crystallographic orientations obtained from the EBSD-measurements are shown in Figure 6.3 together with the detected grain boundaries. The elongation of the grains with strain

can clearly be seen from these plots. The KAM-values as derived from this data are visualised in Figure 6.4. It is shown that some scratches remain after polishing, as apparent from the straight lines running from one edge of the image to the other. Comparing both figures shows that high misorientations are present around grain boundaries. High misorientation values also occur as parallel and evenly spaced lines within grains.

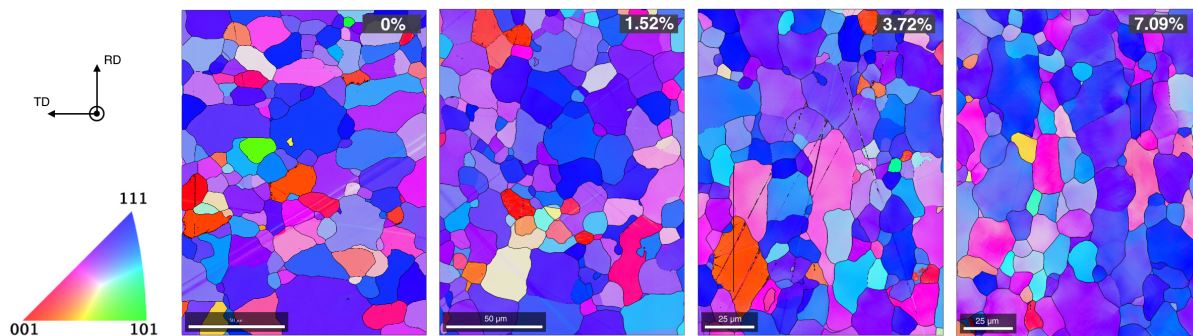


Figure 6.3: Crystal orientations obtained using EBSD. Orientation colour code indicates pole orientations aligned with the out-of-plane direction of the sample.

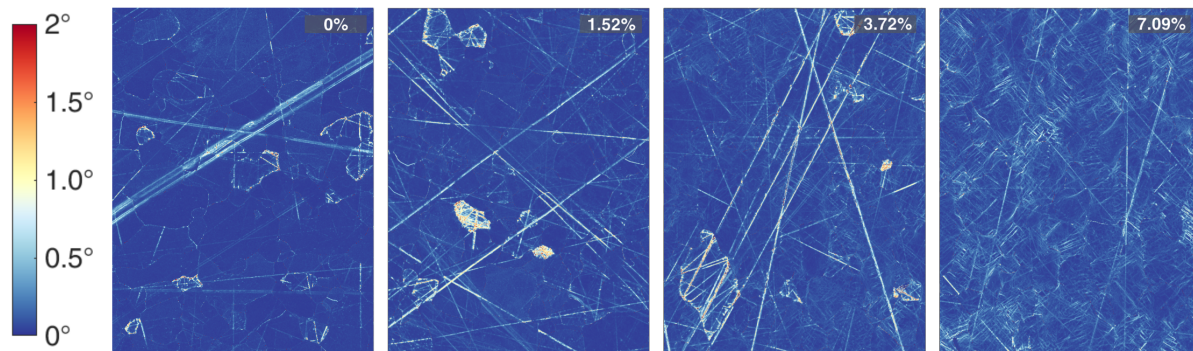


Figure 6.4: KAM-results obtained from the EBSD-data

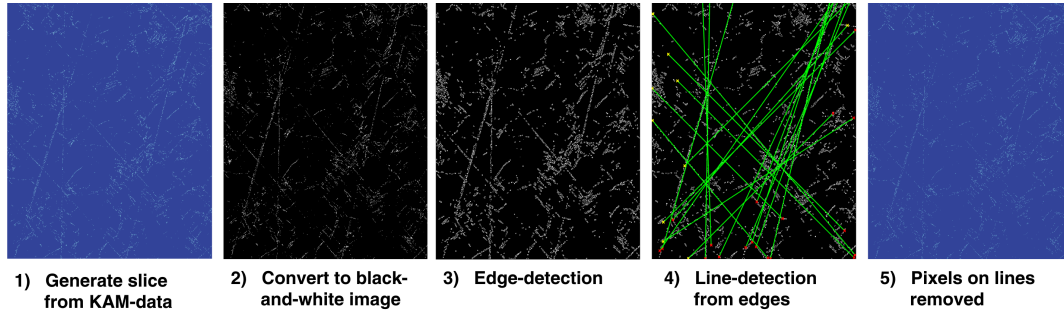


Figure 6.5: Visualisation of scratch-removal filtering steps for one KAM-data image slice

To filter the scratches left from polishing, a line detection algorithm is employed to the KAM-image following the approach of [62]. Its subsequent steps are schematically shown in Figure 6.5. The image is first split up into slices containing misorientation angles $0-0.2^\circ$, $0.2-0.3^\circ$, $0.3-0.4^\circ$, \dots , $0.9-1^\circ$, $1-1.25^\circ$, $1.25-1.5^\circ$, \dots , $1.75-2^\circ$. Each slice is converted into a black-and-white image, from which the edges are detected. The Hough-transform of the edge detection image is computed. Peaks in the Hough transform are used to detect straight lines in the image's edges. For the line finding function, a minimum length of 10 pixels is selected. Gaps between aligned line segments are filled up to 500 pixels. Pixels on identified lines are removed from the data set if the total line length exceeds 140 pixels. A limit is set to the maximum number of lines that may be removed per step. The detection-and-deletion process is repeated 5 times per image slice to remove the full width of the scratches. The remaining data points of the slices are then assembled together again to form the cleaned KAM-image.

Each data point in the cleaned KAM-image is assigned a GND-density using (6.1). The Burgers vector length b is $2.86 \cdot 10^{-7}$ mm and the unit length u is $0.129 \cdot 10^{-3}$ mm, corresponding to the EBSD pixel size. The maximum number of lines removed per filter step is set to 20 to generate the plots. The resulting GND-density distributions are visualised in Figure 6.6a. As they directly correlate with the KAM-values, it is seen here too that GNDs form near grain boundaries, but also in regular patterns within grains. With increasing strain, the overall number of GNDs within the material increases. Numerically obtained GND-density distributions are evaluated at strain levels comparable to those of the experimental data. The results are visualised in Figure 6.6b. GNDs are forming primarily around grain boundaries and their number increases with strain.

The total number of GNDs is calculated by multiplying each pixel's density by the pixel area and summing over the total number of pixels. To allow for comparison between the experimental datasets, the total GND number is divided by the area of the set of pixels \mathcal{A} that were not removed during the scratch-removal procedure:

$$\bar{n}_{\text{GND}} = \frac{\sum_{i=1}^n \rho_{\text{GND},i} A_i}{\sum_{j \in \mathcal{A}} A_j} \quad (6.4)$$

Averaged total GND-numbers from simulations are found using the approach in Appendix F. A qualitative comparison of the evolution of the total GND number with strain between experimental and simulation outcomes is shown in Figure 6.7. For the experimental results, GND numbers obtained from unfiltered KAM-data are indicated together with those obtained from data filtered using the procedure described above. The maximum number of lines to be removed per filtering step is set to 20, 40 and 80 to indicate the effect of the filtering process.

The unfiltered experimental data does not show an increasing GND-number with strain. Such an increasing dislocation number would be expected though, as with ongoing tensile deformation differences in slip between grain boundary and core regions would increase due to the plastic inhomogeneity of the material. The resulting increase in slip gradients can only be present if the number of GNDs is raised too.

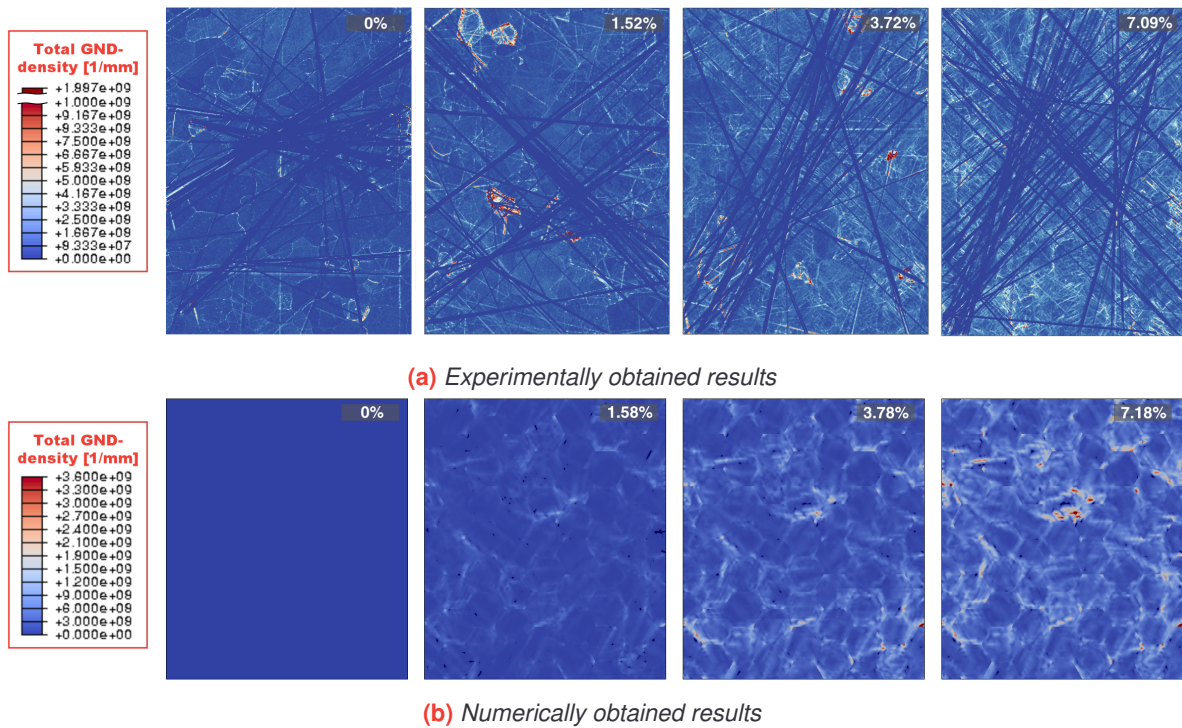


Figure 6.6: Evolution of GND-density distributions with strain

Experimental results from filtered KAM-data show that the GND-number decreases if the maximum number of filtered lines is increased. This indicates that there are still some scratches present in the cleaned KAM-data. The GND-evolution in the remaining unscratched regions shows an approximately linear dependence on the macroscopic strain for all filters. A linear increasing dislocation density with strain is observed from the simulations too. However, here the initial GND-number equals zero. This is similar to the results of the Hall-Petch simulations but contradicts the experimental findings.

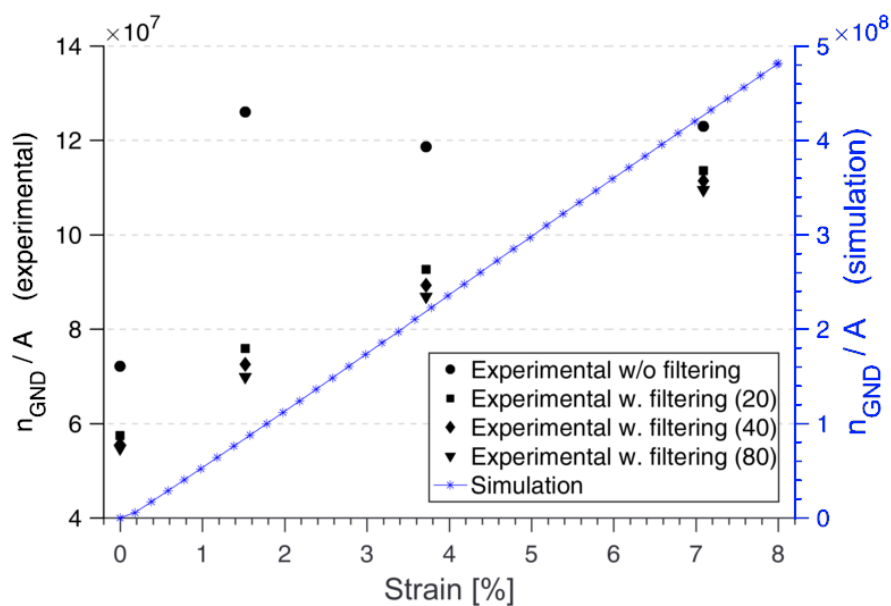


Figure 6.7: Evolution of the averaged GND-number with strain

6.3 Discussion of results

The evolution behaviour of GNDs is found comparable between experiments and simulations. No initial GND-distribution is observed in the numerical results, though. This is caused by the fact that initially, no plastic deformation is present in the material and thus no slip gradients are present. Only at the start of plastic deformation, GNDs start to form and evolve with deformation. Results from the cyclic loading tests performed using pre-deformed samples in Section 5.3.2 show that GND-numbers always increase linearly with strain, even if an initial dislocation distribution is present. Their evolution behaviour is thus maintained with the presence of an initial dislocation density. This indicates that the fit of the simulations with reality can be improved by a suitable GND-distribution initialisation strategy. It may even lower the GND-induced hardening rate, as the experimentally observed initial dislocation number results in a lower GND-generation rate.

In experiments, higher amounts of GNDs seem to be present within the core regions of the grains, especially at higher strain levels. The evenly spaced and parallel directions of the lines in which they tend to form within grains, may however indicate that these apparent GNDs are artefacts of remaining scratches on the material's surface. This aspect may thus require further investigation using even finer polished samples.

In a very recent publication, Kundu and Field [63] performed experiments similar to those within this work. They characterised GND densities in interstitial-free steel samples up to plastic strain of 13.6% using dislocation density tensors obtained by EBSD-measurements. They found a linear increase of the average GND-density, which is directly correlated to the averaged GND-number used in this work, with increasing strain. The GND-distribution showed concentration of GNDs near grain boundaries, just as observed experimentally and numerically in this work. The GND-patterns observed within grains as visual in Figure 6.6a are however not present. This raises the assumption that they indeed originate from polishing scratches.

6.4 Conclusions and recommendations

Experimentally obtained GND-distributions using EBSD-characterisation show that GNDs form primarily around grain boundaries and their number increases with strain. This behaviour is in accordance with the simulation results. The initial GND-distribution present in the experimental samples is missing in the numerical results and should be incorporated to improve the simulations. Plotting the total GND-numbers versus strain reveals that GND-numbers increase approximately linear with strain in both experiments and simulation. This is in accordance with recent experimental findings in literature and indicates the validity of the GND-calculations implemented in the crystal plasticity model. The correctness of simulated GND-distributions within grains needs to be further validated using finer polished samples to rule out artefacts from surface scratches.

7 | Conclusions

The elastic check in a conventional stress-update algorithm can be omitted if a suitable, continuously differentiable approximation of the max-function is applied to the flow-criteria. Within the crystal plasticity framework, the application of such a modified algorithm was found to be limited to problems with small incremental lattice rotations. For large incremental rotations, the stability of the active set of slip systems could not be maintained. Further research into the incorporation of stable tracking method for the active set is required for the modified code to become fully implementable.

The GND-density computation script that originated from the small-strain definition of the Burgers tensor is also applicable in a finite-strain framework. As prerequisite, the plastic slip gradients have to be projected onto slip systems that are expressed in the same (referential or spatial) configuration as these gradients. For the latter variant, a suitable lattice rotation update scheme has to be employed. The version based on referential gradients is most accurate in terms of modelling assumptions and most resistant against convergence errors in FEM-simulations.

Three macroscopic phenomena were investigated using two-dimensional, rectangular RVEs with hexagonal grains, being the Hall-Petch, Bauschinger and anelasticity effect. From these simulations, a number of general conclusions can be made. GNDs form primarily around grain boundaries, as caused by the presence of large slip gradients in these regions. Slip gradients near grain boundaries are a result of the plastic anisotropy of adjacent grains, which by the requirement of continuous deformations leads to differences in slip between a grains core and outer region. The total number of GNDs increases linearly with strain, whereas the SSD-number tends to saturate with increasing strain. The total GND-number is linearly dependent on the inversed grain size, originating directly from the Burgers vector length relating the slip gradients to the GND density.

The experimentally observed grain size-dependent work hardening behaviour as described by the Hall-Petch relation is captured very well by the gradient-enhanced crystal plasticity model. The presence of a realistic initial dislocation distribution can further enhance these results, as reasoned from the absence of a grain size-dependent initial yield stress. The Bauschinger effect as predicted by the crystal plasticity model was found to originate from a non-uniform stress-distribution within the material, caused by plastic anisotropy and the continuity requirement at grain boundaries. Incorporation of the GND density in the slip system hardening equations increases the magnitude of the Bauschinger effect by widening of these stress-distributions. This widening is attributed to the non-uniform distribution of GNDs over the grains. Fitting material data to an experimental tensile curve did not necessarily produce a good fit to experimental cyclic results. The clear influence of a pre-rolling step on the simulated macroscopic response however supports the hypothesis that the results can be improved if the material's deformation history is included in the simulations. In unloading, a nonlinear and increasingly reducing instantaneous modulus was observed. This qualitatively corresponds to anelasticity effects observed experimentally, but the magnitude of this effect was significantly underpredicted by the current implementation of the crystal plasticity model. The origin of the observed anelasticity lies in small-scale plastic deformation of a limited number of material points during unloading. Enhancement of the RVEs to three-dimensional models with realistic texture can increase the magnitude of anelasticity. Another option to improve its representation is to include reversible dislocation motion in the constitutive framework of the crystal plasticity model.

EBSD-characterised GND-density distributions in interstitial-free steel show GNDs primarily accumulate around grain boundaries. The total GND number rises almost linearly with strain and an initial dislocation density is present. The GND-evolution is thus found to be correctly predicted by the crystal plasticity model, but the initial dislocation density is to be included to improve the results.

Altogether, a gradient-enhanced crystal plasticity model can be regarded to be well applicable in predicting macroscopic phenomena that can clearly be related to size effects and plasticity effects resulting from plastic anisotropy of a material's constituent grains. It is not yet fully applicable to effects that may originate from microstructural effects that do not involve dislocation-generation, as is the case for the anelasticity effect.

Bibliography

- [1] F. Barlat, "Constitutive modeling for metals," in *Advanced methods in material forming*, pp. 1–18, Springer, 2007. (p. 1.)
- [2] D. Banabic, "Plastic behaviour of sheet metal," in *Sheet Metal Forming Processes*, pp. 27–140, Springer, 2010. (p. 1.)
- [3] G. E. Dieter and D. J. Bacon, *Mechanical metallurgy*, vol. 3. McGraw-Hill New York, 1986. (p. 1.)
- [4] J. Hu, B. Chen, D. J. Smith, P. E. J. Flewitt, and A. C. F. Cocks, "On the evaluation of the Bauschinger effect in an austenitic stainless steel - The role of multi-scale residual stresses," *International Journal of Plasticity*, vol. 84, pp. 203–223, 2016. (p. 1, 40, and 47.)
- [5] F. Roters, P. Eisenlohr, L. Hantcherli, D. D. Tjahjanto, T. R. Bieler, and D. Raabe, "Overview of constitutive laws, kinematics, homogenization and multiscale methods in crystal plasticity finite-element modeling: Theory, experiments, applications," *Acta Materialia*, vol. 58, no. 4, pp. 1152–1211, 2010. (p. 1, 2, and 4.)
- [6] L. P. Evers, W. A. M. Brekelmans, and M. G. D. Geers, "Scale dependent crystal plasticity framework with dislocation density and grain boundary effects," *International Journal of Solids and Structures*, vol. 41, no. 18-19, pp. 5209–5230, 2004. (p. 1, 2, 31, 32, 33, 37, and 38.)
- [7] W. Boas, "On the inhomogeneity of plastic deformation in metals," *Helvetica Physica Acta*, vol. 23, no. 1-2, pp. 159–166, 1950. (p. 1.)
- [8] B. Chen, J. N. Hu, Y. Q. Wang, S. Y. Zhang, S. Van Petegem, A. C. F. Cocks, D. J. Smith, and P. E. J. Flewitt, "Role of the misfit stress between grains in the Bauschinger effect for a polycrystalline material," *Acta Materialia*, vol. 85, pp. 229–242, 2015. (p. 1, 40, and 47.)
- [9] R. M. Cleveland and A. K. Ghosh, "Inelastic effects on springback in metals," *International Journal of Plasticity*, vol. 18, no. 5-6, pp. 769–785, 2002. (p. 1, 49, and 51.)
- [10] C. Soyarslan, E. S. Perdahcioğlu, E. E. Aşık, A. H. Van Den Boogaard, and S. Bargmann, "Implementation and application of a gradient enhanced crystal plasticity model," in *AIP Conference Proceedings*, vol. 1896, p. 160008, AIP Publishing, 2017. (p. 1, 6, 8, 9, 11, and 12.)
- [11] D. Peirce, R. J. Asaro, and A. Needleman, "An analysis of nonuniform and localized deformation in ductile single crystals," *Acta Metallurgica*, vol. 30, no. 6, pp. 1087–1119, 1982. (p. 1.)
- [12] M. Becker, *Incompatibility and instability based size effects in crystals and composites at finite elastoplastic strains*. PhD thesis, University of Stuttgart, 2006. (p. 1, 2, 6, 7, 31, 32, 34, and 37.)
- [13] L. P. Evers, D. M. Parks, W. A. M. Brekelmans, and M. G. D. Geers, "Crystal plasticity model with enhanced hardening by geometrically necessary dislocation accumulation," *Journal of the Mechanics and Physics of Solids*, vol. 50, no. 11, pp. 2403–2424, 2002. (p. 2, 31, and 33.)
- [14] S. Wulfinghoff, E. Bayerschen, and T. Böhlke, "A gradient plasticity grain boundary yield theory," *International Journal of Plasticity*, vol. 51, pp. 33–46, 2013. (p. 33.)
- [15] S. Haouala, J. Segurado, and J. LLorca, "An analysis of the influence of grain size on the strength of FCC polycrystals by means of computational homogenization," *Acta Materialia*, vol. 148, pp. 72–85, 2018. (p. 2 and 31.)
- [16] J. H. Kim, D. Kim, F. Barlat, and M.-G. Lee, "Crystal plasticity approach for predicting the Bauschinger effect in dual-phase steels," *Materials Science and Engineering: A*, vol. 539, pp. 259–270, 2012. (p. 2 and 41.)
- [17] L. Li, L. Shen, and G. Proust, "A texture-based representative volume element crystal plasticity model for predicting Bauschinger effect during cyclic loading," *Materials Science and Engineering: A*, vol. 608, pp. 174–183, 2014. (p. 2, 40, and 47.)

- [18] I. Ertürk, J. A. W. Van Dommelen, and M. G. D. Geers, "Gradient crystal plasticity modelling of anelastic effects in particle strengthened metallic thin films," *Meccanica*, vol. 49, no. 11, pp. 2657–2685, 2014. (p. 2.)
- [19] M. F. Ashby, "The deformation of plastically non-homogeneous materials," *Philosophical Magazine*, vol. 21, no. 170, pp. 399–424, 1970. (p. 2.)
- [20] J. F. Nye, "Some geometrical relations in dislocated crystals," *Acta metallurgica*, vol. 1, no. 2, pp. 153–162, 1953. (p. 2.)
- [21] U. F. Kocks, "The relation between polycrystal deformation and single-crystal deformation," *Metallurgical and Materials Transactions B*, vol. 1, no. 5, pp. 1121–1143, 1970. (p. 2, 38, and 40.)
- [22] A. W. Thompson, M. I. Baskes, and W. F. Flanagan, "The dependence of polycrystal work hardening on grain size," *Acta Metallurgica*, vol. 21, no. 7, pp. 1017–1028, 1973. (p. 2, 38, and 40.)
- [23] E. Stein, R. de Borst, and T. Hughes, *Encyclopedia of computational mechanics*. No. v. 2 in Encyclopedia of Computational Mechanics, John Wiley, 2004. (p. 4, 8, 10, and 11.)
- [24] M. E. Gurtin, E. Fried, and L. Anand, *The mechanics and thermodynamics of continua*. Cambridge University Press, 2010. (p. 4 and 7.)
- [25] F. Roters, P. Eisenlohr, T. R. Bieler, and D. Raabe, *Crystal plasticity finite element methods: in materials science and engineering*. John Wiley & Sons, 2011. (p. 6.)
- [26] A. Arsenlis and D. M. Parks, "Crystallographic aspects of geometrically-necessary and statistically-stored dislocation density," *Acta materialia*, vol. 47, no. 5, pp. 1597–1611, 1999. (p. 7 and 8.)
- [27] N. A. Fleck, G. M. Muller, M. F. Ashby, and J. W. Hutchinson, "Strain gradient plasticity: theory and experiment," *Acta Metallurgica et Materialia*, vol. 42, no. 2, pp. 475–487, 1994. (p. 8.)
- [28] C. Miehe and J. Schröder, "A comparative study of stress update algorithms for rate-independent and rate-dependent crystal plasticity," *International Journal for Numerical Methods in Engineering*, vol. 50, no. 2, pp. 273–298, 2001. (p. 8, 9, 10, 11, and 24.)
- [29] E. S. Perdahcioğlu, "Lattice rotation update in crystal plasticity," 2017. (p. 11, 66, and 67.)
- [30] T. Liszka and J. Orkisz, "The finite difference method at arbitrary irregular grids and its application in applied mechanics," *Computers and structures*, vol. 11, no. 1-2, pp. 83–95, 1980. (p. 12.)
- [31] M. E. Gurtin, "The Burgers vector and the flow of screw and edge dislocations in finite-deformation single-crystal plasticity," *Journal of the Mechanics and Physics of Solids*, vol. 54, no. 9, pp. 1882–1898, 2006. (p. 22, 23, 26, and 27.)
- [32] P. Cermelli and M. E. Gurtin, "On the characterization of geometrically necessary dislocations in finite plasticity," *Journal of the Mechanics and Physics of Solids*, vol. 49, no. 7, pp. 1539–1568, 2001. (p. 23.)
- [33] S. Yadegari, S. Turteltaub, A. S. J. Suiker, and P. J. J. Kok, "Analysis of banded microstructures in multiphase steels assisted by transformation-induced plasticity," *Computational Materials Science*, vol. 84, pp. 339–349, 2014. (p. 29 and 36.)
- [34] W. A. Counts, M. V. Braginsky, C. C. Battaile, and E. A. Holm, "Predicting the Hall–Petch effect in fcc metals using non-local crystal plasticity," *International Journal of Plasticity*, vol. 24, no. 7, pp. 1243–1263, 2008. (p. 29, 31, 32, and 37.)
- [35] M. Kraska, M. Doig, D. Tikhomirov, D. Raabe, and F. Roters, "Virtual material testing for stamping simulations based on polycrystal plasticity," *Computational Materials Science*, vol. 46, no. 2, pp. 383–392, 2009. (p. 29.)
- [36] J. W. Morris, "The influence of grain size on the mechanical properties of steel," tech. rep., Lawrence Berkeley National Lab.(LBNL), Berkeley, CA (United States), 2001. (p. 31.)
- [37] Y. Li, A. J. Bushby, and D. J. Dunstan, "The Hall–Petch effect as a manifestation of the general size effect," *Proc. R. Soc. A*, vol. 472, no. 2190, p. 20150890, 2016. (p. 31.)
- [38] K. S. Cheong, E. P. Busso, and A. Arsenlis, "A study of microstructural length scale effects on the behaviour of FCC polycrystals using strain gradient concepts," *International Journal of Plasticity*, vol. 21, no. 9, pp. 1797–1814, 2005. (p. 31 and 32.)

- [39] J. K. Mackenzie, "Second paper on statistics associated with the random disorientation of cubes," *Biometrika*, vol. 45, no. 1-2, pp. 229–240, 1958. (p. 33, 74, and 75.)
- [40] R. W. K. Honeycombe, *The plastic deformation of metals*. London: Edward Arnold (Publishers) Ltd., 2 ed., 1984. (p. 34.)
- [41] I. Kovacs, N. Q. Chinh, and E. Kovács-Csetényi, "Grain size dependence of the work hardening process in Al99.99," *physica status solidi (a)*, vol. 194, no. 1, pp. 3–18, 2002. (p. 38.)
- [42] G. J. Weng, "Constitutive equations of single crystals and polycrystalline aggregates under cyclic loading," *International Journal of Engineering Science*, vol. 18, no. 12, pp. 1385–1397, 1980. (p. 40 and 47.)
- [43] X. Hu, C. Wei, H. Margolin, and S. Nourbakhsh, "The Bauschinger effect and the stresses in a strained single crystal," *Scripta Metallurgica et Materiala*, vol. 27, no. 7, pp. 865–870, 1992. (p. 40.)
- [44] C. J. Bayley, W. A. M. Brekelmans, and M. G. D. Geers, "A comparison of dislocation induced back stress formulations in strain gradient crystal plasticity," *International Journal of Solids and Structures*, vol. 43, no. 24, pp. 7268–7286, 2006. (p. 40.)
- [45] L. S. Tóth, A. Molinari, and N. Zouhal, "Cyclic plasticity phenomena as predicted by polycrystal plasticity," *Mechanics of Materials*, vol. 32, no. 2, pp. 99–113, 2000. (p. 40.)
- [46] A. A. Mamun, R. J. Moat, J. Kelleher, and P. J. Bouchard, "Origin of the Bauschinger effect in a polycrystalline material," *Materials Science and Engineering: A*, vol. 707, pp. 576–584, 2017. (p. 40.)
- [47] T. Kuwabara, "Advances of plasticity experiments on metal sheets and tubes and their applications to constitutive modeling," in *AIP Conference Proceedings*, vol. 778, pp. 20–39, AIP, 2005. (p. 41.)
- [48] G. G. Yapici, I. J. Beyerlein, I. Karaman, and C. N. Tome, "Tension–compression asymmetry in severely deformed pure copper," *Acta Materialia*, vol. 55, no. 14, pp. 4603–4613, 2007. (p. 45.)
- [49] B. Raeisinia, *Modelling the effect of grain size distribution on the mechanical response of metals*. PhD thesis, University of British Columbia, 2008. (p. 45 and 52.)
- [50] N. Brown, *Microplasticity*, ch. Observations in microplasticity, pp. 45–73. New York: Interscience Publishers, 1968. (p. 48 and 49.)
- [51] T. Hama, R. Matsudai, Y. Kuchinomachi, H. Fujimoto, and H. Takuda, "Non-linear deformation behavior during unloading in various metal sheets," *ISIJ International*, vol. 55, no. 5, pp. 1067–1075, 2015. (p. 48 and 52.)
- [52] R. Hill, *The mathematical theory of plasticity*, vol. 11. Oxford University Press, 1998. (p. 48 and 50.)
- [53] A. Torkabadi, P. Van Liempt, V. T. Meinders, and A. H. Van den Boogaard, "A constitutive model for the anelastic behavior of advanced high strength steels," in *COMPLAS XIII: proceedings of the XIII International Conference on Computational Plasticity: fundamentals and applications*, pp. 378–385, CIMNE, 2015. (p. 49, 51, and 52.)
- [54] P. van Liempt and J. Sietsma, "A physically based yield criterion i. determination of the yield stress based on analysis of pre-yield dislocation behaviour," *Materials Science and Engineering: A*, vol. 662, pp. 80–87, 2016. (p. 49.)
- [55] Z. Arechabaleta, P. van Liempt, and J. Sietsma, "Quantification of dislocation structures from anelastic deformation behaviour," *Acta Materialia*, vol. 115, pp. 314–323, 2016. (p. 49 and 51.)
- [56] L. Sun and R. Wagoner, "Complex unloading behavior: Nature of the deformation and its consistent constitutive representation," *International Journal of Plasticity*, vol. 27, no. 7, pp. 1126–1144, 2011. (p. 49.)
- [57] A. Torkabadi, *Towards an Accurate Spring-back Prediction, Experiments and Modeling*. PhD thesis, University of Twente, To be published. (p. 52.)
- [58] M. Calcagnotto, D. Ponge, E. Demir, and D. Raabe, "Orientation gradients and geometrically necessary dislocations in ultrafine grained dual-phase steels studied by 2d and 3d ebsd," *Materials Science and Engineering: A*, vol. 527, no. 10-11, pp. 2738–2746, 2010. (p. 54.)

- [59] L. Kubin and A. Mortensen, "Geometrically necessary dislocations and strain-gradient plasticity: a few critical issues," *Scripta materialia*, vol. 48, no. 2, pp. 119–125, 2003. (p. 54.)
- [60] E. Demir, D. Raabe, N. Zaafarani, and S. Zaeferrer, "Investigation of the indentation size effect through the measurement of the geometrically necessary dislocations beneath small indents of different depths using ebsd tomography," *Acta Materialia*, vol. 57, no. 2, pp. 559–569, 2009. (p. 54.)
- [61] R. Krakow, R. J. Bennett, D. N. Johnstone, Z. Vukmanovic, W. Solano-Alvarez, S. J. Lainé, J. F. Einsle, P. A. Midgley, C. M. Rae, and R. Hielscher, "On three-dimensional misorientation spaces," *Proceedings of the Royal Society of London A*, vol. 473, no. 2206, p. 20170274, 2017. (p. 55.)
- [62] The MathWorks, Inc., "Image processing toolbox - user's guide," Natick, 2018. Retrieved from https://www.mathworks.com/help/pdf_doc/images/images_tb.pdf, accessed September 2018. (p. 57.)
- [63] A. Kundu and D. P. Field, "Geometrically necessary dislocation density evolution in interstitial free steel at small plastic strains," *Metallurgical and Materials Transactions A*, vol. 49, no. 8, pp. 3274–3282, 2018. (p. 59.)
- [64] S. Kok, A. J. Beaudoin, and D. A. Tortorelli, "Numerical integration of lattice rotation in polycrystal plasticity," *International Journal for Numerical Methods in Engineering*, vol. 52, no. 12, pp. 1487–1500, 2001. (p. 66.)
- [65] A. Becker, "Sampling a uniformly random rotation," 2012. Retrieved from <http://demonstrations.wolfram.com/SamplingAUniformlyRandomRotation/>, accessed May 2018. (p. 73.)
- [66] D. Depriester, "Computing Euler angles with Bunge convention from rotation matrix," 2018. Retrieved from https://www.researchgate.net/publication/324088567_Computing_Euler_angles_with_Bunge_convention_from_rotation_matrix, accessed May 2018. (p. 73.)

Appendices

A | Derivation of kinematical model assuming small elastic stretch

The aim of this section is to derive the kinematical description of finite strain crystal plasticity under the assumption of small elastic stretch and arbitrary large plastic deformation. The derivation serves as validation of the kinematical basis for the lattice rotation update that is currently implemented in the stress update algorithm of the crystal plasticity finite element model, as described by Perdahcioğlu [29].

The kinematic framework for a crystal plasticity model is commonly based on a multiplicative split of the deformation gradient, also known as the Kröner decomposition:

$$\mathbf{F} = \mathbf{F}_e \mathbf{F}_p \quad (\text{A.1})$$

An intermediate configuration is defined that leaves the crystal lattice of the material undistorted and unrotated. The plastic deformation gradient \mathbf{F}_p maps the initial configuration \mathbb{B}_0 to this fictitious intermediate configuration $\hat{\mathbb{B}}$. It is defined such that the lattice rotation is completely included in the elastic deformation gradient \mathbf{F}_e , which maps the intermediate configuration to the current configuration \mathbb{B} . This decomposition forms the basis for [29].

Kok et. al. [64] use the polar decomposition of the elastic deformation gradient into $\mathbf{F}_e = \mathbf{V}\mathbf{R}$, with \mathbf{V} the left stretch tensor and \mathbf{R} the rotation tensor, to define another intermediate configuration $\hat{\mathbb{B}}$. A schematic overview of this decomposition is given in Figure A.1.

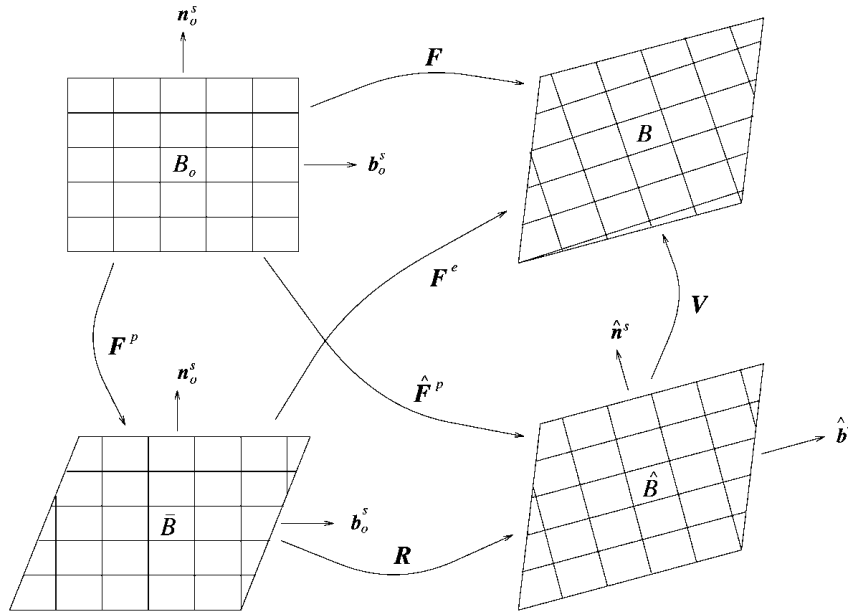


Figure A.1: Schematic representation of the multiplicative decomposition $\mathbf{F} = \mathbf{V}\mathbf{R}\mathbf{F}_p$. Figure adapted from [64]

The spatial velocity gradient \mathbf{L} now can be written as

$$\begin{aligned} \mathbf{L} &= \dot{\mathbf{F}}\mathbf{F}^{-1} = \left(\dot{\mathbf{V}}\mathbf{R}\mathbf{F}_p + \mathbf{V}\dot{\mathbf{R}}\mathbf{F}_p + \mathbf{V}\mathbf{R}\dot{\mathbf{F}}_p \right) \left(\mathbf{F}_p^{-1}\mathbf{R}^T\mathbf{V}^{-1} \right) \\ &= \dot{\mathbf{V}}\mathbf{V}^{-1} + \mathbf{V}\dot{\mathbf{R}}\mathbf{R}^T\mathbf{V}^{-1} + \mathbf{V}\mathbf{R}\dot{\mathbf{F}}_p\mathbf{F}_p^{-1}\mathbf{R}^T\mathbf{V}^{-1} \end{aligned} \quad (\text{A.2})$$

If \mathbf{F}_p leaves the lattice undistorted, the spatial velocity gradient expressed in the coordinates of $\hat{\mathbb{B}}$ is given by

$$\bar{\mathbf{L}} = \dot{\mathbf{F}}_p\mathbf{F}_p^{-1} \quad (\text{A.3})$$

and because $\hat{\mathbf{F}}_p = \mathbf{R}\mathbf{F}_p$, the definition of the velocity gradient in configuration $\hat{\mathbb{B}}$ reads

$$\hat{\mathbf{L}}_p = \left(\dot{\mathbf{R}}\mathbf{F}_p + \mathbf{R}\dot{\mathbf{F}}_p \right) \mathbf{F}_p^{-1} \mathbf{R}^T = \dot{\mathbf{R}}\mathbf{R}^T + \mathbf{R}\bar{\mathbf{L}}_p\mathbf{R}^T \quad (\text{A.4})$$

The left stretch tensor contains the elastic strains. Assuming small strains, this tensor can also be written as $\mathbf{V} = \mathbf{I} + \epsilon$ and thus $\dot{\mathbf{V}} = \dot{\epsilon}$ and $\mathbf{V}^{-1} = \mathbf{I} - \epsilon$, where \mathbf{I} is the second order identity tensor. Substitution of these relations in (A.2) yields

$$\begin{aligned} \mathbf{L} &= \dot{\epsilon}(\mathbf{I} - \epsilon) + (\mathbf{I} + \epsilon) \dot{\mathbf{R}}\mathbf{R}^T (\mathbf{I} - \epsilon) + (\mathbf{I} + \epsilon) \mathbf{R}\dot{\mathbf{F}}_p\mathbf{F}_p\mathbf{R}^T (\mathbf{I} - \epsilon) \\ &= \dot{\epsilon} - \dot{\epsilon}\epsilon + \dot{\mathbf{R}}\mathbf{R}^T + \mathbf{R}\dot{\mathbf{F}}_p\mathbf{F}_p\mathbf{R}^T + \epsilon \left(\dot{\mathbf{R}}\mathbf{R}^T + \mathbf{R}\dot{\mathbf{F}}_p\mathbf{F}_p\mathbf{R}^T \right) - \\ &\quad \left(\dot{\mathbf{R}}\mathbf{R}^T + \mathbf{R}\dot{\mathbf{F}}_p\mathbf{F}_p\mathbf{R}^T \right) \epsilon - \epsilon \left(\dot{\mathbf{R}}\mathbf{R}^T + \mathbf{R}\dot{\mathbf{F}}_p\mathbf{F}_p\mathbf{R}^T \right) \epsilon \\ &= \dot{\epsilon} - \dot{\epsilon}\epsilon + \hat{\mathbf{L}}_p + \epsilon\hat{\mathbf{L}}_p - \hat{\mathbf{L}}_p\epsilon - \epsilon\hat{\mathbf{L}}_p\epsilon \end{aligned} \quad (\text{A.5})$$

By definition, all second order tensors can be decomposed into a symmetric and a skew-symmetric parts and thus $\mathbf{L} = \mathbf{D} + \mathbf{W}$. Here, the rate of deformation tensor \mathbf{D} resembles the symmetric and the spin tensor \mathbf{W} resembles the skew-symmetric part of the velocity gradient. As the total deformation gradient \mathbf{L} can be decomposed as such, so do the representations $\bar{\mathbf{L}}$ and $\hat{\mathbf{L}}$. This makes it possible to write the resulting expression from (A.5) as

$$\begin{aligned} \mathbf{D} &= \dot{\epsilon} - \frac{1}{2} \left(\dot{\epsilon}\epsilon + (\dot{\epsilon}\epsilon)^T \right) + \hat{\mathbf{D}}_p + \epsilon\hat{\mathbf{W}}_p - \hat{\mathbf{W}}_p\epsilon - \epsilon\hat{\mathbf{D}}_p\epsilon \\ \mathbf{W} &= -\frac{1}{2} \left(\dot{\epsilon}\epsilon - (\dot{\epsilon}\epsilon)^T \right) + \hat{\mathbf{W}}_p + \epsilon\hat{\mathbf{D}}_p - \hat{\mathbf{D}}_p\epsilon - \epsilon\hat{\mathbf{W}}_p\epsilon \end{aligned} \quad (\text{A.6})$$

by considering its symmetric and skew-symmetric parts.

Further simplification of (A.6) is possible if the elastic strain is assumed to be so small that $\mathbf{V} \approx \mathbf{I}$ and thus all terms containing ϵ and $\dot{\epsilon}$ in (A.6) disappear. The final configuration is then represented by $\mathbb{B} \approx \hat{\mathbb{B}}$ and the final velocity gradient equals the definition in (A.4): $\mathbf{L} \approx \hat{\mathbf{L}}$. By using the formal definition of the symmetric and skew-symmetric part of this tensor, the additive decomposition is derived as:

$$\begin{aligned} \mathbf{D} &= \frac{1}{2} (\mathbf{L} + \mathbf{L}^T) = \frac{1}{2} (\dot{\mathbf{R}}\mathbf{R}^T + \mathbf{R}\dot{\mathbf{R}}^T) + \mathbf{R}\bar{\mathbf{D}}_p\mathbf{R}^T = \mathbf{R}\bar{\mathbf{D}}_p\mathbf{R}^T \\ \mathbf{W} &= \frac{1}{2} (\mathbf{L} - \mathbf{L}^T) = \frac{1}{2} (\dot{\mathbf{R}}\mathbf{R}^T - \mathbf{R}\dot{\mathbf{R}}^T) + \mathbf{R}\bar{\mathbf{W}}_p\mathbf{R}^T = \dot{\mathbf{R}}\mathbf{R}^T + \mathbf{R}\bar{\mathbf{W}}_p\mathbf{R}^T \end{aligned} \quad (\text{A.7})$$

by making use of $\dot{\mathbf{R}}\mathbf{R}^T = -\mathbf{R}\dot{\mathbf{R}}^T$. Recalling that the elastic velocity gradient can be written as $\mathbf{L}_e = \dot{\mathbf{R}}\mathbf{R}^T$ in the case of negligibly small elastic stretch, it has now been shown that the plastic velocity gradient can be rewritten as an additive decomposition of its plastic and elastic parts as

$$\mathbf{L} = \mathbf{D} + \mathbf{W} = \mathbf{W}_e + \mathbf{R}_e (\bar{\mathbf{D}}_p + \bar{\mathbf{W}}_p) \mathbf{R}_e^T \quad (\text{A.8})$$

which equals the final result obtained in [29]. The derivation therein has thus been validated by applying the small elastic stretch assumption to the decomposition proposed by Kok et. al.

B | Continuously differentiable approximation of the max() function

The $\max()$ function can be approximated with several continuously differentiable functions, each of which have different characteristics in terms of approximation accuracy, numerical stability and convergence behaviour in a stress-update algorithm. Three different functions were tested in the context of this work, being a *modified generalised mean* function, the soft *maximum* function and the *hyperbolic tangent smoothing* function. These functions and their derivatives are given in Table B.1.

A parameter q is introduced in each function. This parameter controls the rate with which the approximation function changes its slope in the transition region between the function value of ϕ and 0. The relation between q and the resemblance between $\bar{\phi}$ and $\max(0, \phi)$ is indicated in Table B.1. The shift parameter $\delta > 0$ in the generalised mean function also affects the size of the transition region.

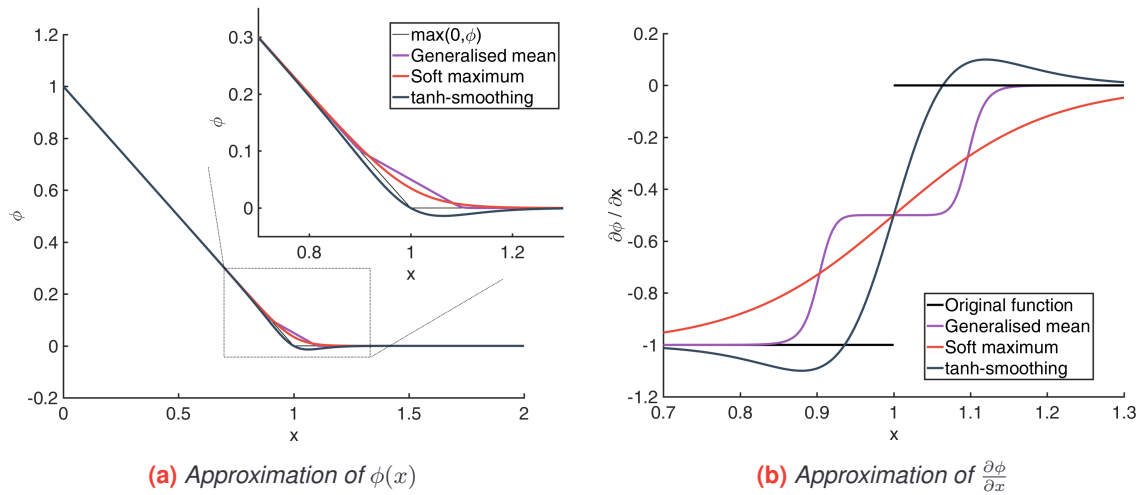


Figure B.1: Comparison of different approximations for the $\max()$ function with $\phi = 1 - x$

Figure B.1a shows the three approximations applied to the test function $\phi = 1 - x$. The approximated derivatives $\frac{\partial \bar{\phi}}{\partial x} = \frac{\partial \bar{\phi}}{\partial \phi} \frac{\partial \phi}{\partial x}$ are depicted in Figure B.1b. The control parameter q is set to 10 for both the generalised mean and soft maximum functions. For the tanh-smoothing function, $q = 10^{-1}$ and $\delta = 10^{-1}$. Both the generalised mean function and soft maximum function lie above the original lines and converge to 0 in the limit $x \rightarrow \infty$. The tanh-smoothing function lies below the original lines in the transition region, apart from the point where $\phi(x) = 0$, where also $\bar{\phi}(x) = 0$.

Table B.1: Overview of continuously differentiable approximation of the $\max()$ function

	$\bar{\phi} =$	$\frac{\partial \bar{\phi}}{\partial \phi} =$	$\bar{\phi} \rightarrow \max(0, \phi)$ if
generalised mean	$\frac{1}{2} \left((\phi^q + \delta^q)^{1/q} + \phi \right)$	$\frac{1}{2} \left(\phi^{q-1} (\phi^q + \delta^q)^{\frac{1}{q}-1} + 1 \right)$	$q \rightarrow \infty, \delta \rightarrow 0$
soft maximum	$\frac{1}{q} \log(1 + e^{q\phi})$	$e^{q\phi} / (1 + e^{q\phi})$	$q \rightarrow \infty$
tanh-smoothing	$\frac{\phi}{2} \left(1 + \tanh\left(\frac{\phi}{q}\right) \right)$	$\frac{1}{2} \left(1 + \tanh\left(\frac{\bar{r}_0^{(\alpha)}}{q}\right) + \frac{\phi}{q \cosh^2\left(\frac{\bar{r}_0^{(\alpha)}}{q}\right)} \right)$	$q \rightarrow 0$

For the chosen control parameters, the error in the transition area is largest for the generalised mean function. A significant reduction of this error is however possible by reducing δ and, less effective, by increasing q . The approximation error for the soft maximum function can partially be remedied by increasing the value for q , but this can cause overflow of the term $e^{q\phi}$ especially when ϕ takes larger values. The soft maximum function is thus less suitable for numerical implementation. The approximation of the tanh-smoothing function is already good for a relatively large value for q and can be effectively improved by further reducing this control parameter.

Convergence behaviour of approximation functions

In terms of accuracy, the generalised mean and tanh-smoothing function seem favourable choices to replace the $\max()$ function in the modified stress-update algorithm. To determine the version that will finally be implemented, the approximation functions are implemented in a single yield surface return mapping algorithm and their convergence behaviour is studied. A material model with Von-Mises plasticity and Nadai hardening is simulated. The original yield criterion for this material is defined in terms of the plastic parameter γ as

$$\phi = \bar{\sigma}^* - \frac{E}{1+\nu} \gamma - \sqrt{\frac{2}{3}} (\sigma_0 + C(\epsilon_{eq} + \epsilon_0)^n) \quad (\text{B.1})$$

and will be approximated by $\tilde{\phi}$ using the equations in Table B.1. The derivative of the flow criterion with respect to the plastic parameter is

$$\frac{\partial \phi}{\partial \gamma} = -\frac{E}{1+\nu} - nC \sqrt{\frac{2}{3}} \left(\sqrt{\frac{2}{3}} \gamma + \epsilon_0 \right)^{n-1} \quad (\text{B.2})$$

and will be approximated by $\frac{\partial \tilde{\phi}}{\partial \gamma} = \frac{\partial \tilde{\phi}}{\partial \phi} \frac{\partial \phi}{\partial \gamma}$ using the relations in Table B.1. In (B.1) and (B.2), $\bar{\sigma}^*$ is the trial Von-Mises equivalent stress and ϵ_{eq} is the equivalent plastic strain. σ_0 , C , ϵ_0 and n are hardening parameters. E is the material's Young's modulus and ν is the Poisson's ratio.

The return-mapping algorithm is applied to a test problem with the parameters shown in Table B.2. The strain is prescribed in one load increment. Figure B.2 shows the convergence rate of the different functions. It is seen that all approximation functions converge, but at different rates. Both the generalised mean as well as the hyperbolic tangent function initially show a quadratic convergence rate, whereas the convergence rate of the soft maximum function is linear and thus unfavourable.

The numerical outcomes of the different simulations are given in Table B.3. The deviation of the final result obtained using the soft maximum function compared to that of the original code is significant. This difference can be attributed to the asymptotic behaviour of the soft maximum and the inability to decrease the size of the transition region due to overflow of the $\exp()$ operator. The final results of the other approximations are identical to that of the original code up to the precision of the convergence tolerance.

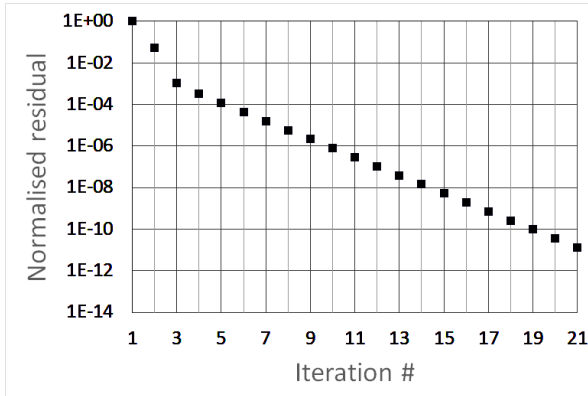
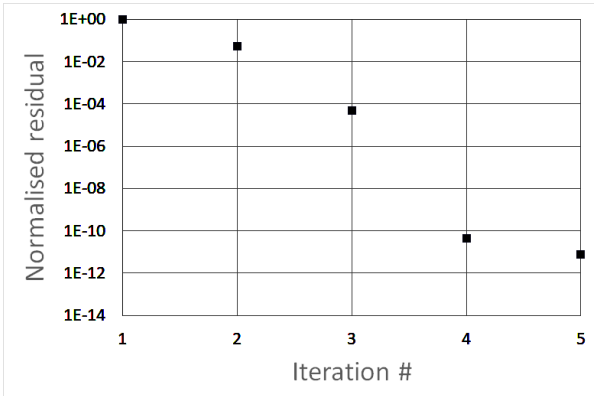
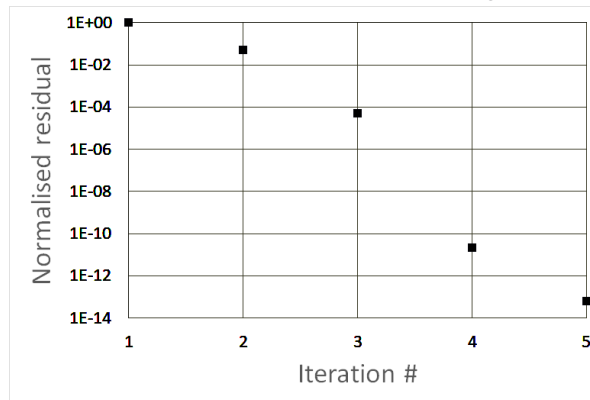
Due to its favourable convergence behaviour and ability to exactly capture the elastic-plastic transition point $\phi(\gamma) = 0$, the tanh-smoothing function will be implemented in the modified crystal plasticity stress update algorithm in Section 3.1.1.

Table B.2: Parameters for the coverage test

Parameter	Value	Parameter	Value
σ_0	315.7 MPa	C	957.9
ϵ_0	0.177	n	0.0017143
E	210000 MPa	ν	0.3
q (generalised mean)	10	δ	10^{-8}
q (tanh-smoothing)	10^{-5}	q (smooth maximum)	1
ϵ	$[0.005, -0.0025, -0.0025, 0, 0, 0]^T$		
Convergence criterion	$ \bar{\phi} < 10^{-8}$ (for original code, $ \phi < 10^{-8}$)		

Table B.3: Final solution values obtained with the different algorithms

Algorithm	Equivalent plastic strain	σ
Original (with elastic check)	0.00341768	$[255.605, -127.803, -127.803, 0, 0, 0]^T$
Soft maximum approximation	0.00317253	$[295.206, -147.603, -147.603, 0, 0, 0]^T$
Generalised mean approximation	0.00341768	$[255.605, -127.803, -127.803, 0, 0, 0]^T$
Tanh-smoothing approximation	0.00341768	$[255.605, -127.803, -127.803, 0, 0, 0]^T$

**(a)** Convergence rate for the soft maximum function**(b)** Convergence rate for the generalised mean function**(c)** Convergence rate for the tanh-smoothing function**Figure B.2:** Comparison of convergence rate of the different approximation functions

C | Stress-update algorithm flowcharts

Table C.1: Original algorithm formulation

Algorithmic stress update with active set search
<p>Initialisation:</p> <ol style="list-style-type: none"> 1. Define $\gamma_k = \gamma_n$ 2. Get trial stress $\sigma^* = \sigma_n + \mathbb{C}^e : d\epsilon_n$ <p>Elastic check</p> <ol style="list-style-type: none"> 3. Determine flow criteria $\phi^{(\alpha)} \forall \alpha \in [1, \dots, n]$ <ol style="list-style-type: none"> (a) Get Schmid tensor $\mathbf{P}_k^{(\alpha)} = \text{sym} \left(\mathbf{R}_{e,n} \mathbf{R}_{m,n} \mathbf{s}^{(\alpha)} \otimes \mathbf{n}^{(\alpha)} \mathbf{R}_{e,n}^T \mathbf{R}_{m,n}^T \right)$ (b) Calculate resolved shear stress $\tau_k^{(\alpha)} = \sigma^* : \mathbf{P}_k^{(\alpha)}$ (c) Determine flow criterion $\phi^{(\alpha)} = \tau_k^{(\alpha)} - \tau_{cr}^{(\alpha)} \left(\gamma_k^{(\alpha)}, \nabla \gamma_n^{(\alpha)} \right)$ 4. If $\phi^{(\alpha)} \leq 0 \forall \alpha \in [1, \dots, n]$, the step is elastic, set $\epsilon_{n+1}^p = \epsilon_{n+1}^p$, $\sigma_{n+1} = \sigma^*$, $\mathbb{C}_{n+1}^{ep} = \mathbb{C}^e$, $\mathcal{A}_{n+1} = \emptyset$ and exit. <p>Plastic slip update</p> <ol style="list-style-type: none"> 5. Set active set $\mathcal{A} = \mathcal{A}_n$ 6. Initialise $k = -1, \gamma_k = 0$ 7. While $\sum_{\alpha \in \mathcal{A}} \ \tau_{k+1}^{(\alpha)}\ > \text{tol}$ and $k < \text{max iter}$ do: <ol style="list-style-type: none"> (a) Update $k = k + 1$ (b) If $k > 0$, calculate $\Delta \gamma_{k+1}^{(\alpha)} = B^{(\alpha\beta)*-1} r^{(\beta)}$. <ol style="list-style-type: none"> i. Update $\gamma_{k+1}^{(\alpha)} = \gamma_k^{(\alpha)} + \Delta \gamma_{k+1}^{(\alpha)}$ ii. Apply scaling update $\gamma_{k+1}^{(\alpha)} = \gamma_k^{(\alpha)} + (1 - \theta) \Delta \gamma_{k+1}^{(\alpha)}$ with $\theta = \min_{\alpha \in \mathcal{A}} \left(1 - \frac{\gamma_k^{(\alpha)}}{\Delta \gamma_{k+1}^{(\alpha)}} \right)$ if any $\Delta \gamma_{k+1}^{(\alpha)} < 0$ and store most violated system (c) Update plastic strain $\epsilon_{p,k+1} = \sum_{\alpha \in \mathcal{A}} \gamma_{k+1}^{(\alpha)} \mathbf{P}^{(\alpha)}$ and stress state $\sigma_{k+1} = \sigma^* - \mathbb{C}_e : \epsilon_{p,k+1}$ (d) Calculate $r_{k+1}^{(\alpha)} \equiv \tilde{\phi}^{(\alpha)}(\sigma^*)$ as defined in 3. (e) Determine Jacobian $B^{(\alpha\beta)*} = \mathbf{P}^{(\alpha)} : \mathbb{C}_e : \mathbf{P}^{(\beta)} + \frac{\partial \tau_k^{(\alpha)}}{\partial \gamma_{k+1}^{(\beta)}}$ and perform perturbation $\hat{B}^{(\alpha\beta)*} = B^{(\alpha\beta)*} + \epsilon \mathbf{I}$ for singular $B^{(\alpha\beta)*}$ 8. If $\sum_{\alpha \in \mathcal{A}} r^{(\alpha)} \Delta \gamma^{(\alpha)} < 0$, remove most violated system as in 7(b) from \mathcal{A} and go to 6. 9. If $\phi^{(\alpha)} > 0$ for some $\alpha \in [1, \dots, n] \setminus \mathcal{A}$, add maximally loaded system to \mathcal{A} and go to 6. <p>Elastoplastic moduli update</p> <ol style="list-style-type: none"> 10. $\mathbb{C}_{n+1}^{ep} = \mathbb{C}^e - \sum_{\alpha=1}^n \sum_{\beta=1}^n B^{(\alpha\beta)*-1} \left(\mathbb{C}^e : \mathbf{P}^{(\alpha)} \right) \otimes \left(\mathbf{P}^{(\beta)} : \mathbb{C}^e \right)$

Table C.2: Modified algorithm formulation

Algorithmic stress update without active set search and elastic check
<p>Initialisation:</p> <ol style="list-style-type: none"> 1. Define $\gamma_k = \gamma_n$ 2. Get trial stress $\sigma^* = \sigma_n + \mathbb{C}^e : d\epsilon_n$ <p>Plastic slip update</p> <ol style="list-style-type: none"> 3. Initialise $k = -1, \gamma_k = 0$ 4. While $\sum_{\alpha=1}^n \ \tau_{k+1}^{(\alpha)}\ > \text{tol}$ and $k < \text{max iter}$ do: <ol style="list-style-type: none"> (a) Update $k = k + 1$ (b) If $k > 0$, calculate $\Delta \gamma_{k+1}^{(\alpha)} = B^{(\alpha\beta)*-1} r^{(\beta)}$ <ol style="list-style-type: none"> i. If $r^{(\alpha)} \Delta \gamma^{(\alpha)} < 0$ for a system α, set $r^{(\alpha)}$ and corresponding rows in $B^{(\alpha\beta)}$ to 0, perform perturbation $\hat{B}^{(\alpha\beta)*} = B^{(\alpha\beta)*} + \epsilon \mathbf{I}$ for singular $B^{(\alpha\beta)*}$ and go to 4(b) ii. Update $\gamma_{k+1}^{(\alpha)} = \gamma_k^{(\alpha)} + \Delta \gamma_{k+1}^{(\alpha)}$ (c) Update plastic strain $\epsilon_{p,k+1} = \sum_{\alpha \in \mathcal{A}} \gamma_{k+1}^{(\alpha)} \mathbf{P}^{(\alpha)}$ and stress state $\sigma_{k+1} = \sigma^* - \mathbb{C}_e : \epsilon_{p,k+1}$ (d) Calculate $r_{k+1}^{(\alpha)} \equiv \tilde{\phi}^{(\alpha)} = f \left(\phi_0^{(\alpha)}(\sigma^*) \right)$ <ol style="list-style-type: none"> i. Get Schmid tensor $\mathbf{P}_k^{(\alpha)} = \text{sym} \left(\mathbf{R}_{e,n} \mathbf{R}_{m,n} \mathbf{s}^{(\alpha)} \otimes \mathbf{n}^{(\alpha)} \mathbf{R}_{e,n}^T \mathbf{R}_{m,n}^T \right)$ ii. Calculate resolved shear stress $\tau_k^{(\alpha)} = \sigma^* : \mathbf{P}_k^{(\alpha)}$ iii. Determine flow criterion $\phi_0^{(\alpha)} = \tau_k^{(\alpha)} - \tau_{cr}^{(\alpha)} \left(\gamma_k^{(\alpha)}, \nabla \gamma_n^{(\alpha)} \right)$ iv. Calculate residual $r^{(\alpha)} = \frac{1}{2} \phi_0^{(\alpha)} \left(1 + \tanh \left(\frac{\phi_0^{(\alpha)}}{q} \right) \right)$ (e) Determine Jacobian: $A^{(\alpha)} = \frac{1}{2} \left(1 + \tanh \left(\frac{\phi_0^{(\alpha)}}{q} \right) + q^{-1} \cosh^{-2} \left(\frac{\phi_0^{(\alpha)}}{q} \right) \right)$ $B_0^{(\alpha\beta)*} = \mathbf{P}^{(\alpha)} : \mathbb{C}_e : \mathbf{P}^{(\beta)} + \frac{\partial \tau_k^{(\alpha)}}{\partial \gamma_{k+1}^{(\beta)}}$ $B^{(\alpha\beta)*} = A^{(\alpha)} B_0^{(\alpha\beta)*}$ and perform perturbation $\hat{B}^{(\alpha\beta)*} = B^{(\alpha\beta)*} + \epsilon \mathbf{I}$ for singular $B^{(\alpha\beta)*}$ <p>Elastoplastic moduli update</p> <ol style="list-style-type: none"> 5. $\mathbb{C}_{n+1}^{ep} = \mathbb{C}^e - \sum_{\alpha=1}^n \sum_{\beta=1}^n A^{(\alpha)} B^{(\alpha\beta)*-1} \left(\mathbb{C}^e : \mathbf{P}^{(\alpha)} \right) \otimes \left(\mathbf{P}^{(\beta)} : \mathbb{C}^e \right)$

D | Driver input files for future work

In the FEM-simulations performed with the modified stress-update algorithm, it was found that convergence problems arise with increasing lattice rotations. A series of additional simulations was performed, in which a square shell body was subjected to simple shear deformation. Using the original stress update algorithm with active set prediction, the final strain state in one integration point of the most-rotated elements was retrieved. These strains can be loaded into the material point driver to identify the difference in behaviour between the original and modified algorithmic formulations. A total of three input files for the material point driver is shown below. For each of the inputs, the modified algorithm fails to converge, whereas the original code finds a solution. These input files can thus be used in further improvement of the modified stress-update algorithm.

```
STATE_VAR 60
LOAD_TYPE 4
TOLERANCE 1e-6

BEGIN_MATERIAL
210000.0d0 0.3d0 24.0d0 0.0d0 0.0d0 0.0d0 2.86d-7 0.7d0 1.0d6 5.0d7 0.5d0
END_MATERIAL

BEGIN_LOAD
1 2 4
1000 -0.048784d0 0.0455731d0 0.0d0 0.00201369d0 0.0d0 0.0d0 1.0d0
END_LOAD
```

```
STATE_VAR 60
LOAD_TYPE 4
TOLERANCE 1e-6

BEGIN_MATERIAL
210000.0d0 0.3d0 24.0d0 0.0d0 0.3d0 0.2d0 2.86d-7 0.7d0 1.0d6 5.0d7 0.5d0
END_MATERIAL

BEGIN_LOAD
1000 -0.0281359d0 0.0237463d0 0.0d0 0.00734103d0 0.0d0 0.0d0 1.0d0
END_LOAD
```

```
STATE_VAR 60
LOAD_TYPE 4
TOLERANCE 1e-6

BEGIN_MATERIAL
210000.0d0 0.3d0 24.0d0 0.0d0 0.0d0 0.0d0 2.86d-7 0.7d0 1.0d6 5.0d7 0.5d0
END_MATERIAL

BEGIN_LOAD
1000 0.0188577d0 -0.0149592d0 0.0d0 0.00462693d0 0.0d0 0.0d0 1.0d0
END_LOAD
```

E | Generating RVEs with random disorientation distributions

Within the crystal plasticity method, often representative volume elements (*RVEs*) with a limited amount of grains are used. Each grain therein is assigned a specific crystallographic orientation. When *RVEs* are computer-generated, i.e. its crystallographic orientations are not obtained from a physical crystallographic texture, often random Euler angles are assigned to each grain. However, not every combination of random Euler angles represents a random crystallographic orientation. To address this problem, a method for generating random orientations from Euler angles is introduced in Section E.1. Furthermore, not every combination of random orientations will result in a random texture. This is especially the case for *RVEs* with a small number of grains. A method for determining the distribution of disorientations in an *RVE* is described in Section E.2. Combining the results from Sections E.1 and E.2, suitable models for simulating the macroscopic behaviour of polycrystalline materials will be generated in Section E.3.

E.1 Generating random crystallographic orientations

For specifying the grain orientation in the crystal plasticity model used in this work, Euler angles in Bunge format are used. The rotated basis $(\mathbf{x}', \mathbf{y}', \mathbf{z}')$ specifying the grain orientation is found by rotating the reference frame $(\mathbf{x}, \mathbf{y}, \mathbf{z})$ using the angles ϕ_1 , Φ and ϕ_2 as:

$$(\mathbf{x}, \mathbf{y}, \mathbf{z}) \xrightarrow[\phi_1]{\mathbf{z}\text{-axis}} (\mathbf{u}, \mathbf{v}, \mathbf{w}) \xrightarrow[\Phi]{\mathbf{u}\text{-axis}} (\mathbf{u}, \mathbf{w}, \mathbf{z}') \xrightarrow[\phi_1]{\mathbf{z}'\text{-axis}} (\mathbf{x}', \mathbf{y}', \mathbf{z}') \quad (\text{E.1})$$

As the rotations are applied successively, a random selection of Euler angles will not automatically result in a random final orientation. A method for generation random orientations is described by Becker [65]. First, a random rotation about the \mathbf{z} -axis is performed. Then, the \mathbf{z} -axis is rotated to a random point on a sphere. The rotation matrix \mathbf{R} specifying the rotated basis $(\mathbf{x}', \mathbf{y}', \mathbf{z}')$ in terms of the reference frame $(\mathbf{x}, \mathbf{y}, \mathbf{z})$ is found as follows. Three random numbers $n_i \in [0, 1]$, $i = 1, 2, 3$ are generated. From those numbers, the parameters

$$\begin{aligned} \theta &= n_1 - \pi \\ \phi &= \pi n_2 \\ z &= 2n_3 \end{aligned} \quad (\text{E.2})$$

are calculated. From these parameters, the material orientation matrix \mathbf{R}_m is defined as

$$\mathbf{R}_m = \begin{bmatrix} \cos \theta - z \sin(\phi - \theta) \sin \phi & \sin \theta - z \cos(\phi - \theta) \sin \phi & \sin \phi \sqrt{2z - z^2} \\ \sin \theta - z \sin(\phi - \theta) \cos \phi & \cos \theta - z \cos(\phi - \theta) \cos \phi & \cos \phi \sqrt{2z - z^2} \\ -\sin \phi \sqrt{2z - z^2} & -\cos \phi \sqrt{2z - z^2} & 1 - z \end{bmatrix} \quad (\text{E.3})$$

The calculation of the Euler angles from this rotation matrix follows the approach described in [66] and is shown in Table E.1. For creating the *RVEs*, a total of 1000 random crystal orientations are generated using Equations (E.2) and (E.3). Figure E.1 shows the set of Euler angles ϕ_1 , Φ and ϕ_2 and the orientations of the \mathbf{z}' -axis for this set. It is seen that the \mathbf{z}' -axes are well-distributed over the spherical domain, but that the Euler angles are not randomly distributed over the domain (ϕ_1, Φ, ϕ_2) . The generation method described above has thus provided a more randomly distributed set of crystal orientations than that resulting from generating orientations from three random Euler angles.

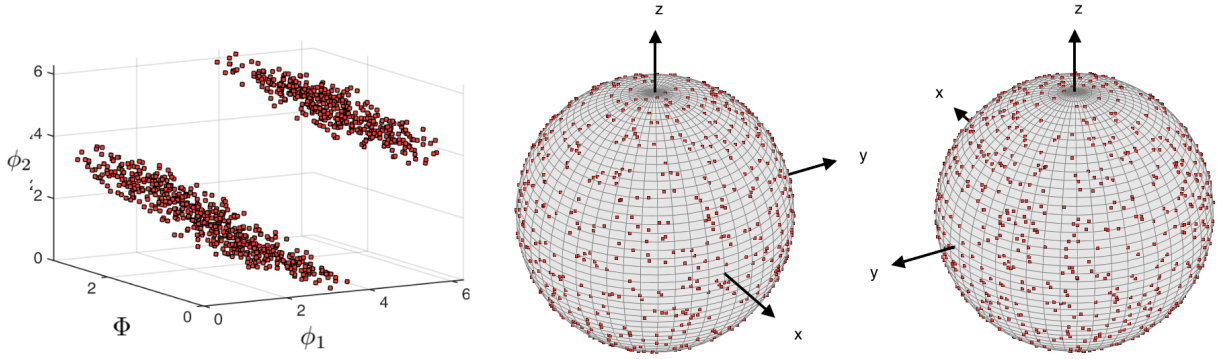


Figure E.1: Visualisation of generated random crystal orientations

Table E.1: Determining Euler angles from rotation matrix

Pseudo-code for computing Euler angles

```

 $\phi = \cos^{-1} R_{33}$ 
if  $\phi = 0$ :
     $\phi_1 = \tan^{-1} \left( -\frac{R_{21}}{R_{11}} \right)$ 
     $\phi_2 = 0$ 
else if  $\phi = \pi$ :
     $\phi_1 = \tan^{-1} \left( \frac{R_{21}}{R_{11}} \right)$ 
     $\phi_2 = 0$ 
otherwise:
     $\phi_1 = \tan^{-1} \left( -\frac{R_{31}}{R_{32}} \right)$ 
     $\phi_2 = \tan^{-1} \left( \frac{R_{13}}{R_{23}} \right)$ 
if  $\phi_i < 0, i = 1, 2$ :
     $\phi_i = \phi_i + \pi$ 

```

E.2 Calculating disorientation distributions

Given two adjacent grains with orientation matrices \mathbf{G}_1 and \mathbf{G}_2 , the misorientation between grains 1 and 2 can be calculated from $\mathbf{R} = \mathbf{G}_1 \mathbf{G}_2^{-1}$. The disorientation between the two grains is defined as the smallest of all symmetrically equivalent misorientations. According to MacKenzie, the disorientation angle ψ_d can be expressed as [39]:

$$1 + 2 \cos \psi_d = \max_{i,j} \text{Tr}(\mathbf{S}_i \mathbf{R} \mathbf{S}_j) \Rightarrow \psi_d = \cos^{-1} \left(\frac{1}{2} \left[\max_{i,j} \text{Tr}(\mathbf{S}_i \mathbf{R} \mathbf{S}_j) - 1 \right] \right) \quad (\text{E.4})$$

in which \mathbf{S}_i is one of the 24 rotation matrices representing proper symmetry rotations as shown in Table E.2. The disorientation distribution can be obtained by calculating ψ_d for every possible pair of adjacent grains and computing the empirical cumulative density function (CDF) from this disorientation data. The empirical CDF $\hat{F}_n(t)$ can be found using

$$\hat{F}_n(t) = \frac{\text{number of elements in sample} \leq t}{n} \quad (\text{E.5})$$

Table E.2: Proper symmetry rotation matrices S_i

$$\begin{aligned}
S_1 &= \begin{bmatrix} 1 & 0 & 0 \\ 0 & 1 & 0 \\ 0 & 0 & 1 \end{bmatrix}, S_2 = \begin{bmatrix} -1 & 0 & 0 \\ 0 & -1 & 0 \\ 0 & 0 & 1 \end{bmatrix}, S_3 = \begin{bmatrix} 1 & 0 & 0 \\ 0 & -1 & 0 \\ 0 & 0 & -1 \end{bmatrix}, S_4 = \begin{bmatrix} -1 & 0 & 0 \\ 0 & 1 & 0 \\ 0 & 0 & -1 \end{bmatrix}, \\
S_5 &= \begin{bmatrix} 0 & -1 & 0 \\ 1 & 0 & 0 \\ 0 & 0 & 1 \end{bmatrix}, S_6 = \begin{bmatrix} 0 & 1 & 0 \\ -1 & 0 & 0 \\ 0 & 0 & 1 \end{bmatrix}, S_7 = \begin{bmatrix} 1 & 0 & 0 \\ 0 & 0 & -1 \\ 0 & 1 & 0 \end{bmatrix}, S_8 = \begin{bmatrix} 1 & 0 & 0 \\ 0 & 0 & 1 \\ 0 & -1 & 0 \end{bmatrix}, \\
S_9 &= \begin{bmatrix} 0 & 0 & 1 \\ 0 & 1 & 0 \\ -1 & 0 & 0 \end{bmatrix}, S_{10} = \begin{bmatrix} 0 & 0 & -1 \\ 0 & 1 & 0 \\ 1 & 0 & 0 \end{bmatrix}, S_{11} = \begin{bmatrix} 0 & 1 & 0 \\ 1 & 0 & 0 \\ 0 & 0 & -1 \end{bmatrix}, S_{12} = \begin{bmatrix} 0 & 0 & 1 \\ 0 & -1 & 0 \\ 1 & 0 & 0 \end{bmatrix}, \\
S_{13} &= \begin{bmatrix} -1 & 0 & 0 \\ 0 & 0 & 1 \\ 0 & 1 & 0 \end{bmatrix}, S_{14} = \begin{bmatrix} 0 & 1 & 0 \\ 1 & 0 & 0 \\ 0 & 0 & 1 \end{bmatrix}, S_{15} = \begin{bmatrix} 0 & 0 & -1 \\ 0 & -1 & 0 \\ -1 & 0 & 0 \end{bmatrix}, S_{16} = \begin{bmatrix} 1 & 0 & 0 \\ 0 & 0 & 1 \\ 0 & 1 & 0 \end{bmatrix}, \\
S_{17} &= \begin{bmatrix} 0 & 0 & 1 \\ 1 & 0 & 0 \\ 0 & 1 & 0 \end{bmatrix}, S_{18} = \begin{bmatrix} 0 & 1 & 0 \\ 0 & 0 & 1 \\ 1 & 0 & 0 \end{bmatrix}, S_{19} = \begin{bmatrix} 0 & 1 & 0 \\ 0 & 0 & -1 \\ -1 & 0 & 0 \end{bmatrix}, S_{20} = \begin{bmatrix} 0 & -1 & 0 \\ 0 & 0 & -1 \\ 1 & 0 & 0 \end{bmatrix}, \\
S_{21} &= \begin{bmatrix} 0 & -1 & 0 \\ 0 & 0 & 1 \\ -1 & 0 & 0 \end{bmatrix}, S_{22} = \begin{bmatrix} 0 & 0 & -1 \\ 1 & 0 & 0 \\ 0 & -1 & 0 \end{bmatrix}, S_{23} = \begin{bmatrix} 0 & 0 & -1 \\ -1 & 0 & 0 \\ 0 & 1 & 0 \end{bmatrix}, S_{24} = \begin{bmatrix} 0 & 0 & 1 \\ -1 & 0 & 0 \\ 0 & -1 & 0 \end{bmatrix}
\end{aligned}$$

E.3 RVEs with random disorientation distributions

To obtain models with a sufficiently random disorientation distribution to be used in simulating the Hall-Petch behaviour, trial RVEs consisting out of 8, 16, 32 and 64 grains were generated. For the first three grain numbers, a total of 5000 RVEs is generated. For 64 grains, a total of 1000 RVEs is sampled. Each grain within an RVE is randomly assigned an orientation from the set of 1000 Euler angles generated in Section E.1. For each RVE, the empirical disorientation CDF is calculated. A histogram with equally wide bins, centred around the disorientation angles $\psi_d = 0^\circ, 5^\circ, \dots, 70^\circ$, is then calculated from this CDF. This allows for comparison with the MacKenzie-distribution for disorientations in random polycrystals [39]. The deviation with the random disorientation distribution is calculated from

$$\delta = \sum_{i=1}^{15} |p(\psi_i) - \hat{p}(\psi_i)| \quad (\text{E.6})$$

where $p(\psi_i)$ is the MacKenzie-distribution evaluated at disorientation angle ψ_i , $\hat{p}(\psi_i)$ is the height of the histogram bin centred around ψ_i obtained from the empirical CDF of the RVE and $\psi_i \in [0^\circ, 5^\circ, \dots, 70^\circ]$.

Figure E.2 shows the deviation with the MacKenzie-distribution for the generated trial-RVEs. It can be seen that for a larger grain number, the spread in the deviations becomes less. This indicates that for the 32 and 64-grain models, less effort has to be taken to obtain a more or less random texture. For an 8-grain model, only a very limited combination of angles will result in a random texture. However, for all four grain numbers, a satisfactory uniform disorientation distribution can be found as shown in Figure E.3. The grain orientation assignments for the best-possible disorientation distributions are provided in Table E.3. The locations of the different grains in the RVEs are indicated in Figure E.4.

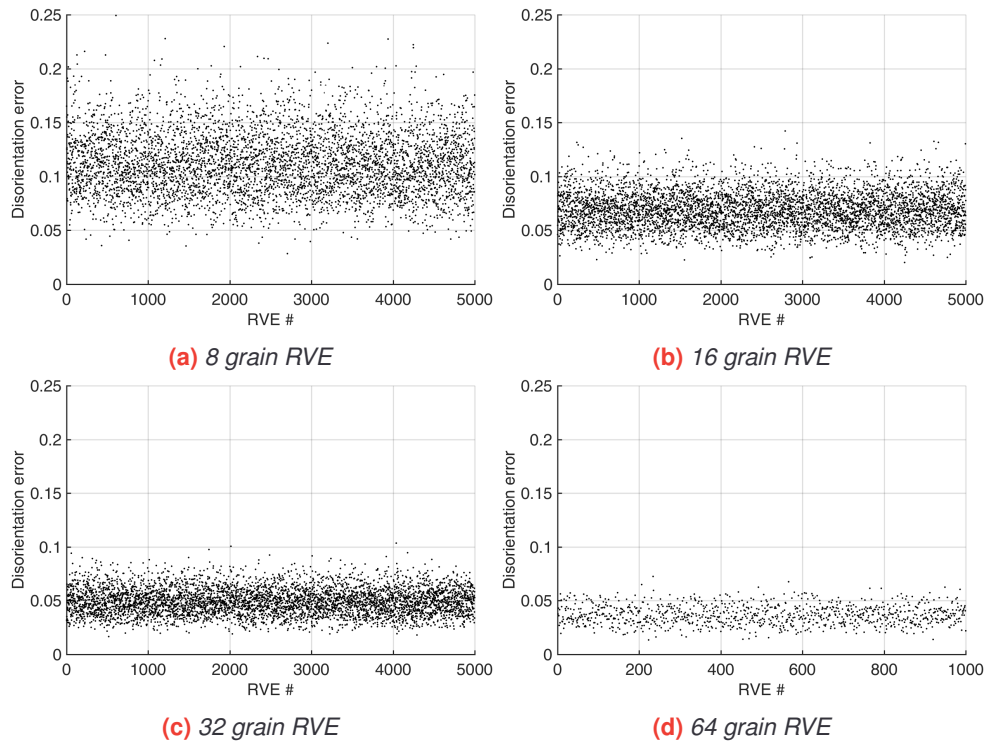


Figure E.2: Sum of the differences between histogram bin heights at $\psi_d = 0^\circ, 5^\circ, \dots, 70^\circ$ and the MacKenzie-distribution

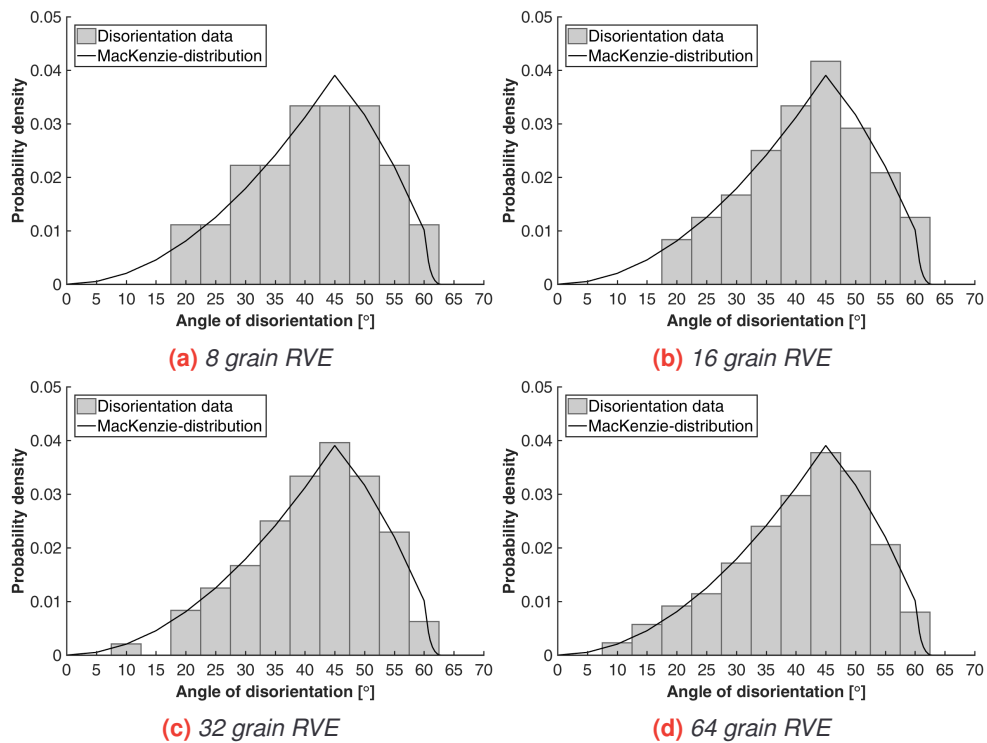


Figure E.3: Best-obtained disorientation distributions for various numbers of hexagonal grains

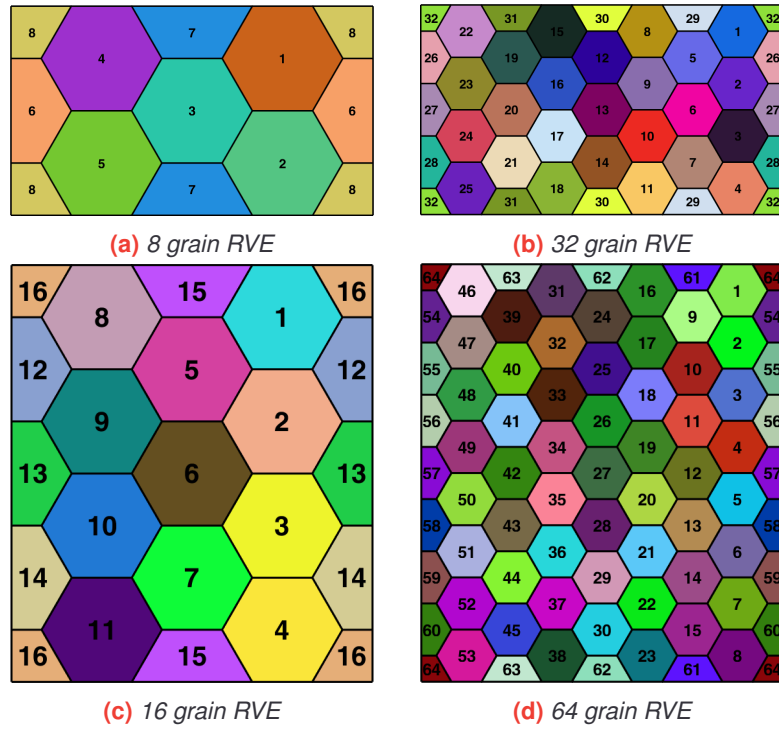


Figure E.4: Grain assignments for various RVE sizes. Corresponding colours indicate grains with the same material assignment and orientation.

Table E.3: Grain orientations used in the 8, 16, 32 and 64-grain RVEs

8 grains				32 grains				64 grains				64 grains - continued			
Grain #	ϕ_1	Φ	ϕ_2	Grain #	ϕ_1	Φ	ϕ_2	Grain #	ϕ_1	Φ	ϕ_2	Grain #	ϕ_1	Φ	ϕ_2
1	3.549	2.807	5.918	1	1.968	2.816	2.538	1	5.845	1.301	2.880	33	3.576	1.599	2.545
2	2.983	0.751	3.394	2	0.542	1.569	4.934	2	5.492	2.581	3.484	34	3.278	0.799	2.150
3	5.304	1.198	5.501	3	4.441	1.118	4.448	3	4.648	0.394	3.229	35	3.385	2.143	6.087
4	3.883	2.145	0.061	4	3.999	1.727	4.279	4	6.011	2.311	3.017	36	4.709	1.843	2.765
5	4.944	1.539	1.655	5	4.500	2.812	2.892	5	4.006	1.579	5.765	37	4.622	1.783	3.240
6	4.970	0.443	1.495	6	1.487	1.150	1.726	6	3.637	0.427	5.118	38	4.107	1.143	3.165
7	3.999	1.727	4.279	7	2.588	2.717	2.553	7	1.069	2.424	0.296	39	1.634	0.493	1.708
8	2.859	2.631	1.739	8	1.608	1.460	5.068	8	4.666	1.550	4.767	40	2.316	2.327	2.718
				9	3.568	1.643	2.650	9	5.566	2.989	5.088	41	3.428	2.589	0.934
				10	2.613	2.456	0.534	10	1.428	1.886	0.082	42	2.481	2.092	2.799
				11	0.824	1.511	3.271	11	1.893	2.490	4.262	43	5.588	1.721	3.220
				12	2.727	1.125	1.916	12	3.754	2.556	1.982	44	3.931	1.527	5.458
				13	4.197	2.438	3.724	13	6.060	2.284	3.768	45	4.788	0.290	0.927
				14	5.786	1.039	0.449	14	2.254	2.282	1.077	46	5.054	1.254	4.047
				15	5.142	1.651	2.385	15	5.163	2.138	1.381	47	2.027	1.295	1.783
				16	6.011	2.311	3.017	16	2.193	0.391	0.960	48	6.123	2.224	1.141
				17	6.280	1.575	5.633	17	1.282	2.615	3.997	49	1.391	0.765	4.549
				18	0.647	1.538	2.627	18	6.011	2.311	3.017	50	1.968	2.816	2.538
				19	1.566	1.017	5.075	19	3.924	1.176	0.664	51	2.727	1.828	0.709
				20	5.971	1.931	0.445	20	3.174	2.615	3.471	52	3.056	1.960	5.606
				21	4.554	1.413	1.644	21	2.886	0.677	5.710	53	0.266	1.868	1.584
				22	6.268	1.678	3.751	22	4.288	1.232	1.118	54	4.775	0.623	5.751
				23	2.037	2.168	2.501	23	1.000	0.262	2.281	55	1.858	2.821	3.272
				24	3.357	0.993	1.926	24	0.139	1.556	3.219	56	3.023	1.109	0.155
				25	0.846	2.036	2.056	25	1.334	2.603	4.994	57	0.101	1.679	2.966
				26	4.734	1.740	0.275	26	4.606	2.261	5.136	58	6.123	2.224	1.141
				27	1.528	1.320	1.249	27	2.033	2.893	0.399	59	0.784	0.729	0.912
				28	1.246	1.309	4.747	28	0.562	2.422	2.870	60	3.884	0.574	3.824
				29	2.193	0.391	0.960	29	1.494	2.427	2.000	61	2.319	1.185	1.528
				30	0.929	2.507	2.142	30	3.421	2.092	6.110	62	3.216	0.793	0.672
				31	5.105	2.513	3.492	31	1.193	2.013	2.460	63	2.201	2.254	0.371
				32	0.849	2.158	0.094	32	5.229	2.618	3.462	64	0.540	1.597	6.278

F | Numerical integration of dislocation densities

To obtain the total number of statistically stored and geometrically necessary dislocation in an element, the dislocation densities must be integrated over the element surface:

$$n_{SSD} = \iint_A \rho_{SSD}(x, y) dA, \quad n_{GND} = \iint_A \rho_{GND}(x, y) dA \quad (F.1)$$

The stress update and gradient calculation user subroutines in Abaqus calculate the values for the dislocation densities at the integration points. The dislocation numbers can thus be found from these values using numerical integration. For triangular elements, the numerical approximation becomes:

$$n_{(\cdot)} = \iint_A \rho_{(\cdot)}(x, y) dA = \int_0^1 \int_0^{1-L_1} \rho_{(\cdot)}(L_1, L_2) \det(\mathbf{J}) dL_1 dL_2 \approx \sum_{i=1}^{n_{GP}} \rho_{(\cdot)}(L_{1i}, L_{2i}) w_i \det(\mathbf{J}_i) \quad (F.2)$$

in which i indicates the number of the integration point, w_i are the weight factors for the element's Gauss integration scheme and \mathbf{J} is the Jacobian matrix that transforms the integral into natural coordinates. Its determinant $\det(\mathbf{J}_i)$ is evaluated at the natural coordinates of the corresponding Gauss point. For a fully integrated, quadratic triangular element as in Figure F.1, the interpolation functions, Gauss points locations and corresponding weight factors are given in Table F.1.

The Jacobian matrix, defined as $\mathbf{J} = \begin{bmatrix} \frac{\partial x}{\partial L_1} & \frac{\partial y}{\partial L_1} \\ \frac{\partial x}{\partial L_2} & \frac{\partial y}{\partial L_2} \end{bmatrix}$ can be calculated from the vector of nodal coordinates

\mathbf{X} and the vector with interpolation functions $\mathbf{N} = [N_1, N_2, \dots, N_6]$ according to $\mathbf{J} = \begin{bmatrix} \frac{\partial \mathbf{N}}{\partial L_1} \\ \frac{\partial \mathbf{N}}{\partial L_2} \end{bmatrix} \mathbf{X}$.

In principle, this Jacobian can thus be found at each integration point by substituting of its coordinates in the derivatives of the interpolation functions and multiplying by the elements nodal coordinates. However, as $dA = dx dy = \det(\mathbf{J}) dL_1 dL_2$ and the area of the element in natural coordinates is $\frac{1}{2}$, it is found that $\det(\mathbf{J}) = 2A$ (with A the element area in real coordinates) for triangular elements with straight sides.

A Python post-processing macro has been written for Abaqus which loops over all elements and Gauss points and approximates the dislocation numbers using (F.2). The dislocation densities are directly obtained from the state variables at each integration point. The element area is read from the element volume output *EVOL*, which equals the element area for unit thickness shell elements. To be able to compare results for different-sized RVEs, the total dislocation numbers can be normalised using the total RVE area.

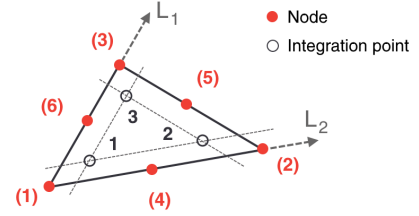


Figure F.1: Schematic overview of a quadratic triangular element

Table F.1: Interpolation functions and integration scheme details for quadratic triangular element

Interpolation functions:	Gauss point locations:	Weight factor:
$N_1 = (1 - L_1 - L_2)(1 - 2L_1 - 2L_2)$	GP 1: $(L_1, L_2) = \left(\frac{1}{6}, \frac{1}{6}\right)$	GP 1: $w_1 = \frac{1}{6}$
$N_2 = (2L_1 - 1)L_1$	GP 2: $(L_1, L_2) = \left(\frac{4}{6}, \frac{1}{6}\right)$	GP 2: $w_2 = \frac{1}{6}$
$N_3 = (2L_2 - 1)L_2$	GP 3: $(L_1, L_2) = \left(\frac{4}{6}, \frac{4}{6}\right)$	GP 3: $w_3 = \frac{1}{6}$
$N_4 = 4(1 - L_1 - L_2)L_1$		
$N_5 = 4L_1L_2$		
$N_6 = 4(1 - L_1 - L_2)L_2$		